

DISSERTATION

CUMULUS MOISTENING, THE DIURNAL CYCLE, AND  
LARGE-SCALE TROPICAL DYNAMICS

Submitted by

James H. Ruppert, Jr.

Department of Atmospheric Science

In partial fulfillment of the requirements

For the Degree of Doctor of Philosophy

Colorado State University

Fort Collins, Colorado

Summer 2015

Doctoral Committee:

Advisor: Richard H. Johnson

Eric D. Maloney

Sue van den Heever

V. Chandrasekar

Copyright by James H. Ruppert, Jr. 2015

All Rights Reserved

## ABSTRACT

### CUMULUS MOISTENING, THE DIURNAL CYCLE, AND LARGE-SCALE TROPICAL DYNAMICS

Observations and modeling techniques are employed to diagnose the importance of the diurnal cycle in large-scale tropical climate. In the first part of the study, soundings, radar, and surface flux measurements collected in the Indian Ocean DYNAMO experiment (Dynamics of the Madden–Julian Oscillation, or MJO) are employed to study MJO convective onset. According to these observations, MJO onset takes place as follows: moistening of the low–midtroposphere is accomplished by cumuliform clouds that deepen as the drying by large-scale subsidence and horizontal advection simultaneously wane. This relaxing of subsidence is tied to decreasing column radiative cooling, which links back to the evolving cloud population. A new finding from these observations is the high degree to which the diurnal cycle linked to air-sea and radiative fluxes invigorates clouds and drives column moistening each day. This diurnally modulated cloud field exhibits pronounced mesoscale organization in the form of open cells and horizontal convective rolls. Based on these findings, it is hypothesized that the diurnal cycle and mesoscale cloud organization represent two manners in which local convective processes promote more vigorous day-to-day tropospheric moistening than would otherwise occur.

A suite of model tests are carried out in the second part of the study to 1) test the hypothesis that the diurnal cycle drives moistening on longer timescales, and 2) better understand the relative roles of diurnally varying sea surface temperature (SST) and direct atmospheric radiative heating in the diurnal cycle of convection. Moist convection is explicitly represented in

the model, the diurnal cycle of SST is prescribed, and cloud-interactive radiation is simulated with a diurnal cycle in shortwave heating. The large-scale dynamics are parameterized using the spectral weak temperature gradient (WTG) technique recently introduced by Herman and Raymond. In this scheme, external (i.e., large-scale) vertical motion  $w_{wtg}$  is diagnosed based on the internal diabatic heating in the model.  $w_{wtg}$  is then used to advect model temperature and humidity.  $w_{wtg}$  opposes domain-averaged temperature anomalies via adiabatic warming and cooling, thereby yielding a feedback between the model diabatic heating and the large-scale column moisture source associated with large-scale vertical motion. With a control simulation that successfully replicates a regime of shallow convection similar to nature, it is found through sensitivity tests that the diurnal cycle in tropospheric radiative heating is the dominant driver of both diurnal column moisture variations and nocturnal rainfall in this regime, the latter of which agrees with previous findings by Randall et al. The diurnal cycle in SST and surface fluxes, in turn, drives the daytime convective regime, which is distinct from the nocturnal regime by its rooting in the boundary layer.

A simulation in which the diurnal cycle is stretched to 48 h amplifies an important nonlinear feedback at work in the diurnal cycle, which owes to the high-amplitude diurnal cycle in column relative humidity RH. This diurnal cycle in RH limits the amount of evaporation, and hence evaporative cooling, that takes place in the cloud layer. By throttling down the diabatic cooling, the diurnal cycle throttles down the daily-mean moisture sink driven by large-scale subsidence, such that the environment drifts toward a more moist state, all else being equal. When the diurnal cycle is not present, this nonlinear moisture source is weaker, and the environment drier. This feedback rectifies diurnal moistening onto longer timescales, thereby linking the diurnal cycle to longer timescales. These findings suggest that 1) the diurnal cycle of

moist convection, as observed in DYNAMO, cannot be ruled out as an column moisture source important to MJO initiation, and 2) that proper representation of the diurnal cycle is prerequisite to accurate representation of large-scale climate, at least within the regime studied herein.

## ACKNOWLEDGEMENTS

I am greatly indebted to Dick Johnson, whose enthusiasm for my work has exerted a continual driving force that has motivated me through even the most downtrodden of days. Without his enthusiasm, I would never have experienced just how exciting and fascinating this science is. Furthermore, I owe immeasurable gratitude for the wealth of ideas that Dick has shared with me, including the original seedling of a thought that I should look into the diurnal cycle in DYNAMO data. I must give great thanks to my committee members – Eric Maloney, Sue van den Heever, and V. Chandrasekar – whose comments on this work I greatly respect and appreciate, and whose guidance at the various stages of this research has been critical. I must especially acknowledge Sue, who provided the keen idea to change the period of the diurnal cycle in our model simulations. Without this ingenious trick, the diurnal cycle–climate feedback might not have been detected.

I am also indebted to Dave Randall and Dave Raymond, who both provided important suggestions in the use of large-scale balanced dynamics for application in the modeling study. Without the instruction from Eric Maloney through my time spent in tropical dynamics class, however, I wouldn't have understood a word from Dave Randall or Dave Raymond. To Eric I owe most of what I claim to know about tropical dynamics, the rest of which I owe to past and present students in his research group – specifically, Walter Hannah and Brandon Wolding.

To George Bryan I acknowledge his tireless work on his cloud model CM1, which he freely provides to the community. In addition, his help during a meeting in Boulder during the late stages of this research provided a lifeboat while I was drowning in model debugging.

I acknowledge Paul Ciesielski for his hard work on many of the DYNAMO observation datasets, as well as many very insightful discussions on this research. I also acknowledge Rick Taft for critical support with computers on many occasions. I owe thanks to many others for providing helpful comments at some stage in this research, including Dave Duncan, Alex Gonzalez, Dave Henderson, Bonne Hotmann, John Peters, Chris Slocum, Doug Stolz, and Elizabeth Thompson. I would also like to acknowledge the Department of Atmospheric Science administrative staff, without which the science would not be possible.

I must acknowledge my family – Mom, Dad, Collin, Meagan, and Caitlin, for their love and support, despite the unfortunate distances between us. I also acknowledge all of my close friends in Fort Collins, who make the tough pursuit worth it, if even with the thought of the weekend’s celebrations. Lastly, yet most importantly, I acknowledge my life-saving, care-taking, and ever-loving girlfriend, Tia. I always look forward to sharing each meal with you. The thoughts of our summer travel prospects, and those beyond, keep me going.

Support for this work has been provided by the National Science Foundation.

## TABLE OF CONTENTS

Abstract.....	ii
Acknowledgements.....	iii
Chapter 1: Introduction.....	1
Chapter 2: Diurnally modulated cumulus moistening in the preonset stage of the Madden–Julian oscillation during DYNAMO .....	6
2.1 Introduction.....	6
2.2 Data and methodology .....	6
A) Gridded sounding analysis.....	6
B) Radar cloud measurements .....	9
C) Auxiliary datasets.....	10
2.3 Overview of the DYNAMO MJO events .....	11
2.4 The diurnal cycle of cumulus moistening.....	22
2.5 Summary and conclusions .....	38
Chapter 3: On the driving mechanisms of the diurnal cycle of moist convection and feedbacks onto climate.....	44
3.1 Introduction.....	44
3.2 Weak temperature gradient forcing .....	45
3.3 Modeling techniques and methodology .....	48
A) Cloud-resolving model .....	48
B) Model base state and external forcing .....	52
C) Model experiments.....	55
D) The apparent heat source and moisture sink.....	58

3.3 Results.....	59
A) Overview of control simulation.....	59
B) Modified physics tests.....	74
C) The diurnal cycle and column moistening.....	86
D) Sensitivity tests.....	94
3.4 Summary and conclusions .....	97
Chapter 4: Overarching conclusions.....	101
References.....	105

# CHAPTER 1

## INTRODUCTION

The dynamics governing the coupling between moist-convective processes and large-scale circulation in the tropics is a topic of avid investigation presently, since such coupling has important impacts on weather globally, while major hurdles in improving its predictability (Waliser et al. 2012). A prime example of such coupling is the Madden–Julian Oscillation (MJO; Madden and Julian 1971, 1972). The MJO dominates tropical intraseasonal (20–90-day) variability and influences global weather—e.g., tropical cyclone frequency, monsoon onset and variability, ENSO, and midlatitude storm tracks—through myriad tropical–extratropical teleconnections (Zhang 2005, 2013). Through these teleconnections the MJO acts as a “bridge” between weather and climate (Zhang 2013), thereby holding a critical key to our advancement beyond medium-range predictability (Hendon et al. 2000; Waliser et al. 2003, 2012; Lin et al. 2006; Moncrieff et al. 2012). While studies have elucidated the principal diabatic heating structure and convective cloud evolution in the MJO, the physics governing the transition from predominant shallow cumuli to widespread, organized deep convection during MJO convective initiation remains largely unsolved (Bladé and Hartmann 1993; Maloney and Hartmann 1998; Johnson et al. 1999; Stephens et al. 2004; Majda and Stechmann 2009; Jiang et al. 2011; Hohenegger and Stevens 2013; Zhang et al. 2013).

Investigating MJO convective initiation was a central objective of the DYNAMO (Dynamics of the MJO) field campaign, which was conducted in the tropical Indian Ocean during 2011–12 boreal fall–winter in collaboration with CINDY (Cooperative Indian Ocean Experiment on Intraseasonal Variability in the Year 2011), AMIE (ARM MJO Investigation

Experiment), and LASP (Littoral Air-Sea Processes) (Yoneyama et al. 2013; Zhang et al. 2013). Hereafter, these efforts will be referred to collectively as DYNAMO. Two MJO events were comprehensively sampled in DYNAMO, providing an unprecedented opportunity to diagnose the key processes during the transition from shallow to deep convection in the MJO.

The MJO is a zonal overturning circulation that propagates eastward across the tropics at  $\sim 5 \text{ m s}^{-1}$  in connection with an upper-level divergent wind pattern, which typically spans the global tropics (Madden and Julian 1972). The *active phase* is characterized by upper-level divergence and enhanced deep convection, and the *suppressed phase* by upper-level convergence and mostly non-precipitating shallow cumuli (Zhang 2005 and references therein). While the associated upper-level divergent wind signal can circumnavigate the globe several times (Matthews 2008; Gottschalck et al. 2013), convective coupling typically initiates (referred to as MJO initiation henceforth) in the Indian Ocean and ceases in the central Pacific Ocean (Madden and Julian 1972; Hendon and Salby 1994; Wheeler and Hendon 2004).

During the transition from suppressed to active conditions in the MJO (from an Eulerian viewpoint), the prevailing character of convective clouds evolves from shallow cumulus, to congestus, to deep cumulonimbus as the free troposphere transitions from dry, to moist up to midlevels, to fully moistened, respectively (DeMott and Rutledge 1998; Johnson et al. 1999; Kikuchi and Takayabu 2004; Benedict and Randall 2007; Haertel et al. 2008; Yoneyama et al. 2008; Riley et al. 2011; Del Genio et al. 2012). This well-documented coupling between moist convection and column humidity within the MJO fundamentally owes to the effects of entrainment on ascending moist-convective clouds. The entrainment of low relative-humidity air reduces the buoyancy of these clouds—thereby limiting their terminal height—while entrainment in moister conditions has less of a negative impact on their buoyancy (Austin 1948; Wei et al.

1998; Redelsperger et al. 2002; Derbyshire et al. 2004; Takemi et al. 2004; Waite and Khouider 2010).

The systematic deepening of convective clouds prior to the active phase has led many to argue that the free-tropospheric moistening by the antecedent populations of cumulus and congestus clouds is important for *preconditioning* the environment for subsequent deep convection (Johnson et al. 1999; Kemball-Cook and Weare 2001; Kikuchi and Takayabu 2004; Benedict and Randall 2007; Yoneyama et al. 2008; Waite and Khouider 2010). The concept of cumulus preconditioning, in the context of the MJO, originates from “discharge–recharge” theory (Hendon and Liebmann 1990; Rui and Wang 1990; Bladé and Hartmann 1993). While the implicit meaning of cumulus preconditioning has evolved over time, a flaw in the original concept is that cumulus cloud populations do not typically moisten (i.e., humidify) the troposphere over a large scale *independent* of changes in large-scale circulation (Hohenegger and Stevens 2013).

Rather, large-scale circulation and humidity are intimately linked, that is, on the spatiotemporal scales important to the MJO, wherein temperature variations are relatively small (Charney 1963; Raymond 2001; Sobel et al. 2001). By this thinking, it is the feedbacks between convective clouds and large-scale circulation that are important, rather than the activity of the convective cloud population alone. For instance, while large-scale subsidence and horizontal moisture advection exert control over column humidity, and therefore over moist convection, clouds can reduce column radiative cooling. This reduction can in turn reduce large-scale subsidence (Mapes 2001), assuming negligible temperature variations, thereby providing a link between clouds and the large-scale column moisture source (Chikira 2014). Local processes that

augment moist convection, e.g., mesoscale organized cloud systems and cold pools, can therefore communicate with the large-scale moisture source through such feedbacks.

One such process diagnosed in this study is the locally driven diurnal cycle. While net (i.e., daily-mean) column humidity changes are clearly linked to slowly evolving large-scale circulation in the MJO, the relative role of more rapid changes in convection due to the diurnal cycle is unclear. The diurnal cycle of convection can be pronounced in tropical suppressed regimes, and is in some respects unique from the archetypal nocturnal convective peak first documented by Gray and Jacobson (1977). In particular, during periods of light wind and strong insolation – namely, the suppressed phase of the MJO – the diurnal cycle of sea surface temperature (SST) can be very large (e.g., magnitudes of 2~3°C) as a result of shallow diurnal warm layers that develop due to strong daytime stabilization of the upper ocean (Bernie et al. 2005; Matthews et al. 2014). This diurnal cycle in SST, in turn, drives a pronounced daytime increase of surface fluxes, which in turn invigorates convection during the day (i.e., analogous to the diurnal cycle over land; Sui et al. 1997; Bellenger et al. 2010).

Previous studies demonstrate that this diurnal cycle in SST, wherein the heat received during the day in the shallow diurnal warm layer is convectively mixed downwards overnight, rectifies the slower (i.e., daily-mean) SST increase during the suppressed phase of the MJO (Webster et al. 1996; Duvel et al. 2004; Bernie et al. 2005, 2008; Vialard et al. 2009; Matthews et al. 2014). The question remains, however, as to whether or not the diurnal cycle of convection and associated diurnal column moisture variations can rectify onto longer timescales in a similar manner. This study represents a first step toward answering this question.

First, several in situ observational datasets from DYNAMO will be exploited to describe the large-scale evolution during the two observed MJO events and diagnose the relationship

between diurnally varying moist convection and column humidity during the MJO pre-onset stage (chapter 2). The observational findings set the stage for the subsequent modeling study (chapter 3), which is executed specifically to test a key hypothesis that derives from the observational results. Lastly, chapter 4 provides summary and conclusions of the overarching study findings, including future work and implications for the science.

## CHAPTER 2

# DIURNALLY MODULATED CUMULUS MOISTENING IN THE PREONSET STAGE OF THE MADDEN–JULIAN OSCILLATION DURING DYNAMO<sup>1</sup>

### *2.1 Introduction*

In this chapter, several datasets of in situ measurements from DYNAMO are employed (described in section 2.2), first to describe the general characteristics and evolution of the two observed MJO events (section 2.3), and second to describe the characteristics of the diurnal cycle and its role in modulating column humidity during the MJO suppressed phases (section 2.4). In the conclusions for this chapter (section 2.5), two new hypotheses are presented based on the observational results, one of which is tested in the modeling study that follows (chapter 3).

### *2.2 Data and methodology*

The primary DYNAMO observations employed in this study—those from a sounding network, a cloud-sensitive radar, and an air-sea flux site—are available from [http://data.eol.ucar.edu/master\\_list/?project=DYNAMO](http://data.eol.ucar.edu/master_list/?project=DYNAMO).

#### A) GRIDDED SOUNDING ANALYSIS

The Indian Ocean sounding network was composed of six sites, making two quadrilaterals straddling the equator, 500~800 km on a side. The signals of the two (Oct and Nov) MJO events analyzed herein were well sampled by the northern quadrilateral, while the southern quadrilateral sampled intermittent deep convection connected to the ITCZ (intertropical convergence zone) (Johnson and Ciesielski 2013). This study is therefore limited to the northern

---

<sup>1</sup> This chapter is comprised by content from Ruppert and Johnson (2015), ©American Meteorological Society. Used with permission.

quadrilateral (Fig. 2.1). This quadrilateral was comprised by three islands—Gan, Malé, and Colombo—and a ship—the R/V *Revelle*. Katsumata et al. (2011) demonstrate that a four-point quadrilateral array can accurately sample both the divergent and rotational flow components comprising the large-scale MJO circulation, while a triangular array does a poorer job. Therefore, periods when the R/V *Revelle* went offsite and the sounding array was reduced to three points are indicated in figures.

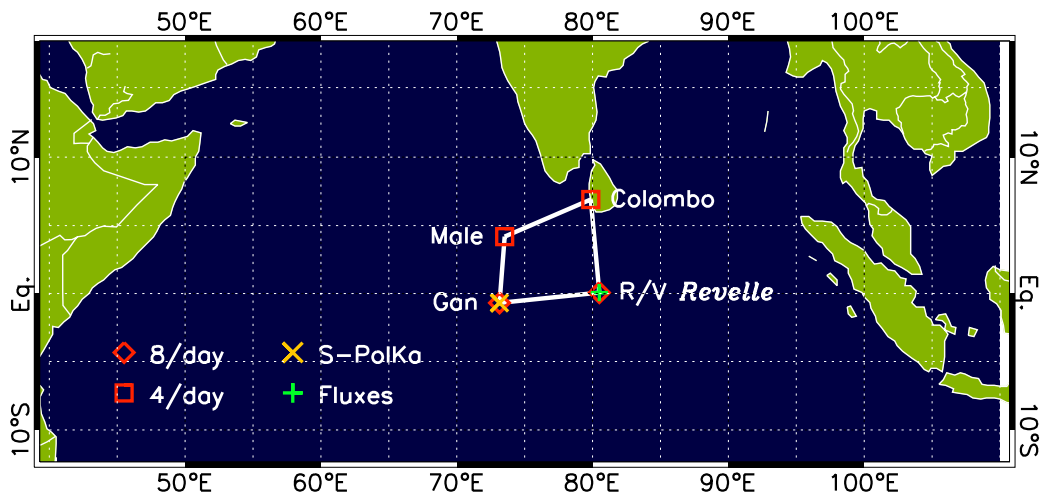


Fig. 2.1. DYNAMO northern sounding array for the period October–December 2011. Soundings were launched four–eight times per day, as indicated. Locations of the NCAR S-PolKa radar (Addu Atoll) and air-sea flux site (R/V *Revelle*) are also indicated.

A comprehensive set of quality-control techniques has been applied to the DYNAMO soundings, including mitigation of the low-level heat island and flow blocking effects in the Colombo soundings due to the large island of Sri Lanka (Ciesielski et al. 2014a,b). Following quality control, the sounding observations were horizontally interpolated onto a  $1^\circ$  mesh using the multiquadric objective analysis technique of Nuss and Titley (1994), and vertically interpolated onto an isobaric grid at 25-hPa spacing from 1000–50 hPa. Several observational datasets were included in the interpolation to supplement the primary soundings (dropsondes, satellite-derived vector winds, scatterometer surface winds, and thermodynamic profiles from

radio occultation measurements), the details of which are provided in a companion paper by Johnson et al. (2015). Vertical pressure velocity  $\omega$  was calculated by vertically integrating divergence from the surface to the tropopause (with adiabatic flow assumed at the tropopause), with mass-balance applied using a constant divergence correction (O'Brien 1970). The gridded analysis was then spatially averaged over the northern sounding array to yield a time–pressure series of northern-array mean quantities.

During the special observing period (SOP: 1 Oct–15 Dec), soundings were launched eight (four) times per day at the equatorial (northern) sites (Fig. 2.1), though on 8 Dec launches at Colombo reduced to one per day. Therefore, the analysis is carried out for 1 Oct–7 Dec. Temporal interpolation was carried out to generate data at three-hourly frequency at the two northern sites (Fig. 2.1). This procedure was crucial for exploiting the three-hourly information from the two equatorial sites, which resulted in markedly improved sampling of the diurnal cycle. The interpolation was performed for the analysis times of 0300, 0900, 1500, and 2100 UTC using the two soundings from three hours prior to and following the given analysis time for the respective site (interpolation was not performed if either of these two soundings were missing). The error due to this procedure was assessed by exploiting the three-hourly soundings at Gan. RMS differences between actual and contemporaneous Gan soundings generated by this procedure amounted to  $\sim 0.5^{\circ}\text{C}$ ,  $0.5 \text{ g kg}^{-1}$ , and  $1 \text{ m s}^{-1}$  in temperature, specific humidity, and wind speed, respectively, which are inconsequential for the objectives of this study.

Similar analysis approaches to those described above have been successfully applied in many previous tropical and monsoon field campaigns (e.g., the Tropical Ocean Global Atmosphere Coupled Ocean–Atmosphere Response Experiment, or COARE, the South China Sea Monsoon Experiment, the North American Monsoon Experiment, and the Terrain-influenced

Monsoon Rainfall Experiment), which have confirmed the reliability of results via comparison with independent observations (Lin and Johnson 1996a,b; Johnson and Ciesielski 2002; Ciesielski et al. 2003; Johnson et al. 2010; Ruppert et al. 2013). Detailed comparisons between the DYNAMO gridded sounding analysis and independent datasets are provided by Johnson et al. (2015), and are not repeated here. Provided in section 3, however, is a comparison between budget-derived and satellite-estimated rainfall.

## B) RADAR CLOUD MEASUREMENTS

The behavior of clouds is assessed using measurements from the National Center for Atmospheric Research (NCAR) dual-polarimetric and dual-frequency (10 cm: S band, and 8 mm: Ka band) S-PolKa weather research radar (Keeler et al. 2000), which was deployed during DYNAMO on Addu Atoll, Maldives, at 0.63°S, 73.10°E (to the northwest of Gan Island). (Only information from the S band is employed in this study.) The details of S-PolKa data quality control and field instrumentation management can be found at <https://www.eol.ucar.edu/instrumentation/remote-sensing/s-pol> and in prior studies (Powell and Houze 2013; Zuluaga and Houze 2013; Rowe and Houze 2014). When viewing S-PolKa data in this study, the caveat that the S-PolKa sampling region is far smaller than and on the corner of the northern sounding array must be considered. Slight inconsistencies in the timing between northern array-averaged quantities and radar quantities are possible due to this issue.

Owing to its high sensitivity, the S-PolKa radar detects non-precipitating clouds, which are important for moistening the troposphere to offset the drying by large-scale subsidence (Nitta and Esbensen 1974; Johnson and Lin 1997). This study employs the range–height indicator (RHI) echo measurements from the S-PolKa northeastern quadrant dataset, which is composed of vertical slices over azimuths from 4°–82° (where there is minimal ground clutter) at 2°

intervals, up to an elevation angle of  $40^\circ$ , and at 15-min sampling frequency. The maximum range of the RHI measurements is 150 km, though data are only retained within a 50-km range for this analysis, as advised by Feng et al. (2014). A subset of hydrometeor echo-base and echo-top height measurements is assembled from the dataset following interpolation of the data onto a Cartesian grid of 500-m vertical–horizontal spacing. Echo base and top are defined as the vertical boundaries of contiguous detectable echo return, with a minimum echo threshold of  $-30$  dBZ (Feng et al. 2014). Then, echo features with a base elevation  $\leq 1$  km and vertical depth  $\geq 1.5$  km are isolated, thereby excluding very thin clouds and the majority of Bragg scattering layers related to detrained moisture and turbulent mixing across vertical moisture gradients (Davison et al. 2013). Therefore, what are retained are boundary layer-based clouds and high-based clouds with contiguous detectable rain shafts. During suppressed periods, when rainfall is minimal and stratiform systems rare, these echo features are dominated by boundary layer-based convective clouds (Barnes and Houze 2013; Powell and Houze 2013; Zuluaga and Houze 2013; Rowe and Houze 2014).

*Echo-top frequency* is calculated from the above-described subset of echo features by counting the total occurrences of echo top at each vertical level as a function of time, and normalizing this result by the total number of grid bins in the horizontal plane. *Echo area coverage* is calculated from the same subset by dividing the total number of horizontal grid points containing echo (at any level, subject to the above criteria) by the total number of grid points in the horizontal plane.

### C) AUXILIARY DATASETS

High-time-resolution (10-min) surface thermodynamic variables were collected during DYNAMO at the R/V *Revelle* (Fig. 2.1). The measurements employed herein include sea

surface temperature (SST; following an adjustment to skin temperature), surface sensible and latent heat flux, wind speed, wind stress, and 10-m air temperature and humidity. Daily-mean latent heat flux from the TropFlux product (Praveen Kumar et al. 2011) is employed following an average over the northern sounding quadrilateral to facilitate the estimation of rainfall from the moisture budget. The TRMM (Tropical Rainfall Measurement Mission; Kummerow et al. 2000) 3B42v7 rainfall product (three-hourly frequency; Huffman et al. 2007) is employed, following an average over the northern sounding quadrilateral, for comparison with budget-derived rainfall. Orbit swath true-color images from MODIS (Moderate Resolution Imaging Spectroradiometer) are also employed, which were collected from <http://lance-modis.eosdis.nasa.gov/cgi-bin/imagery/realtime.cgi>.

### 2.3 Overview of the DYNAMO MJO events

Two MJO events were sampled by the DYNAMO northern sounding array during its full operation (Oct: MJO1; Nov: MJO2). The two MJO events are depicted in Fig. 2.2 as periods of very dry conditions (i.e., relative humidity  $RH < 50\%$ ) through a deep layer with little rainfall, followed by very moist conditions (i.e.,  $RH > 70\%$ ) through most of the column with enhanced rainfall. These are the *suppressed phase* (MJO1: early–mid Oct; MJO2: mid Nov) and *active phase* (MJO1: late Oct–early Nov; MJO2: late Nov), respectively, which are separated by the vertical lines marking MJO onset in Fig. 2.2. (MJO onset, the MJO sub-periods, and budget-derived rainfall  $P_0$ , as depicted in Fig. 2.2, are explicitly defined later.) Dry conditions (i.e.,  $RH < 50\%$ ) reach down to  $\sim 800$  hPa during the suppressed phase of MJO1, while dry conditions only reach  $\sim 550$  hPa during that of MJO2. Differences in MJO event duration are also apparent, with both the suppressed and active phases of MJO1 outlasting those of MJO2 by roughly one week.

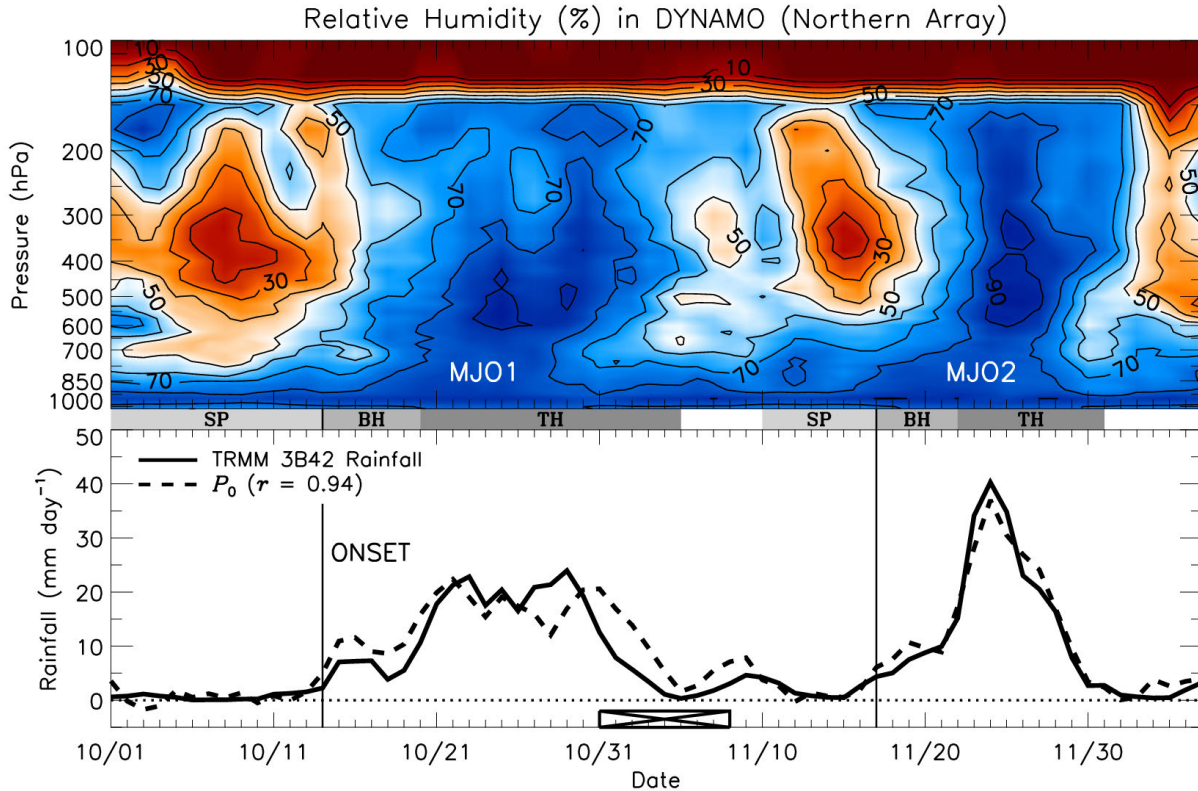


Fig. 2.2. (top) Time–pressure series of daily-mean relative humidity RH (every 10%; with respect to ice where temperature  $< 0^{\circ}\text{C}$ ) from the northern-array gridded analysis. (bottom) Daily-mean rainfall estimates ( $\text{mm day}^{-1}$ ) from TRMM 3B42 (solid) and the moisture budget  $P_0$  (dashed). All fields temporally smoothed using a three-day running mean (smoothing in this and subsequent figures is applied using the “boxcar” technique). Correlation  $r$  between the smoothed rainfall estimates is indicated (significant to the 99%-level). Here and in subsequent figures: “SP” refers to suppressed periods, and “BH” (“TH”) to periods of bottom-heavy (top-heavy) apparent heating, drying, and vertical motion profiles (Figs. 2.3 and 2.4); the black “X” along the lower abscissa indicates periods when the *Reville* was on port call; and the vertical solid lines denote MJO onset (i.e., see text for definition).

The bottom-up moistening that commences during the suppressed phase (Fig. 2.2) has been noted in numerous studies, and likely relates to the deepening of convective clouds during this period (Lin and Johnson 1996a,b; Johnson et al. 1999; Kikuchi and Takayabu 2004; Kiladis et al. 2005; Benedict and Randall 2007; Haertel et al. 2008). The character of this low-to-midlevel moistening differs between MJO1 and MJO2, as described later. Moistening from aloft can also be noted in Fig. 2.2 (e.g., from 15~20 Nov in the layer 150–300 hPa). Studies have

related this moistening to the gravity-wave or Kelvin-wave response to the convective envelope of previous MJO convective events (Kiladis et al. 2001; Gottschalck et al. 2013; Johnson and Ciesielski 2013). Studies have also linked such gravity waves to the observed increase in cirrus clouds in the upper troposphere–lower stratosphere in the days–weeks prior to the MJO active phase, which can be observed as far as 30° east of the MJO convective envelope (Virts and Wallace 2010; Virts et al. 2010; Riley et al. 2011; Del Genio et al. 2012).

Figure 2.3 provides DYNAMO daily-averaged time–pressure series of the apparent heat source  $Q_1$  and apparent moisture sink  $Q_2$ , calculated according to Yanai et al. (1973):

$$Q_1 \equiv \frac{D\bar{s}}{Dt} = \frac{\partial \bar{s}}{\partial t} + \bar{\mathbf{v}} \cdot \nabla \bar{s} + \bar{\omega} \frac{\partial \bar{s}}{\partial p} = Q_R + L_v (\bar{c} - \bar{e}) - \frac{\partial}{\partial p} (\overline{\omega' s'}), \quad (2.1)$$

$$Q_2 \equiv -L_v \frac{D\bar{q}}{Dt} = -L_v \left( \frac{\partial \bar{q}}{\partial t} + \bar{\mathbf{v}} \cdot \nabla \bar{q} + \bar{\omega} \frac{\partial \bar{q}}{\partial p} \right) = L_v (\bar{c} - \bar{e}) + L_v \frac{\partial}{\partial p} (\overline{\omega' q'}), \quad (2.2)$$

with  $s = c_p T + gz$  dry static energy,  $c_p$  the specific heat of dry air at constant pressure,  $T$  temperature,  $g$  gravity,  $z$  height,  $\mathbf{v}$  horizontal flow,  $\omega$  vertical pressure velocity (Fig. 2.4),  $Q_R$  radiative heating,  $L_v$  the latent heat of vaporization at 0°C,  $c$  ( $e$ ) hydrometeor condensation (evaporation) rate, and  $q$  water vapor mixing ratio. Overbars denote a spatial average over the northern sounding array, and primes deviations from that average. The heat and moisture source terms related to horizontal eddies and ice-phase processes do not appear in (2.1) and (2.2), although they can be included (Arakawa and Schubert 1974; Yanai and Johnson 1993). The LHS of (2.1) and (2.2) are calculated directly from the gridded analysis.

MJO1 and MJO2 appear clearly in Fig. 2.3 and the time series of  $\omega$  in Fig. 2.4.  $Q_1$  and  $Q_2$  are negative through most of the troposphere during the suppressed phases in connection with radiative cooling and moistening by clouds under subsidence; and  $Q_1$  and  $Q_2$  are positive during the two active phases, reflecting the large latent heating and drying due to precipitation with

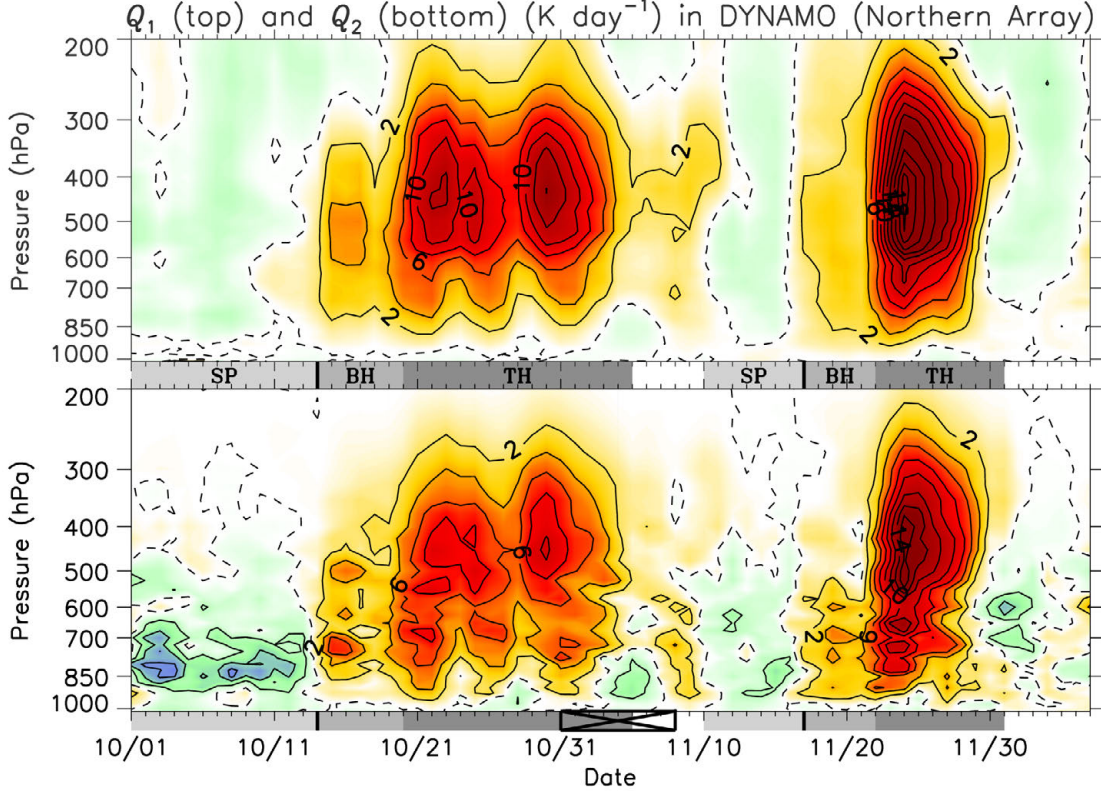


Fig. 2.3. Daily-mean time–pressure series of the apparent heat source  $Q_1$  (top) and apparent moisture sink  $Q_2$  (bottom) (contoured every  $2 \text{ K day}^{-1}$  and shaded with positive values in red)<sup>2</sup>. The zero contour is dashed. Three-day temporal smoothing applied.

strong ascent. *MJO onset* henceforth refers to the time at which subsidence and apparent cooling and moistening switch to ascent and heating and drying (MJO1: 14 Oct; MJO2: 17 Nov; ascertained from unsmoothed, column-integrated fields), as indicated in the relevant figures. As Yanai et al. (1973) show, the vertically integrated budgets can be written as

$$\langle Q_1 \rangle = \langle Q_R \rangle + \langle L_v (\bar{c} - \bar{e}) \rangle - \left\langle \frac{\partial}{\partial p} (\overline{\omega' s'}) \right\rangle = \langle Q_R \rangle + L_v P_0 + S_0, \quad (2.3)$$

$$\langle Q_2 \rangle = \langle L_v (\bar{c} - \bar{e}) \rangle + \left\langle L_v \frac{\partial}{\partial p} (\overline{\omega' q'}) \right\rangle = L_v (P_0 - E_0), \quad (2.4)$$

where

<sup>2</sup>  $Q_1$  and  $Q_2$ , as defined in (1) and (2), have been multiplied by the factor  $8.64 \times 10^4 c_p^{-1}$  for presentation in  $\text{K day}^{-1}$ .

$$\langle \rangle \equiv \frac{1}{g} \int_{p_T}^{p_{sfc}} ( ) dp,$$

$P_0$  is precipitation,  $S_0$  is surface sensible heat flux,  $E_0$  is surface evaporation rate,  $p_{sfc}$  is surface pressure, and  $p_T$  is 100 hPa (results insensitive to the choice of  $p_T$ ).  $P_0$ , shown in Fig. 2.2, is calculated from (2.4) using  $E_0$  from TropFlux averaged over the northern sounding array. The Pearson's correlation coefficient  $r$  between TRMM rainfall and  $P_0$  is 0.94 (significant to the 99% level using the Student's t-test and assuming a sample size of seven, the approximate number of ten-day periods in the dataset). There are times when  $P_0$  is slightly negative or departs measurably from TRMM rainfall, which could owe to any of several factors: observational sampling errors (Mapes et al. 2003), inaccuracies in  $E_0$  from TropFlux, changes in cloud volume (which break the assumption that  $P_0 = \langle \bar{c} - \bar{e} \rangle$ ; McNab and Betts 1978), or inaccuracies in TRMM rainfall (Liu et al. 2007). The marked agreement between  $P_0$  and TRMM rainfall, however, lends confidence to the gridded sounding analysis, and the moisture budget described next (see Johnson et al. 2015 for more detailed budget validation).

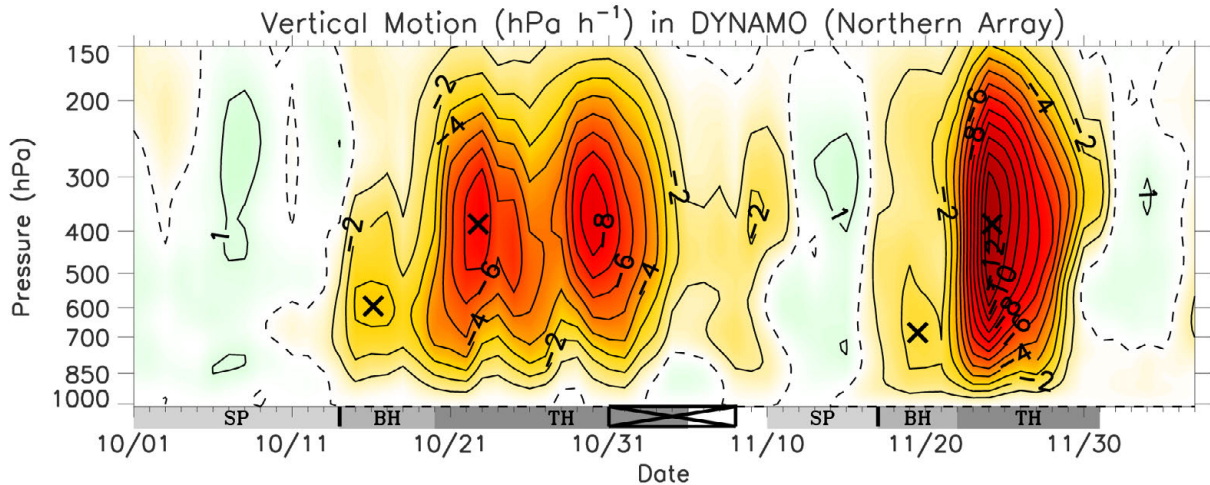


Fig. 2.4. As in Fig. 2.3 except for vertical pressure velocity  $\omega$  (contoured every 2 hPa h<sup>-1</sup> and shaded with negative values in red). X's are placed in several locations to highlight the level of maximum ascent.

Presented next is the column-integrated water vapor budget (Fig. 2.5), which is employed in lieu of the column-integrated MSE budget (Sobel et al. 2014) since the latter hides the direct effects of clouds (i.e., the moistening/drying due to liquid–vapor phase changes). Furthermore, in the column-integrated MSE budget, vertical dry static energy advection typically cancels with moisture advection in the vertical advection term, therefore potentially hiding the role of vertical advection. From (2) and (4), the column-integrated water vapor budget can be written as

$$\begin{aligned} \left\langle \frac{\partial L_v \bar{q}}{\partial t} \right\rangle &= -\langle \bar{\mathbf{v}} \cdot \nabla L_v \bar{q} \rangle - \left\langle \bar{\omega} \frac{\partial L_v \bar{q}}{\partial p} \right\rangle - \langle Q_2 \rangle \\ &= -\langle \bar{\mathbf{v}} \cdot \nabla L_v \bar{q} \rangle - \left\langle \bar{\omega} \frac{\partial L_v \bar{q}}{\partial p} \right\rangle + L_v (E_0 - P_0). \end{aligned} \quad (2.5)$$

According to (5), moistening/drying (in the Eulerian framework) is driven by horizontal and vertical advection (first and second RHS terms), as well as surface evaporation and precipitation (third and fourth RHS terms), or the *apparent* source and sink, respectively. Since, on the large scale, clear-air vertical motion is downward in the tropics (i.e., drying), moistening via vertical advection (i.e., ascending motion) in (2.5) should be regarded as the upward flux of moisture and evaporation of detrained hydrometeors by clouds, which in such cases dominate the sampled divergent circulation (e.g., Arakawa and Schubert 1974; Yanai et al. 1973; Chikira 2014). While the budget terms (as shown in Fig. 2.5) are smoothed, no means are removed; therefore, their individual contributions to column moistening are conveyed in the absolute sense.

Before discussing the individual terms in the moisture budget, three subdivisions of each MJO event are defined based on several key characteristics and transition points depicted in Figs. 2.2–2.4 (ascertained from unsmoothed fields). These subdivisions are depicted by shaded bars in all relevant figures. The suppressed phases (“SP”) are identified as the periods in which  $\langle Q_2 \rangle < 0$  and subsidence prevails prior to MJO onset (1–13 Oct and 10–16 Nov; end-dates are

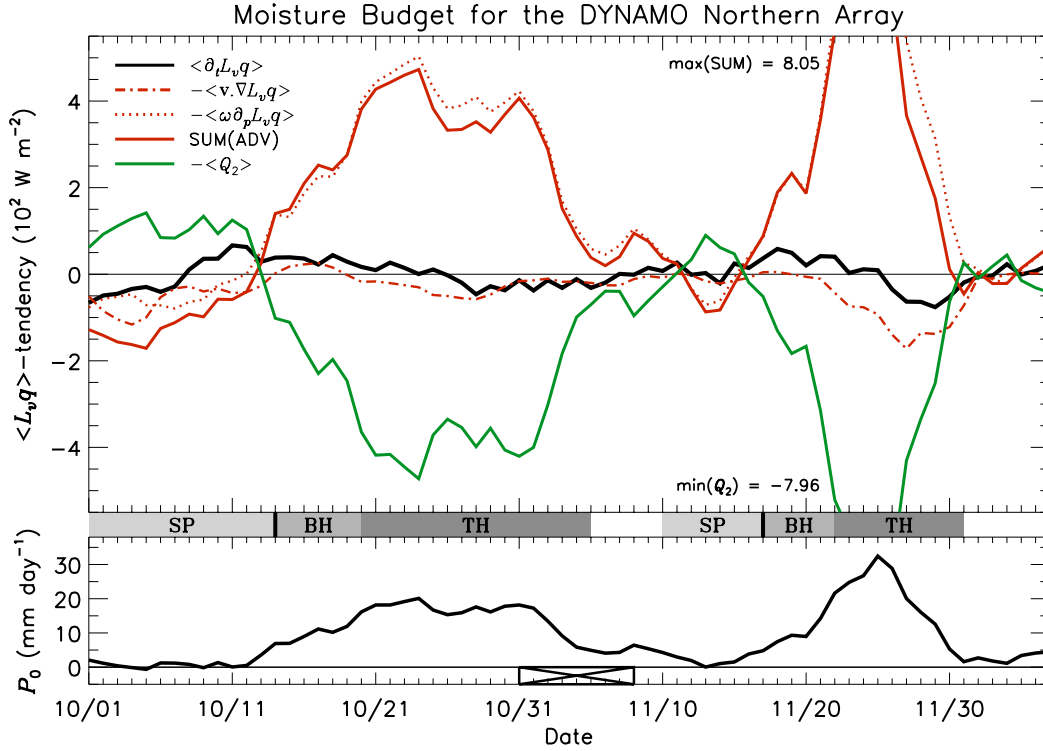


FIG. 2.5. (top) Daily-mean vertically integrated water vapor budget ( $10^2 \text{ W m}^{-2}$ ) and (bottom) budget rainfall  $P_0$  ( $\text{mm day}^{-1}$ ). Budget terms are calculated as shown in eqn. (5), with the Eulerian tendency (black), horizontal advection (red, dot-dashed), vertical advection (red, dotted), the sum of horizontal and vertical advection (SUM(ADV); red, solid), and apparent sources (green). Maximum and minimum values for terms exceeding the ordinate scale are indicated. Five-day temporal smoothing has been applied to all fields.

inclusive). These periods are analogous to the *pre-onset stage* in DYNAMO parlance (Yoneyama et al. 2013). The active phases are split into two sub-periods each. The first sub-periods are those with relatively more bottom-heavy  $Q_1$ ,  $Q_2$ , and  $\omega$  profiles (“BH”; 14–19 Oct and 17–21 Nov), which correspond with positive moisture (i.e.,  $L_v q$ -) tendency (Fig. 2.5). The second are those characterized by top-heavy  $Q_1$ ,  $Q_2$ , and  $\omega$  profiles (“TH”), which exhibit progressively decreasing moisture tendency (20 Oct–4 Nov and 22–30 Nov).

The signs of  $Q_1$  and  $Q_2$  during SP (Fig. 2.3), together with the knowledge that  $P_0 \sim 0$  (Fig. 2.2), imply specifically which heat and moisture sources/sinks are at play. From (2.3), the magnitude of  $\langle Q_R \rangle$  must exceed that of  $S_0$ , assuming  $S_0 > 0$ . From (2.4), the moistening signal in

$Q_2$  owes primarily to  $E_0 > 0$ . Figure 2.5 reveals that this evaporative moistening works in opposition to the drying by subsidence and horizontal advection. These terms are  $O(100 \text{ W m}^{-2})$  of moistening and drying, respectively. [Motivated by a reviewer comment, we have confirmed that  $L_v E_0$  calculated from TropFlux agrees very well with the magnitude of  $-\langle Q_2 \rangle$  during SP in Fig. 2.5. This comparison is roughly equivalent to comparing TRMM rainfall and  $P_0$ , as in Fig. 2.2, since  $P_0$  is calculated using TropFlux in  $\langle Q_2 \rangle / L_v + E_0$ , from (2.4).] The quasi-balance between large-scale drying and cumulus moistening is reminiscent of the tropical trade cumulus regimes described previously, though horizontal advection typically plays a smaller role in such regimes (Nitta and Esbensen 1974; Johnson and Lin 1997).

In SP/MJO1, the moisture tendency becomes positive around 7 Oct (Fig. 2.5). The low-to-mid-tropospheric moistening observed during the subsequent ~six days (Fig. 2.2) is accomplished by surface evaporation (2.4), or alternatively, vertical eddy cloud transport (2.2), which overcomes the drying by large-scale circulation (Figs. 2.4 and 2.5). The waning of subsidence and horizontal-advective drying, while cumulus moistening persists, orchestrates the evolution of the moisture tendency, indicating the key role of large-scale circulation changes. In contrast to SP/MJO1, a period of moistening takes place early in SP/MJO2 (i.e., from 850~550 hPa), followed by a persistent period of relatively moist conditions compared to SP/MJO1 (i.e.,  $\text{RH} \geq 50\%$  up to ~550 hPa), followed again by moistening beginning shortly before onset (Figs. 2.2 and 2.5). In spite of these differences between SP/MJO1 and SP/MJO2, the role of large-scale circulation is similar, in that column moistening is facilitated by the waning of large-scale drying (subsidence acts as the primary drying agent during SP/MJO2; Fig. 2.5).

At the time of onset in both MJOs,  $Q_2$  switches to large drying due to rainfall as vertical advection switches to a large moisture source of  $O(500 \text{ W m}^{-2})$  (Fig. 2.5). Horizontal advection

is very weakly moistening in BH/MJO1. The moisture tendency remains positive during BH in both MJOs, reflecting the full-column moistening as depicted in Fig. 2.2. This second stage of moistening is accomplished in the presence of relatively bottom-heavy convection (Figs. 2.3 and 2.4), indicative of predominant congestus and cumulonimbus clouds. The relatively bottom-heavy heating implies that convective inflow (i.e., convergence) is focused over a relatively shallow depth of the lower-troposphere, leading to a larger moisture source than a heating profile with a higher peak (i.e., as in stratiform precipitating systems) (Wu 2003; Zhang et al. 2004).

During TH, the moisture tendency becomes negative, aided by increased horizontal-advective drying. This drying likely reflects the dry-air intrusions associated with equatorward advection in Rossby gyres on the west side of the active phase (Gill 1980; Chen et al. 1996; Maloney and Hartmann 1998; Benedict and Randall 2007; Gottschalck et al. 2013; Kerns and Chen 2014). Unsaturated downdrafts in stratiform precipitation systems also likely assist the drying (Figs. 2.3 and 2.4) (Zipser 1977; Barnes and Houze 2013; Zuluaga and Houze 2013; Chikira 2014; Rowe and Houze 2014). The end of each active phase is met with a return to conditions characteristic of SP.

A DYNAMO time series of echo-top frequency and echo area coverage (cf. section 2) is provided in Fig. 2.6. An abundance of short-timescale variability is clear in echo-top frequency, particularly the two-day modes during the active phase of MJO1, likely related to the westward-propagating two-day waves described in past studies (Haertel et al. 2008; Johnson and Ciesielski 2013; Zuluaga and Houze 2013). There is also a clear, slower evolution of convection related to the MJO. Shallow cumulus and congestus clouds with tops  $< 10$  km prevail during SP, with a progressive deepening of clouds prior to and around MJO onset. Clouds are generally deeper in SP/MJO2, consistent with a deeper moist layer (Fig. 2.2). Echo tops  $> 12$  km prevail thereafter

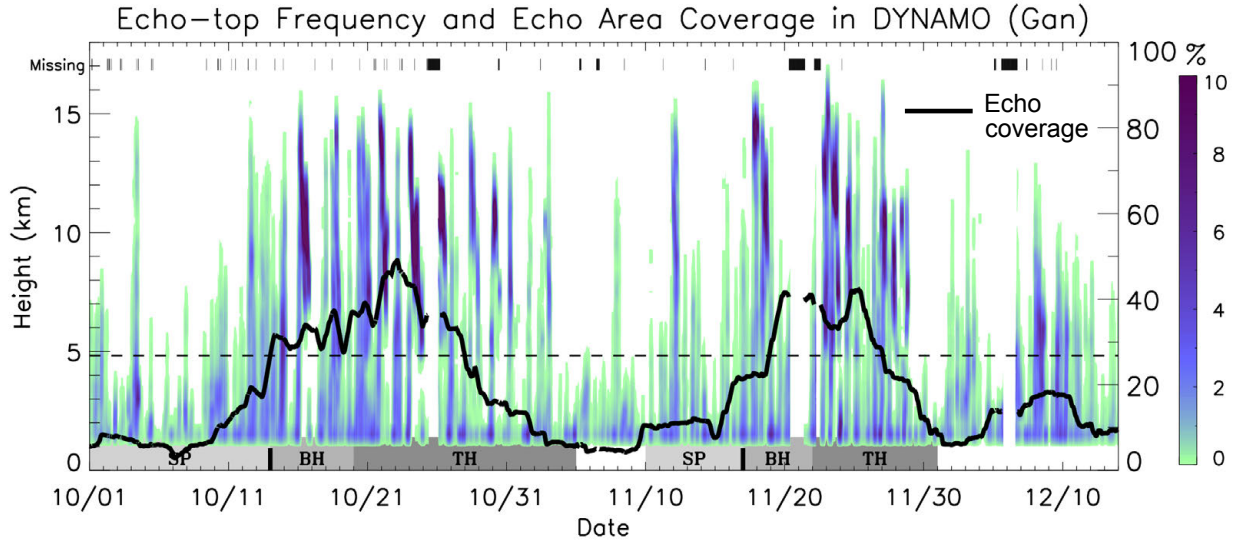


Fig. 2.6. Time–height series of echo-top frequency and echo area coverage (%) from 15-min S-PolKa RHI data (cf. section 2 for methodology). Temporal smoothing has been applied to echo-top frequency (echo area coverage) using a six-hour (five-day) running mean. Black hashes near the top indicate time periods of missing data (where the time gap between scans exceeded 23 min). The dashed line indicates the 0°C level.

during the active phase. Echo area coverage increases from ~10 to ~30% during this transition, indicating that cloud systems are both deepening (in echo-top height) and increasing in abundance and/or size leading up to and shortly after MJO onset. Echo area coverage maximizes around 50% early in TH/MJO1, with dual peaks of ~40% in BH and TH/MJO2. Echo-area coverage, diabatic heating (Fig. 2.3), column humidity (Figs. 2.2 and 2.5), and rainfall all exhibit close correspondence in both tendency and time of peak values. These findings are generally consistent with those of Xu and Rutledge (2014).

The findings of this section demonstrate that moistening of the troposphere in the MJO pre-onset stage is orchestrated by simultaneous changes in large-scale circulation and the convective cloud population. While there are differences between the suppressed phases of MJO1 and MJO2 (i.e., in the character and duration of moistening and depth of the moist layer; Fig. 2.2), the role of large-scale circulation is similar in both. Namely, moistening of the low–

midtroposphere (Fig. 2.2) is accomplished by the waning of drying due to subsidence and horizontal advection (Figs. 2.4 and 2.5) as the population of convective clouds is simultaneously invigorated. Invigoration of the cloud population is manifest in a deepening and increase in the areal coverage of clouds (Fig. 2.6). Moistening of the full column takes place after MJO onset (BH) in connection with relatively bottom-heavy diabatic heating, suggesting abundant congestus and cumulonimbus clouds and minimal stratiform rainfall (Fig. 2.3). The magnitude of diabatic heating increases with time as column humidity and echo area coverage increase from BH into TH (though there is an earlier peak in echo coverage in BH/MJO2). Column drying begins during TH in connection with top-heavy diabatic heating, and is assisted by increased horizontal dry-air advection. Rainfall approximately correlates with column humidity, therefore maximizing around the time that column moistening completes (i.e., early in TH). This evolution is consistent with previous studies (Maloney and Hartmann 1998; Johnson et al. 1999; Benedict and Randall 2007; Del Genio et al. 2012; Barnes and Houze 2013; Johnson and Ciesielski 2013; Zuluaga and Houze 2013; Xu and Rutledge 2014).

Variations in both vertical and horizontal advection are important, consistent with the findings of Sobel et al. (2014). Horizontal advection, as depicted in Fig. 2.5, is largely manifest in a waxing and waning of drying related to enhanced (suppressed) equatorward dry-air advection due to Rossby wave activity during the late-active phase (pre-onset stage) (Gottschalck et al. 2013; Kerns and Chen 2014). Studies demonstrate that enhanced anomalous horizontal-advective drying (moistening) is associated with enhanced westerly (easterly) flow (Johnson and Ciesielski 2013; Kerns and Chen 2014; Sobel et al. 2014). The waning of subsidence during the pre-onset stage may be linked to both remote and local effects. Eastward-propagating gravity or Kelvin waves are likely important for decreasing upper-level convergence prior to onset (Kiladis

et al. 2001; Virts and Wallace 2010; Virts et al. 2010; Gottschalck et al. 2013; Johnson and Ciesielski 2013). Observations depict a reduction in outgoing longwave radiation during the pre-onset phase (Sobel et al. 2014; Johnson et al. 2015). This reduction in column radiative cooling – likely driven by the local invigoration of moist convection (Fig. 2.6) and/or development of high cirrus clouds during the pre-onset stage (Virts and Wallace 2010; Virts et al. 2010) – must equate to reduced large-scale subsidence when temperature variations are assumed negligible (Mapes 2001; Chikira 2014).

Since the local invigoration of moist convection during the pre-onset stage is intimately linked with the coinciding humidification of the low–midtroposphere (Figs. 2.2, 2.5, and 2.6), a better understanding of the key physics in MJO onset may come from improved understanding of this convective invigoration. The next section of this study exploits the unique opportunity afforded by DYNAMO to describe the local influences on convective invigoration in MJO onset. The findings will demonstrate that moist convection exhibits a pronounced locally driven diurnal cycle, with cumulus invigoration occurring distinctly each afternoon in response to the formation of oceanic diurnal warm layers. This diurnal cycle drives a major component of Eulerian column humidity variations during the pre-onset stage.

#### *2.4 The diurnal cycle of cumulus moistening*

Time series of the column-integrated Eulerian moisture tendency, i.e.,  $\langle \partial \bar{q} / \partial t \rangle$ , spanning the two MJO suppressed phases reveal the importance of short-timescale variability during these periods (Fig. 2.7). There is a clear prominence of cyclic variability with period  $\leq 24$  h. Comparison between the unfiltered Eulerian tendency and the same term smoothed with a 24-h running mean, i.e.,  $\langle \partial \bar{q} / \partial t \rangle_{\text{DAILY}}$ , confirms this point (Fig. 2.7). The variance of  $\langle \partial \bar{q} / \partial t \rangle$  over

the period 1 Oct–7 Dec is  $\sim 74$  ( $\text{mm day}^{-1}$ )<sup>2</sup>, compared to  $\sim 9$  ( $\text{mm day}^{-1}$ )<sup>2</sup> in  $\langle \partial \bar{q} / \partial t \rangle_{\text{DAILY}}$ ; in other words, 90% of the total variance of the Eulerian column moisture tendency is explained by diurnal and sub-diurnal variability during these periods (this fraction exceeds 90% when the periods shown in Fig. 2.7 are isolated for the variance calculations). The diurnal cycle in the advective moisture source is negligible (not shown), corroborating that the diurnal cycle is primarily locally driven.

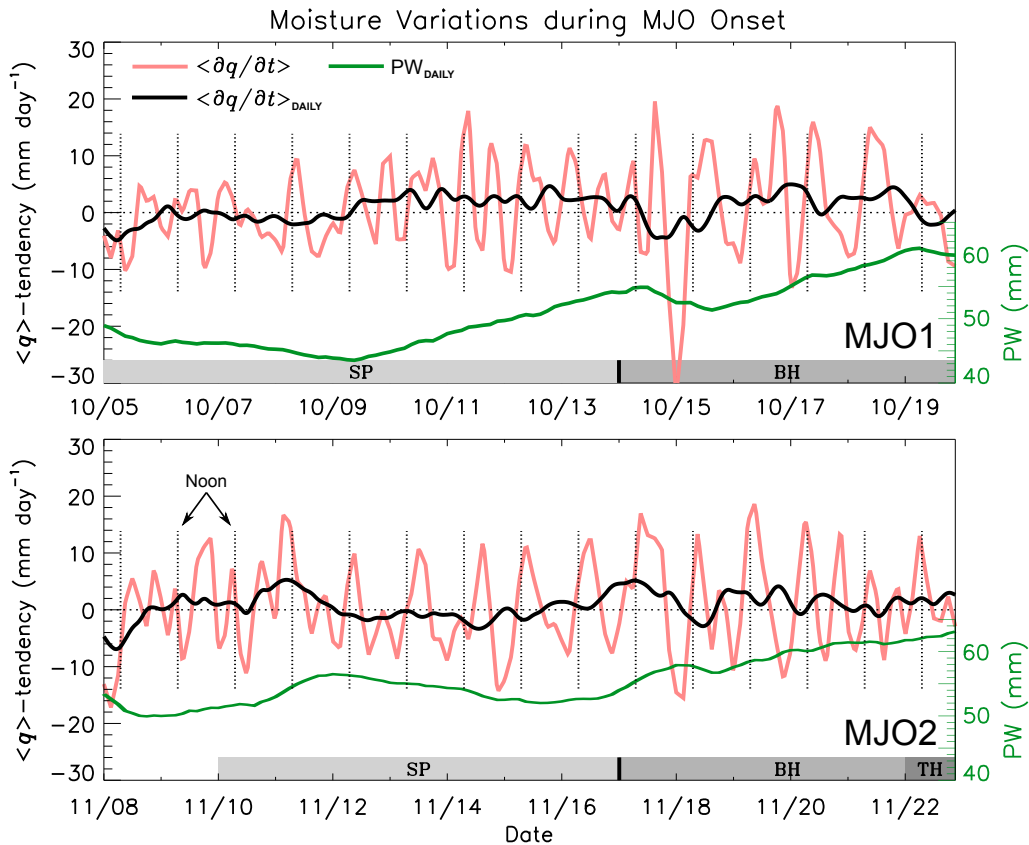


Fig. 2.7. Time series of the northern-array mean, column integrated Eulerian moisture tendencies ( $\text{mm day}^{-1}$ ; left axis) spanning convective onset in (top) MJO1 and (bottom) MJO2.  $\langle \partial q / \partial t \rangle$  (red) denotes the three-hourly Eulerian tendency, and  $\langle \partial q / \partial t \rangle_{\text{DAILY}}$  (black) is the same except smoothed using a 24-h running mean. Precipitable water (PW; green; mm; right axis) is also shown. The dotted vertical lines denote local noon.

While there are differences between the two MJO events (e.g., greater semidiurnal variability in SP/MJO1), the diurnal cycle is clearly important, with moistening often peaking in the afternoon (Fig. 2.7). The relationships between independent datasets portray a coherent diurnal cycle in moist convection, as will be demonstrated. This diurnal cycle, with pronounced afternoon convection, implies the importance of daytime upper-ocean warming (Sui et al. 1997). In this sense, the diurnal cycle differs from that of more disturbed tropical oceanic regimes, wherein overnight convective activity dominates due to enhanced oceanic mixing (i.e., prevention of large diurnal SST swings) and nocturnally maximized radiative cooling from the upper part of clouds (Gray and Jacobson 1977; Randall et al. 1991; Xu and Randall 1995; Chen and Houze 1997; Sui et al. 1998; Dai 2001; Yang and Smith 2006; Johnson 2011).

A time series of SST from the R/V *Revelle* during DYNAMO depicts a very prominent diurnal cycle (Fig. 2.8). The diurnal cycle is most regular and/or largest during the suppressed periods when  $SST_{\text{daily}}$  (SST smoothed with a 24-h running mean) is climbing, with the greatest diurnal increase appearing on 16 Nov, from 29.3–32.1°C over the period 0650–1530 LT, i.e., a remarkable increase of 2.8°C in 9 h. Similar rapid warming was observed during light-wind periods in COARE (Weller and Anderson 1996). These large diurnal SST swings occur under clear, light-wind conditions owing to the formation of upper-ocean diurnal warm layers, whereby daytime heating stabilizes the upper ocean, inhibits vertical mixing, and hence concentrates subsequent solar heating to within this surface layer (Halpern and Reed 1976; Stramma et al. 1986; Flament et al. 1994; Webster et al. 1996; Weller and Anderson 1996; Kawai and Wada 2007; Bellenger et al. 2010; Matthews et al. 2014). Studies demonstrate that this diurnal cycle is key to rectifying the slower (i.e., daily-mean) warming preceding MJO onset (Bernie et al. 2005;

Matthews et al. 2014). Greater wind speeds limit the diurnal SST range by enhancing vertical mixing (e.g., compare SP/MJO1 with SP/MJO2; Fig. 2.8).

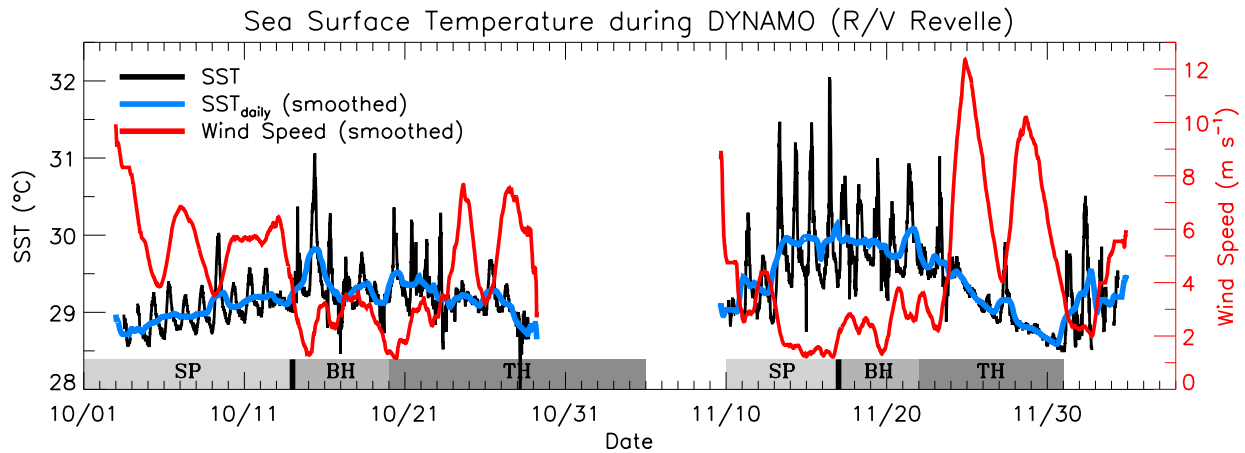


Fig. 2.8. Time series of ten-minute frequency sea surface temperature (SST, adjusted to skin temperature; black; °C; left axis), SST smoothed using a 24-h running mean ( $SST_{\text{daily}}$ ; blue), and surface wind speed smoothed using a 24-h running mean (red;  $\text{m s}^{-1}$ ; right axis) from the *Reville* flux site (Fig. 2.1).

Time series of surface flux measurements from the R/V *Reville* spanning SP/MJO1 (Fig. 2.9) and SP/MJO2 (Fig. 2.10) corroborate the prominence of the diurnal cycle during these periods. During SP/MJO1, sensible heat flux ( $S_0$ ) and 10-m air temperature often exhibit diurnal cycles closely following that of SST, though wind speed and latent heat flux ( $L_v E_0$ ) are dominated by longer-timescale variability. During SP/MJO2, however, SST, air temperature,  $S_0$ ,  $L_v E_0$ , and wind speed all exhibit clear, coherent diurnal cycles in the four days leading up to MJO onset. The relationship between variables is more clearly depicted in Fig. 2.11, which shows anomaly diurnal composites over the strongly diurnally modulated days (MJO1: 6–11 Oct; MJO2: 13–16 Nov).<sup>3</sup> These composites are calculated by averaging the time series as a function of time of day and removing the composite mean (the calculations were also carried out by

<sup>3</sup> Note that the selected date ranges for diurnal composites differ between some figures (i.e., Figs. 2.11, 2.14, 2.15, and 2.16). This is unavoidable when aiming to isolate diurnal variability, and in datasets with differing sampling regions.

removing daily means first to subtract the lower-frequency variability, and the results were virtually identical; not shown). During the period in SP/MJO2, there is a composite-average night–day SST variation of  $\sim 1.5^\circ\text{C}$ , with a peak at  $\sim 13$  local time (13L). Night–day variations in air temperature,  $S_0$ ,  $L_v E_0$ , and wind speed are  $\sim 1^\circ\text{C}$ ,  $\sim 10 \text{ W m}^{-2}$ ,  $\sim 80 \text{ W m}^{-2}$ , and  $\sim 2 \text{ m s}^{-1}$ , respectively (Fig. 2.11b). The diurnal cycle in air temperature suggests that the boundary layer is progressively warmed by increasing SST, which is tied to a progressive increase in wind speed as the mixed layer deepens (Johnson et al. 2001). The sudden air temperature drop of  $\sim 0.6^\circ\text{C}$  around 14L indicates the effect of evaporatively generated cold pools, which in turn provides a strong, albeit brief, boost to air-sea fluxes (Fig. 2.11b). Note, however, that the magnitude of this sudden cooling owes largely to a single event on 15 Nov (Fig. 2.10). The composite evolution of SST and fluxes is qualitatively similar during the Oct period, though with more

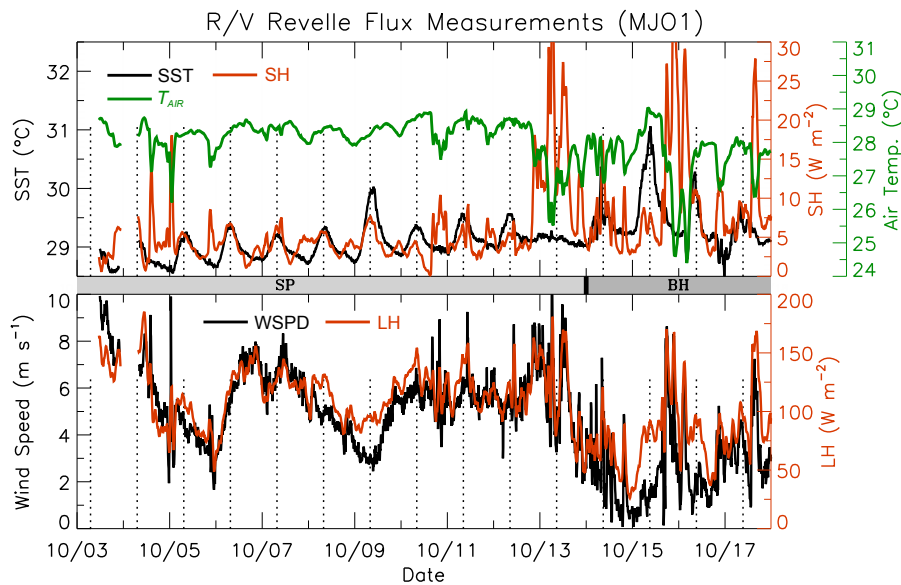


Fig. 2.9. (top) Time series spanning convective onset for MJO1 of SST (black;  $^\circ\text{C}$ ; left axis), 10-m air temperature (green;  $^\circ\text{C}$ ; outer-right axis), and surface sensible heat flux SH (red;  $\text{W m}^{-2}$ ; inner-right axis) from the *Revelle* (red;  $\text{W m}^{-2}$ ; right axis). (bottom) As in the top except with wind speed (black;  $\text{m s}^{-1}$ ; left axis) and surface latent heat flux LH (red;  $\text{W m}^{-2}$ ; right axis). SH and LH have been smoothed using a one-hour running mean. The vertical dotted lines indicate local noon.

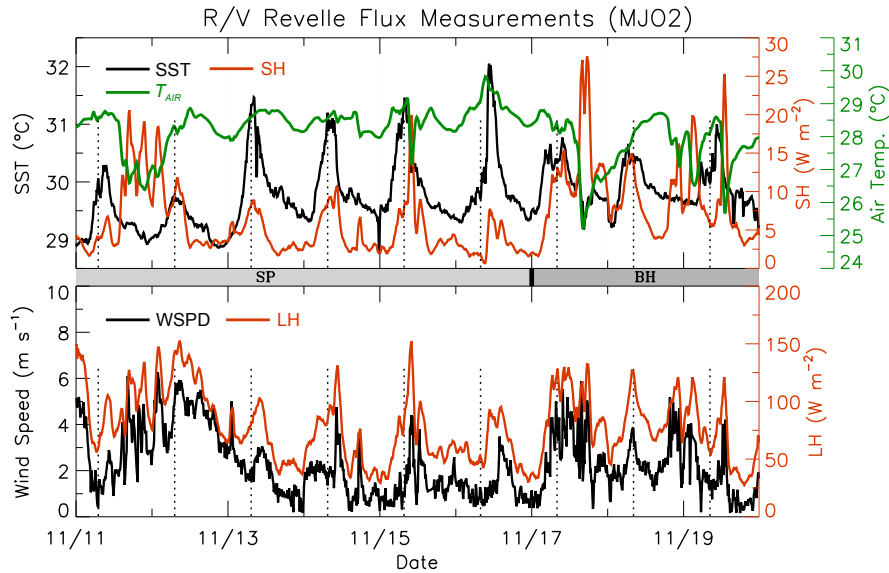


Fig. 2.10. As in Fig. 2.9 except for MJO2.

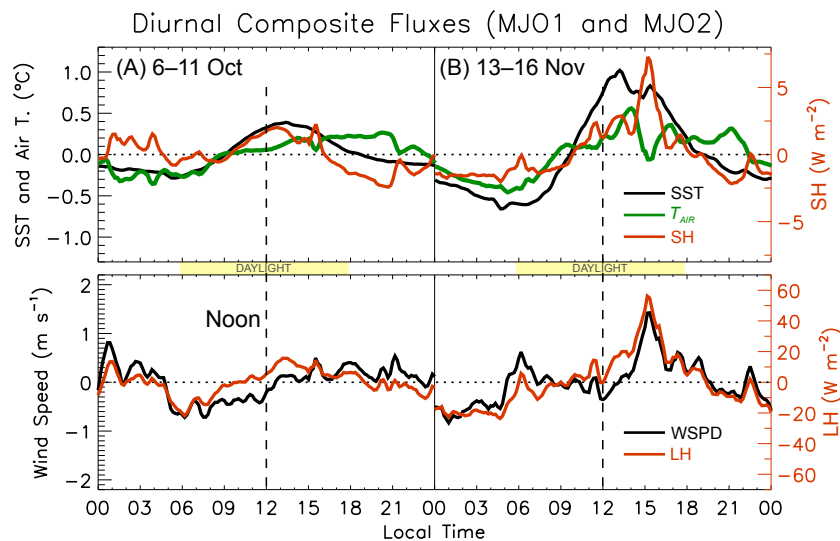


Fig. 2.11. (top) Diurnal composite SST (black;  $^{\circ}C$ ; left axis), 10-m air temperature (green;  $^{\circ}C$ ; left axis), and SH (red;  $W m^{-2}$ ; right axis) for the (a) Oct (MJO1) and (b) Nov (MJO2) suppressed phases. Composite means have been removed. (bottom) As in the top except with wind speed (black;  $m s^{-1}$ ; left axis) and surface latent heat flux LH (red;  $W m^{-2}$ ; right axis). Composite date ranges are (a) 6–11 Oct and (b) 13–16 Nov (end-dates are inclusive). Local time is indicated along the abscissa. Vertical dashed lines indicate local noon. All fields have been smoothed using a 30-min running mean. Yellow boxes indicate solar daylight hours, here and henceforth.

limited diurnal variations, likely owing to larger mean wind speed (Figs. 2.8 and 2.11a). The large-scale cloud response to the diurnal variation in air-sea fluxes, during *both* SP/MJO1 and SP/MJO2, however, was substantial (shown later).

To assess the character of clouds in the DYNAMO array during the MJO suppressed phases, sets of true-color images from the MODIS Aqua and Terra satellites are provided (500-m resolution), with samples for SP/MJO1 (Fig. 2.12) and SP/MJO2 (Fig. 2.13). The Aqua and Terra satellite overpass sequence provides closely overlapping regional sampling each day, though with a three-hour gap between each satellite’s overpass, thereby sampling the evolution of the cloud scene (from the late morning to the early afternoon). Since the overpasses shift each day, however, the sampling regions also shift. The images shown have been cropped from their originals with preference for regions nearest to the northern sounding array and away from image edges where the cloud scene is distorted. The most prominent feature of these cloud scenes is the high degree of mesoscale organization – virtually all clouds are part of either cloud streets (Figs. 2.12b,c, and 2.13h), indicative of horizontal convective rolls (HCRs; Weckwerth et al. 1996), or open cells (Figs. 2.12c–f and 2.13a,b, and d–f). The open cells range in diameter from roughly 15–50 km. Open-cellular cloud organization was also noted in COARE (Johnson et al. 2001). While this organization fundamentally owes to heating from below by the warm ocean surface (i.e., Rayleigh–Bénard convection), the dimensionality of the organization relates to the dominance of shear- versus buoyancy-driven turbulence.

The mode of this organization can be estimated from the ratio  $z_i/L$ , where  $z_i$  is the depth of convective overturning, and  $L$  the Obukhov length, given by

$$L = -\frac{c_p \rho \theta_v u_*^3}{kgF_v}, \quad (2.6)$$

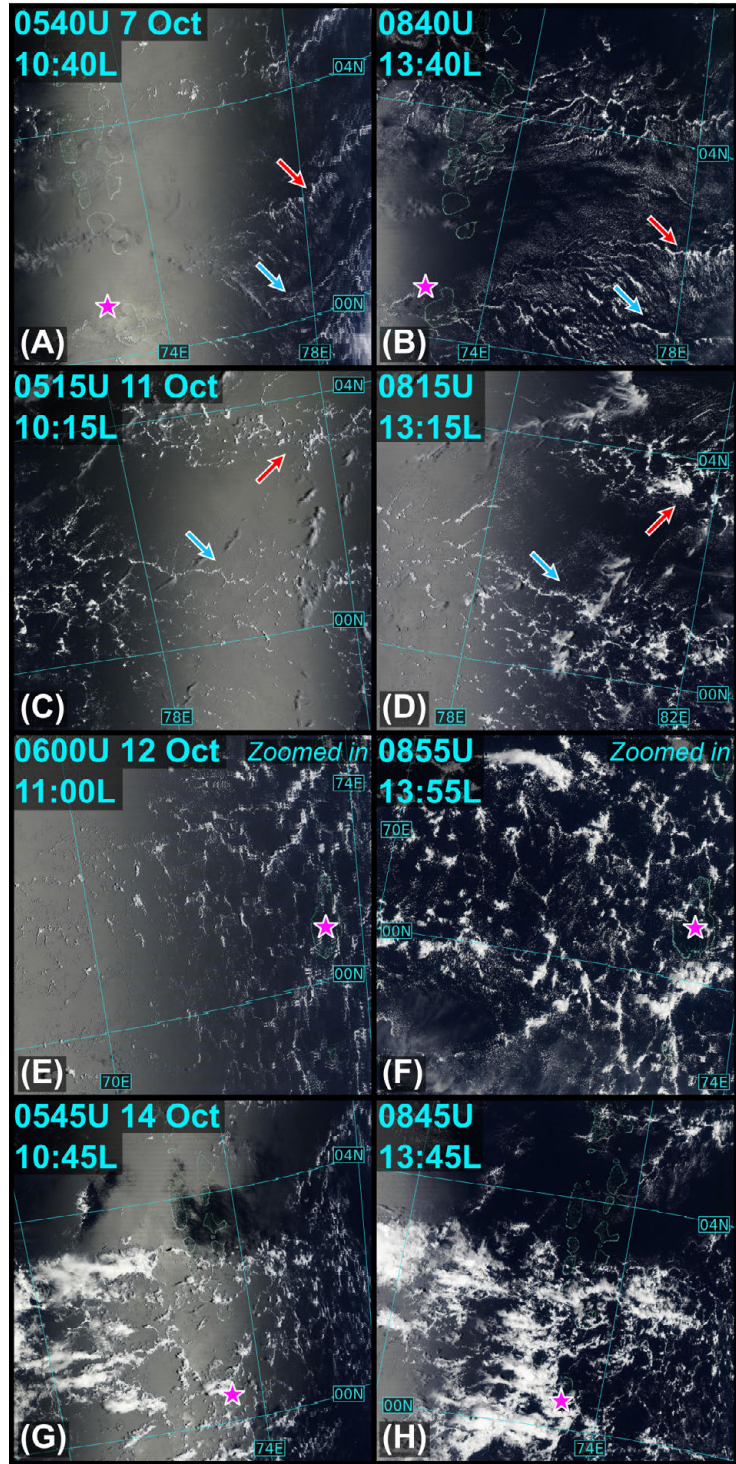


Fig. 2.12. Cropped true-color images from the Terra (left) and Aqua (right) MODIS satellites for selected dates of the Oct suppressed phase (MJO1). Date is indicated in the left column, and UTC and local time are indicated in each panel. The magenta star marks Huvadhu Atoll, located ~100 km north of Addu Atoll. Red and blue arrows indicate subjectively identified corresponding cloud features between same-day images.

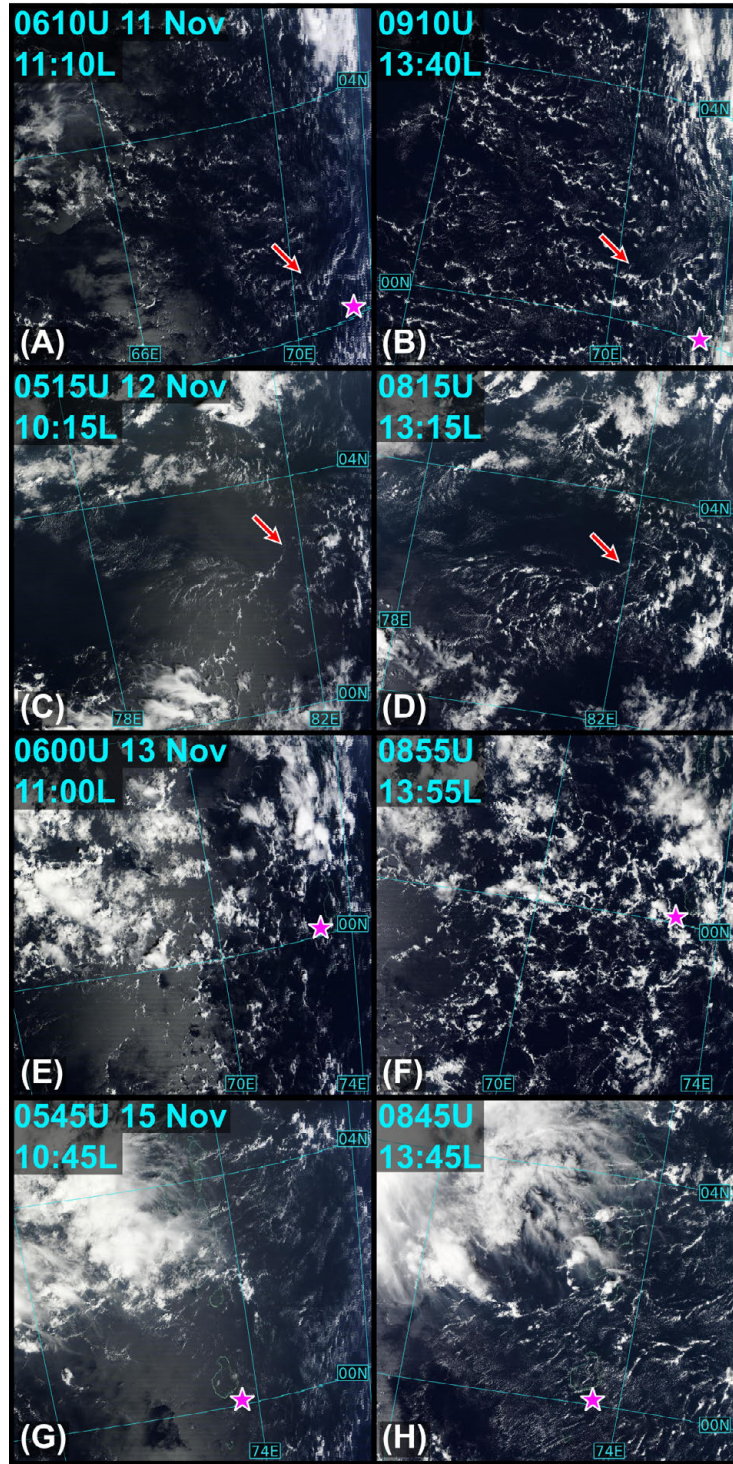


Fig. 2.13. As in Fig. 2.12 except for the Nov suppressed phase (MJO2).

where  $\rho$  is density,  $\theta_v$  virtual potential temperature,  $u_* = \sqrt{\tau/\rho}$  friction velocity,  $k$  the von Kármán constant,  $F_v = S_0 + 0.61c_pTE_0$  buoyancy flux, and  $\tau$  shear stress at the surface. Weckwerth et al. (1999) suggest that HCRs are favored when  $-z_i/L < 25$ , i.e., when low-level wind shear is relatively strong ( $L$  relatively large), while cells are favored for larger ratio values, such as for relatively large surface buoyancy flux or weak wind speeds. Calculating  $L$  from (2.6) using *Revelle* flux site measurements, and taking  $z_i$  as mixed layer depth analyzed subjectively (Johnson et al. 2001) from *Revelle* soundings, reveals mean ratio values of  $\sim 5$  for the Oct suppressed period and  $\sim 130$  for the Nov period. Therefore, conditions generally favor HCRs in the Oct period and open cells in the Nov period, owing to stronger low-level winds in SP/MJO1, both from the perspective of the *Revelle* (Fig. 8) and the greater sounding array (Johnson and Ciesielski 2013; their Fig. 12). While the role of evaporatively generated cold pools in the observed organization is yet unclear, it is likely that some of the cellular structures depicted in Figs. 2.12 and 2.13 owe to outward-spreading cold pools, particularly late in the suppressed phases as rainfall increases leading up to MJO onset (Figs. 2.2, 2.6, and 2.9–2.11) (Rowe and Houze 2014). Detailed observations of the boundary layer thermodynamics will be necessary to pin this down.

Weckwerth et al. (1996) show that the boundary layer circulation related to such mesoscale organization augments the convective instability in the boundary layer by creating localized areas of enhanced moisture, thereby promoting deeper convective clouds than would otherwise occur. Therefore, the cloud organization depicted in Figs. 2.12 and 2.13 may reflect a process by which mesoscale circulation enhances the overall communication of moisture between the boundary layer and overlying free troposphere.

Also apparent during both suppressed periods is a slight change in the cloud scenes within the three hours between satellite overpasses each day. Specifically, an increase in the size and/or number of clouds by afternoon suggests that moist convection is intensifying. This change is particularly clear on 11, 12, and 14 Oct (Figs. 2.12c–h), and 11, 13, and 15 Nov (Figs. 2.13a,b, and e–h) (note however, that expanding cirrus cloud shields also influence the scenes, e.g., Figs. 2.12g,h and 2.13g,h). Diurnal composites of echo-top frequency and echo area coverage calculated from the S-PolKa RHI dataset (cf. section 2) are shown for segments of the suppressed phase in MJO1 (7–13 Oct) and MJO2 (13–16 Nov) in Fig. 2.14 (date ranges selected to avoid variability unrelated to the diurnal cycle; cf. Fig. 2.6). During both suppressed periods, echo-top frequency generally peaks in the lower troposphere, reflecting the dominance of shallow cumuli, with echo area coverage ranging from 0~25%. An increase in low-level echo-top frequency occurs, however, as echo area coverage begins to increase around 11L during the Oct period (Fig. 2.14a), and ~09L in the Nov period (Fig. 2.14b), followed by a pronounced deepening of echo tops thereafter. Frequency >0.5% reaches 9~11 km as echo area peaks around 20% by 15L in both periods, indicating a midafternoon population of congestus clouds with larger cloud size and/or quantity than earlier in the day. Bellenger et al. (2010) relate this afternoon convective invigoration to a reduction of convective inhibition, which is in turn driven by the boundary layer warming driven by increased SST. The deeper clouds persist through evening in the Oct period, dissipating around 02L. During the Nov period, however, deep overnight convective clouds appear more distinctly from afternoon convection, in both echo-top frequency and echo area coverage, around 00~05L. This diurnal cycle in clouds occurs on a large scale, as inferred from the morning–afternoon changes in the MODIS cloud scenes described above (Figs. 2.12 and 2.13).

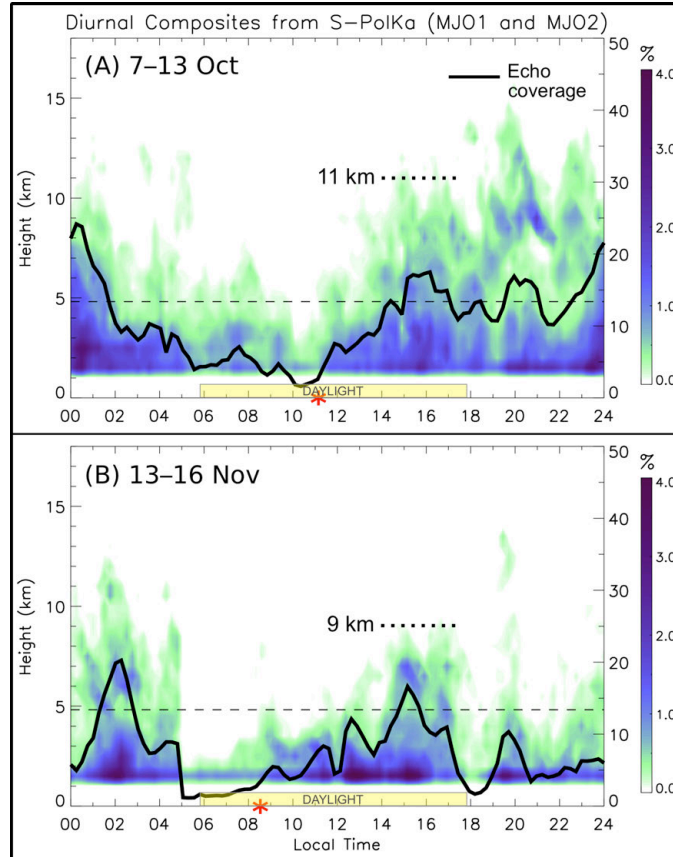


Fig. 2.14. Diurnal time–height composites of convective echo-top frequency (shading; %) and echo area coverage (solid, black line; %; right axis) for the (a) Oct and (b) Nov suppressed phases, calculated from 15-min S-PolKa RHI data. Composite date ranges are (a) 7–13 Oct and (b) 13–16 Nov (end-dates are inclusive). Local time is indicated along the abscissa. Red asterisks mark the time of increasing echo-top frequency and echo area coverage. The 11- and 9-km levels are indicated by dotted lines. Horizontal dashed lines indicate the 0°C level.

Diurnal composites of TRMM rainfall averaged over the northern sounding array for periods in MJO1 (7–13 Oct) and MJO2 (11–16 Nov) are provided in Fig. 2.15. While the mean amounts are very small, both periods exhibit increasing rainfall in the afternoon in connection with building convection (Fig. 2.14). Afternoon rainfall peaks around 17–21L, roughly around the time of greatest and deepest cloud echo-top frequency, a relationship that holds on the much longer time scale of the MJO (Xu and Rutledge 2014). While rainfall in the Oct period largely persists through night before tapering off in the morning (Fig. 2.15a), rainfall in the Nov period

exhibits a more distinct early-morning maximum offset by  $\sim 12$  h from the afternoon peak (Fig. 2.15b). This maximum in the Nov period is consistent with the distinct early-morning maximum in echo-top frequency and echo coverage (Fig. 2.14), though the timing is in slight disagreement. Differences in timing between Figs. 2.14 and 2.15 may relate to differences in spatial sampling between S-PolKa and the TRMM northern-array average (also recall the difference in sampling frequency). The existence of both afternoon and nocturnal rainfall peaks was also found in suppressed periods during COARE and MISMO (Sui et al. 1997; Johnson et al. 2001; Bellenger et al. 2010).

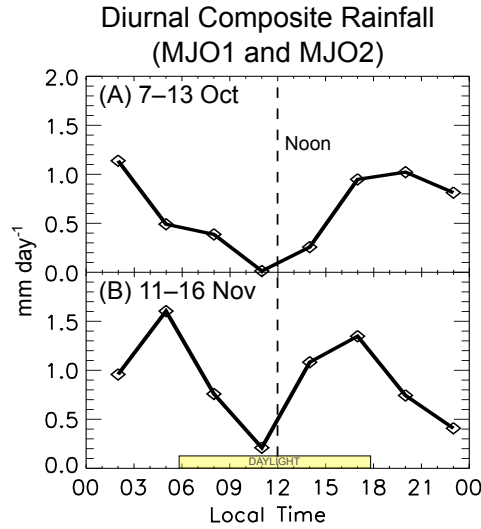


Fig. 2.15. Diurnal composites of TRMM 3B42 rainfall ( $\text{mm day}^{-1}$ ) averaged over the northern sounding quadrilateral for the (a) Oct and (b) Nov suppressed phases. Composite date ranges are (a) 7–13 Oct and (b) 11–16 Nov (end-dates are inclusive). Local time is indicated along the abscissa.

Figure 2.16 provides diurnal composite  $q$ ,  $\omega$ ,  $Q_1$ , and  $Q_2$  derived from the DYNAMO gridded analysis for the suppressed phases in MJO1 (7–13 Oct) and MJO2 (11–16 Nov). Mixing ratio  $q$  is shown with the composite mean removed ( $q'$ ), though the means are retained in all of the other fields. There is remarkable consistency in the diurnal cycle between the Oct and Nov suppressed phases, despite a relatively weaker diurnal cycle in fluxes during SP/MJO1, as

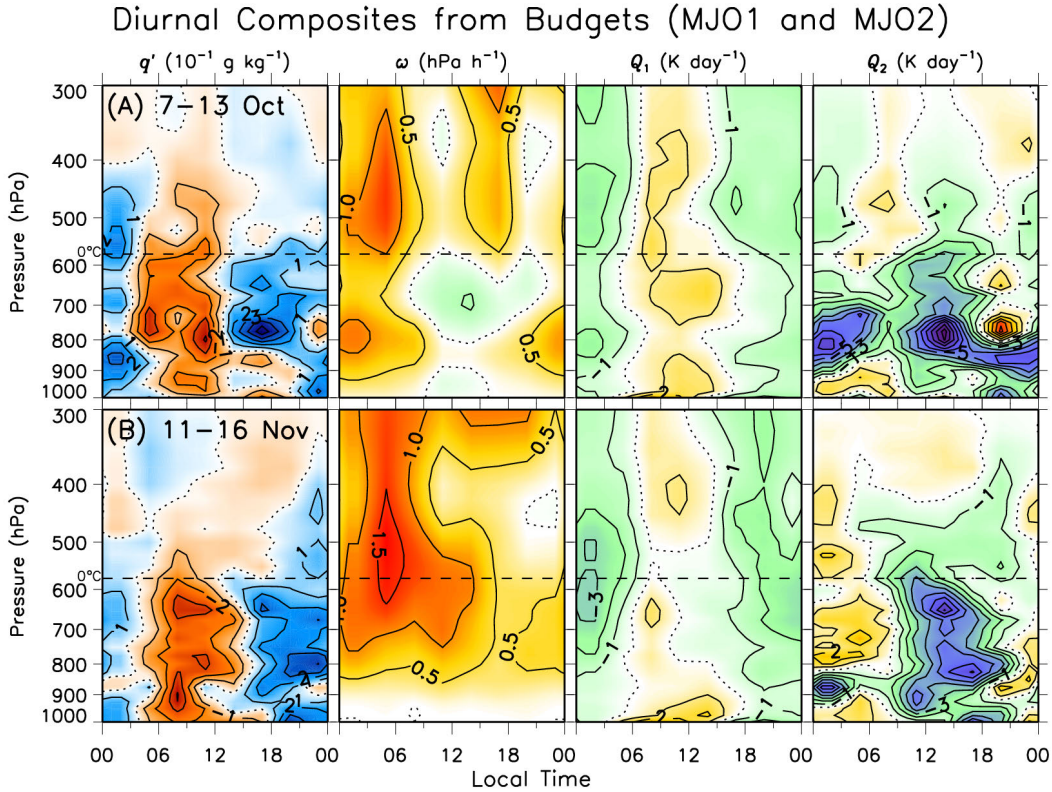


Fig. 2.16. Diurnal composite variables from the northern-array gridded analysis for the suppressed phases of (a) MJO1 and (b) MJO1, showing (from left–right) water vapor mixing ratio with composite mean removed  $q'$  (contoured every  $10^{-1} \text{ g kg}^{-1}$ ),  $\omega$  (every  $0.5 \text{ hPa h}^{-1}$ ),  $Q_1$ , and  $Q_2$  (every  $\text{K day}^{-1}$ ). Positive values are shaded in red, except for  $q'$ , which is the opposite. Composite date ranges are (a) 7–13 Oct and (b) 11–16 Nov (end-dates are inclusive). Horizontal dashed lines indicate the  $0^\circ\text{C}$  level. Vertical smoothing has been applied to all fields using a three-point running mean.

measured at the *Revelle* (Figs. 2.9–2.11). Both periods exhibit a morning–evening  $q'$  swing of magnitude  $0.4\sim 0.6 \text{ g kg}^{-1}$  in the layer  $900\sim 550 \text{ hPa}$ , with moister conditions in the evening. Since temperature varies negligibly (not shown), this diurnal variation in  $q'$  directly correlates with relative humidity, which exhibits anomalies of  $\text{O}(3\%)$ . Most of the variation in  $q'$  occurs below the  $0^\circ\text{C}$  level, reflecting the dominance of warm-rain clouds (Figs. 2.6 and 2.14). Anomalies of  $q'$  do appear above the  $0^\circ\text{C}$  level overnight, however, indicative of deeper clouds (Fig. 2.14). The diurnal variation in  $\omega$  indicates enhanced deep subsidence in the late evening–early morning, which may relate to the remote forcing of nocturnally invigorated deep

convection in the ITCZ or elsewhere, though this issue remains unsolved. The weak rising motion (SP/MJO1; Fig. 2.16a) or relaxed subsidence (SP/MJO2; Fig. 2.16b) in the lower troposphere in the morning–afternoon likely owes to the local increase in convective activity. The evolution of  $Q_1$  largely reflects the diurnal cycle of radiative heating, though enhanced warming near and within the boundary layer relates to the large convergence of eddy heat flux due to surface warming as the mixed layer deepens (Johnson et al. 2001).

The diurnal cycle in  $Q_2$  indicates pronounced daytime apparent moistening, the majority of it taking place from 09~18L, which is in quadrature with  $q'$ , indicating the dominance of the local tendency term in (2) (this was verified by a check of the individual contributions to  $Q_2$ ; not shown). Since  $Q_2 < 0$  through most of the column, and precipitation is negligible (Fig. 2.2), this signal can be related back to the vertical convergence of vertical eddy moisture flux, which ties to surface evaporation (eqns. 2 and 4). This conclusion also follows by noting the magnitude difference between  $Q_1$  and  $Q_2$ : if water phase changes dominated the moisture source,  $Q_1$  and  $Q_2$  would exhibit similar magnitude (such as when stratiform rainfall abounds as in the active phase; Fig. 2.3). Therefore, while latent heat release in the cloud layer is critical for driving convective eddies upwards into the free troposphere, it is the large vertical eddy moisture flux by clouds that is driving this moistening.  $Q_2$  moistening reaches a peak of  $\sim 10 \text{ K day}^{-1}$  ( $\sim 4 \text{ g kg}^{-1} \text{ day}^{-1}$ ) at 14L around 800 hPa in the Oct period, which closely coincides with the time of peak  $L_v E_0$  as measured at the *Revelle* (Fig. 2.11; recall the difference in temporal resolution between these two datasets). While  $Q_2$  moistening persists within a shallow layer through much of the evening in SP/MJO1,  $Q_2$  switches to drying overnight–early morning during SP/MJO2. A cycle in  $q'$  and  $Q_2$  also appears in the boundary layer (i.e., below  $\sim 900 \text{ hPa}$ ), which is shifted slightly later than

the cycle in the free troposphere. While this boundary layer moistening is not yet understood, it has been observed in previous field campaigns (Sui et al. 1997; Yasunaga et al. 2008).

An issue that remains unresolved is the role of water vapor storage in clouds: since the volume of clouds exhibits substantial diurnal fluctuation (Fig. 2.14), the amount of water contained in suspended hydrometeors likely also fluctuates (McNab and Betts 1978). This issue will be the subject of a future study. Another present hurdle to closing the moisture budget on the diurnal time scale is that accurate diurnal surface flux information is limited to a single location (e.g., Fig. 2.11), while information over the northern sounding array is necessary to complement the sounding-derived information (Fig. 2.16).

The findings described in this section demonstrate that the locally driven diurnal cycle explains much of the temporal variation in column humidity over the DYNAMO northern sounding array, as demonstrated during the period of low–midlevel moistening in the suppressed phase or pre-onset stage of the MJO (Fig. 2.7). This diurnal cycle is characterized by a daytime deepening of clouds from shallow cumulus to congestus, an increase in their areal coverage, and a corresponding peak in cumulus moistening (Figs. 2.7 and 2.12–2.16). The afternoon invigoration of convection is driven by the afternoon peak in SST and air-sea fluxes, which owes to the influence of oceanic diurnal warm layers (Figs. 2.8–2.11) (Bellenger et al. 2010; Matthews et al. 2014).

A noteworthy finding described in this section is the prominence of mesoscale cloud organization during the suppressed phase (also observed in COARE; Fig. 8 of Johnson et al. 2001), which is manifest in HCRs and/or open cells, depending primarily on the strength of the low-level wind (Figs. 2.12 and 2.13). This cloud organization is indicative of buoyancy-driven boundary layer overturning circulation, which is likely important for augmenting the overall

communication of moisture between the boundary layer and the overlying free troposphere (Weckwerth et al. 1996).

### *2.5 Summary and conclusions*

Two MJO events were comprehensively sampled in the tropical Indian Ocean during DYNAMO, providing an unprecedented opportunity to diagnose the key processes in the transition from shallow to deep moist convection during MJO convective onset from in situ measurements. Atmospheric soundings, radar, and air-sea flux measurements collected during DYNAMO have been employed to carry out this diagnosis.

The findings of section 2.3—a large-scale overview of two DYNAMO MJO events—demonstrate that humidification of the low–midtroposphere during the late suppressed phase or pre-onset stage of the MJO owed to simultaneous changes in the convective cloud population and large-scale circulation, as schematically depicted in Fig. 2.17a [note: the clouds depicted in Fig. 2.17 represent the predominant character of the convective cloud population; all convective cloud modes, however, can occur within a given MJO phase (Mapes et al. 2006; Barnes and Houze 2013)]. While there were differences between the pre-onset stage of MJO1 and that of MJO2 (i.e., the character and duration of moistening and depth of the moist layer; Fig. 2.2), the role of large-scale circulation is similar in both. Namely, the drying by large-scale circulation wanes as the low–midtroposphere humidifies and the convective cloud population is invigorated (Fig. 2.17a). Rainfall begins and increases as the column is moistened and convective clouds deepen. Following MJO onset (i.e., the onset of large-scale diabatic heating; Fig. 2.3), humidity is increased over the full depth of the column in connection with relatively bottom-heavy convection, indicative of predominant congestus and cumulonimbus clouds and minimal

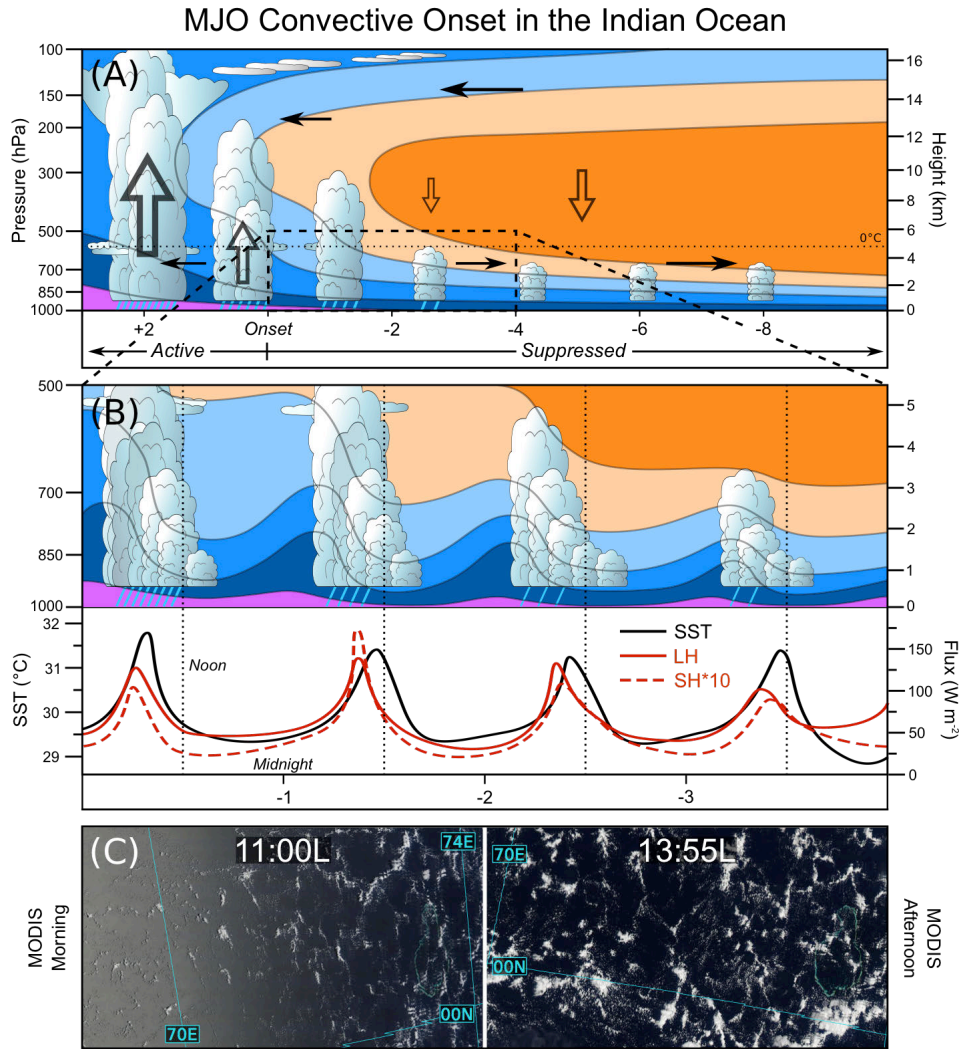


Fig. 2.17. A schematic model of MJO convective onset (in an Eulerian framework) based on the findings of this study. (a) Time–pressure series of convective clouds (i.e., the predominant character of convective clouds) and relative humidity RH (shading; ranging from 40~80%; brown is drier), from the suppressed phase, through MJO onset, to the early-active phase, as indicated along the abscissa. Shown is a transition from shallow cumulus to congestus to deep cumulonimbus and stratiform clouds, with high cirrus clouds appearing prior to onset. The blue lines beneath clouds indicate rainfall. Open (closed) arrows schematically depict vertical (horizontal) motion, with size proportional to magnitude. (b) (top) Time–pressure series emphasizing diurnal variability during the late-suppressed phase or pre-onset stage [time–pressure space denoted by the dashed box in (a)], with RH, convective clouds, and rainfall; and (bottom) the corresponding time series of SST (black), latent heat flux LH (red, solid), and sensible heat flux SH multiplied by 10 (red, dashed). Abscissa ticks are local midnight, and vertical dotted lines are local noon. (c) Characteristic cloud field as depicted by MODIS true-color imagery in the (left) morning (0600 UTC, 11:00L) and (right) afternoon (0855 UTC, 13:55L) (from 12 Oct 2011; Figs. 2.12e,f), revealing the prominence of mesoscale cloud organization (i.e., open cells and horizontal convective rolls).

stratiform rainfall. The heating profile becomes progressively more top-heavy as peak ascending motion shifts upward later in the active phase, indicating increasing stratiform rainfall. This evolution is generally consistent with the findings of previous studies (Maloney and Hartmann 1998; Johnson et al. 1999; Benedict and Randall 2007; Riley et al. 2011; Del Genio et al. 2012; Barnes and Houze 2013; Powell and Houze 2013; Zuluaga and Houze 2013; Kerns and Chen 2014; Rowe and Houze 2014; Xu and Rutledge 2014).

The moisture budget indicates the importance of both vertical and horizontal advection in the moistening of the low–midtroposphere prior to and during MJO convective onset, namely, via relaxation of the drying due to subsidence and horizontal advection. The role of horizontal advection in DYNAMO is largely manifest in a waxing and waning of horizontal-advective drying, which relates to the enhancement (abatement) of low-level westerly flow (Fig. 2.17a) and equatorial Rossby gyres during the active phase (pre-onset stage) (Gottschalck et al. 2013; Kerns and Chen 2014). The abatement of subsidence drying during the pre-onset stage is partly linked to the approach of the global-circumnavigating (gravity or Kelvin wave) MJO signal, which drives a relaxation of upper-level convergence (Kiladis et al. 2001; Gottschalck et al. 2013; Johnson and Ciesielski 2013). The appearance of high cirrus clouds prior to MJO onset is also linked to the near-tropopause adiabatic cooling and moistening driven by this circumnavigating signal (Fig. 2.17a) (Virts and Wallace 2010; Virts et al. 2010; Riley et al. 2011; Del Genio et al. 2012).

Local factors may also be important for the observed waning of subsidence. In particular, column radiative cooling is observed to decrease during the pre-onset stage (Sobel et al. 2014; Johnson et al. 2015), which coincides with the invigoration of convective clouds and development of high cirrus clouds. Reduced column radiative cooling must in turn cause

relaxation of the large-scale subsidence, when assuming negligible temperature variations (Mapes 2001). While such a feedback between moist convective clouds, column radiative heating, and large-scale subsidence is cited as a *maintenance* mechanism for the MJO active phase in the context of moisture-mode theory (Chikira 2014), it is possible that this feedback also plays a role in the transition from shallow to deep convection during MJO onset/initiation.

DYNAMO observations have also been exploited to describe the diurnal cycle of moist convection during the suppressed phase or pre-onset stage of the two MJO events (section 2.4), with the aim of improving our understanding of the physical processes involved in convective invigoration, and ultimately, shedding light on convective invigoration in relation to MJO onset. A new finding of this study is the importance of the locally driven diurnal cycle during the pre-onset stage of the MJO. Namely, the diurnal cycle of convective clouds dominates temporal variations of column humidity during the pre-onset stage (Fig. 2.7). This diurnal cycle is characterized by a daytime deepening of shallow cumuli (and an increase in their areal coverage; Fig. 2.14), which develop into congestus clouds by afternoon. This diurnal cycle is schematically depicted in Fig. 2.17b (upper panel), which occurs within the slower (i.e., daily-mean) evolution associated with the transition into the MJO active phase (Fig. 2.17a). This daily convective invigoration drives a prominent daytime maximum in cumulus moistening (Fig. 2.16), which roughly coincides with a peak in SST and air-sea fluxes, the fluxes lagging the SST maxima by approximately 2 h (Fig. 2.17b, lower panel). The diurnal cycle in SST relates to oceanic diurnal warm layers that form under light-wind, clear-sky conditions (Halpern and Reed 1976; Matthews et al. 2014). This daytime surface warming drives an increase in surface fluxes, which invigorates moist convection by reducing convective inhibition (Fig. 2.11; Bellenger et al. 2010). Figure 2.17b schematically depicts this ocean-driven diurnal moistening and diurnal

cloud response within an environment that is transitioning from suppressed to active conditions in connection with MJO onset, i.e., as the drying by large-scale subsidence and horizontal advection wanes and convective clouds deepen in the daily-mean sense (Fig. 2.17a).

A further finding of this study is the prominence of mesoscale cloud organization during the suppressed phase, which is manifest in open cells and horizontal convective rolls (Fig. 2.17c). The character of this organization relates to the relative magnitudes of shear-driven and buoyancy-driven turbulence, though it fundamentally owes to heating from below by the warm ocean surface. This mesoscale organization may play a role in the moistening process by driving convective elements to greater heights than would otherwise occur through the local enhancement of convergence and deepening of boundary layer moisture along cell boundaries (Weckwerth et al. 1996). More work is needed to investigate this process and ascertain the relative role of cold pools in the organization.

The primary findings of this study lead to two new testable hypotheses pertaining to the transition from the suppressed to the active phase of the MJO:

1. *The diurnal cycle of sea surface temperature and air-sea fluxes drives a net boost to convective activity and cumulus moistening in the low-midtroposphere, which would not exist without such a diurnal cycle.*

That is to say, the daytime invigoration of moist convection related to the diurnal cycle of SST yields more vigorous cumulus convection in a daily-mean sense than if this diurnal cycle did not exist. If this hypothesis were true, then the diurnal cycle of SST, as described herein, may be regarded as a forcing mechanism for convective invigoration and column moistening.

2. *The mesoscale organization of clouds and the associated mesoscale circulation lead to localized areas of enhanced boundary layer moisture and deeper mixed layers*

*(Weckwerth et al. 1996; Johnson et al. 2001), leading to deeper clouds than would otherwise occur.*

This hypothesis is analogous to the former in that it brings to light the possible role of local processes (i.e., mesoscale cloud organization) in augmenting cumulus moistening of the low–midtroposphere, and hence, assisting the transition from shallow to deeper convective clouds during MJO convective onset. Proper testing of these hypotheses using models will require, at a minimum, simultaneous resolution of both the cumulus scale, of  $O(\leq 500 \text{ m})$ , and the mesoscale cloud organization, of  $O(>10 \text{ km})$  (Figs. 2.12 and 2.13).

CHAPTER 3  
ON THE DRIVING MECHANISMS OF THE DIURNAL CYCLE OF  
MOIST CONVECTION AND FEEDBACKS ONTO CLIMATE

*3.1 Introduction*

Following from the observational results presented in chapter two, this chapter describes a suite of convection-resolving model experiments designed specifically to test the possible role of the diurnal cycle in MJO initiation, and in large-scale climate in general. Specifically, the experiments assess whether the diurnal cycle of moist convection drives a net column moisture source that would not otherwise exist. Additionally, the modified-physics tests will enable diagnosis of the relative roles of SST and radiative heating in the diurnal cycle of moist convection. Although these simulations exhibit mesoscale cloud organization, testing of the importance of this organization to the climate is left for future work.

Since the primary motivation for this study is to assess the character and role of the diurnal cycle of moist convection in large-scale climate, a crucial element of the model experiments (which are described in section 3.3) is the treatment of large-scale circulation. Since the model experiments are integrated at high spatial resolution in order to resolve moist-convective circulations, the simulation domains employed are of  $O(10^2)$  km; and therefore, large-scale circulation – i.e., of  $O(10^3-10^4)$  km in nature – cannot be resolved. The effects large-scale circulation are therefore parameterized by diagnosing “large-scale” vertical motion via an approximation deriving from weak temperature gradient (WTG) theory (Sobel et al. 2001). This diagnostic vertical motion operates in response to model diabatic heating, providing the necessary adiabatic warming and/or cooling to offset this heating diabatic heating. Since this

large-scale vertical motion also advects moisture, it represents the important feedback between the diabatic heating and column humidity, as exists in nature.

Background on WTG theory and its use in large-scale forcing in models is provided in section 3.2, followed in section 3.3 by the specific modeling tools and methodology for the model experiments in this study. The results of the model experiments are provided in section 3.4, with a summary of the associated findings in section 3.5.

### 3.2 Weak temperature gradient forcing

WTG theory rests on the notion that horizontal temperature gradients in the tropics are weak owing to the negligible Coriolis torque on horizontal flow (Charney 1963; Sobel and Bretherton 2000; Sobel et al. 2001), and the resulting efficiency with which gravity waves disperse localized temperature (i.e., buoyancy) anomalies over the greater area. As a result, temperature holds in a state of approximate balance, such that the temperature budget reduces to

$$\bar{w} \frac{d\bar{\theta}}{dz} \approx Q_1. \quad (3.1)$$

In (3.1),  $w$  is vertical motion in  $z$ -coordinates,  $\theta$  is potential temperature, overbars denote the regional (i.e., simulation-domain) average in  $(x,y)$ , and  $Q_1$  is the diabatic heat source, i.e., (2.1).

The strict WTG constraint on vertical velocity (e.g., Sobel and Bretherton 2000) can be found through a simple rearrangement of (3.1):

$$\bar{w} = w_{wtg} \equiv Q_1 \left( \frac{d\bar{\theta}}{dz} \right)^{-1}. \quad (3.2)$$

With  $w_{wtg}$  diagnosed from the RHS of (3.2), the advection of  $\theta$  by  $w_{wtg}$  will perfectly offset of the heating due to  $Q_1$ , resulting in constant  $\bar{\theta}$ . Imposing (3.2) directly is unphysical, however, since the WTG balance encompassed by (3.1) represents the aggregate effect of the diabatically-

generated gravity waves, or “buoyancy bores” (Mapes 1993), that disperse localized buoyancy perturbations. Gravity waves do not operate instantaneously – they make adjustments over a certain timescale as a function of their phase speed, which varies as a function of their vertical scale (Nicholls et al. 1991).

The relaxed, spectral WTG scheme of Herman and Raymond (2014) parameterizes the vertical scale-dependence of gravity wave propagation. Consider first the general formulation of relaxed  $w_{wtg}$  (Raymond and Zeng 2005):

$$w_{wtg} \equiv \frac{\theta'(z,t)}{\tau} \left( \frac{d\bar{\theta}}{dz} \right)^{-1} = D_{\theta}(z,t)/\tau. \quad (3.3)$$

Compared to (3.2),  $Q_1$  is replaced by  $\theta'(z,t)/\tau$ , where  $\theta'(z,t)$  is the horizontally averaged potential temperature deviation at time  $t$  relative to a reference (i.e., base-state) profile – namely,  $\bar{\theta}(z,t) - \theta_0(z)$  – and  $\tau$  is a relaxation time scale. A single relaxation timescale cannot account for all vertical gravity wave modes, however. Following Herman and Raymond (2014), the spectral coefficients of the diabatic forcing  $D_{\theta}$  in (3.3) can be diagnosed from

$$\Theta_j(t) = \frac{2}{h} \int_0^h D_{\theta}(z,t) \sin(m_j z) dz, \quad (3.4)$$

where  $h$  is tropopause height,  $m_j = j\pi/h$  is vertical wavenumber, and  $j = 1, 2, 3, \dots$  represents the hydrostatic gravity wave vertical mode.  $w_{wtg}$  is then recomposed by summing over all vertical modes:

$$w_{wtg}(z,t) = \sum_j \frac{\Theta_j(t)}{\tau_j} \sin(m_j z), \quad (3.5)$$

where

$$\tau_j = L / c_j = L m_j / N = \pi L j / h N \quad (3.6)$$

is the mode-dependent relaxation timescale, derived assuming  $c_j = N/m_j$  the mode-dependent hydrostatic gravity wave phase speed,  $L = 300$  km is the horizontal relaxation scale (Herman and Raymond 2014), and  $N$  is the column mean Brunt-Väisälä frequency. The choice of  $L = 300$  km corresponds to  $\tau \sim 1.7$  h and  $c \sim 50$  m s<sup>-1</sup> for the first internal mode. This system for diagnosing  $w_{wtg}$  is an idealization with the following assumptions: constant  $N$  with depth, zero mean horizontal wind, and a rigid lid at the tropopause.

The spectral  $w_{wtg}$  technique has advantages over the strict WTG forcing, i.e., (3.2), in that the temperature field relaxes toward the reference state rather than opposing diabatic heating instantaneously, thereby permitting small buoyancy perturbations to sustain. This relaxation is also mode dependent. Shallow diabatic forcing, for example, yields a weaker (i.e., slower) response in  $w_{wtg}$  than does a deep heating, via (3.6). The WTG large-scale forcing approach, in general, has advantages over other techniques, such as applying an external profile of vertical motion to force the model thermodynamic fields – e.g., that measured during a field experiment. In such an approach, the vertical motion is decoupled from the internal diabatic forcing, and the heat budget is therefore not constrained, freeing temperature to drift with time. Furthermore, vertical motion is typically a derived quantity from basic field observations rather than directly measured (cf. section 2.2.A), and is difficult to accurately diagnose at the frequency required to adequately resolve the diurnal cycle.

The  $w_{wtg}$  approach for applying large-scale forcing is not without limitation. Given that  $w_{wtg}$  is driven by the simulated diabatic forcing, any errors in the diabatic forcing translate to errors in the  $w_{wtg}$  response. Furthermore,  $w_{wtg}$  is an idealization in that 1) the large-scale forcing is assumed to solely owe to gravity waves, and 2) these gravity waves fully offset the daily-averaged diabatic tendencies. In an alternative approach, for example, the model base state can

be adjusted over time by the internal diabatic heating (Herman and Raymond 2014). Since it is critical that the temperature budget be constrained in the model experiments for the purpose of analyzing feedbacks between the diurnal cycle of moist convection and large-scale circulation, however, this spectral  $w_{wtg}$  technique is quite appropriate.

### *3.3 Modeling techniques and methodology*

#### A) CLOUD-RESOLVING MODEL

The explicit treatment of moist convection is of the utmost importance for the present study, since the objective of this study is to characterize the diurnal cycle of convection and its relationship with radiation and large-scale circulation. The model experiments are carried out with CM1 (Cloud Model 1; Bryan and Fritsch 2002). Specifically designed for cloud modeling, CM1 solves a system of equations for moist processes that is both mass- and energy-conserving (Bryan and Fritsch 2002). CM1 employs the time-split (Klemp and Wilhelmson 1978) third-order Runge–Kutta time integration scheme (Wicker and Skamarock 2002) with a compressible, horizontally explicit, and vertically implicit pressure solver (Klemp et al. 2007; as in the Advanced Research WRF). Model variables are staggered on a C grid, with advection performed using fifth-order differencing in all spatial dimensions, which includes implicit diffusion (no additional diffusion is applied) (Wicker and Skamarock 2002). Turbulence is modeled using a turbulent kinetic energy (TKE) scheme similar to that of Deardorff (1980). Microphysics is parameterized with the two-moment Morrison scheme (Morrison et al. 2005, 2009), which is double-moment in the mixing ratios of rain water  $q_r$ , cloud ice  $q_i$ , snow  $q_s$ , and graupel  $q_g$ . A constant cloud droplet concentration of  $100 \text{ cm}^{-3}$  is assumed, though cloud water mixing ratio  $q_c$  is predicted.

The spectral  $w_{wtg}$  scheme of Herman and Raymond (2014) is implemented in CM1 as in (3.4)–(3.6) (cf. section 3.2). The domain-averaged input terms are first interpolated onto a vertical grid of constant 50-m spacing.  $w_{wtg}$  is then diagnosed and interpolated back onto the stretched model grid. Unmodified,  $w_{wtg}$  exhibits a large, unphysical diurnal cycle in the lower troposphere – particularly the planetary boundary layer (PBL) – where there are large temperature variations and negligible static stability (applying WTG balance at low levels is a known issue; Herman and Raymond 2014). While previous studies have applied a sine function that forces  $w_{wtg}$  toward zero at low levels (Raymond and Zeng 2005), a constant subsidence profile ( $w_{dyn}$ ) derived from an average of the DYNAMO northern-array sounding budget analysis over SP/MJO2 is instead applied at low levels herein (Fig. 3.1).  $w_{wtg}$  is replaced with  $w_{dyn}$  in the lower troposphere according to  $w_{merge} = c_1 \times w_{wtg} + c_2 \times w_{dyn}$ , where  $(c_1, c_2) = (1, 0)$  for  $z \geq z_{top}$ ,  $(c_1, c_2) = (0, 1)$  for  $z \leq z_{bot}$ ,  $c_1 = (z - z_{bot}) / (z_{top} - z_{bot})$  for  $z_{bot} < z < z_{top}$ , and  $c_2 = 1 - c_1$ . With the choices of  $z_{top} = 5$  km and  $z_{bot} = 1$  km,  $w_{merge} = w_{dyn}$  in the PBL. This merged profile – simply denoted  $w_{wtg}$  henceforth – is then used to advect  $\theta$  and water vapor mixing ratio  $q$  using second-order differencing.

The diurnal cycle of moist convection is partly driven by the diurnal cycle of SST and the associated diurnal cycle in surface fluxes, and partly by the diurnal cycle of shortwave radiative heating. SST is prescribed in the model with a repeating diurnal cycle, which is from a diurnal composite of observed SST at R/V *Revelle* during SP/MJO2 (i.e., Fig. 2.10). This diurnal cycle is characterized by a range of 1.9°C from 29.3–31.2°C, with a mean of 29.9°C. The fluxes of heat and moisture are computed by assuming constant exchange coefficients,  $C_h = 1.66 \times 10^{-3}$  and  $C_q = 1.74 \times 10^{-3}$  for heat and moisture, respectively, which are derived from an analysis of R/V *Revelle* flux measurements for SP/MJO2 (cf. Moum et al. 2013). These coefficients are then

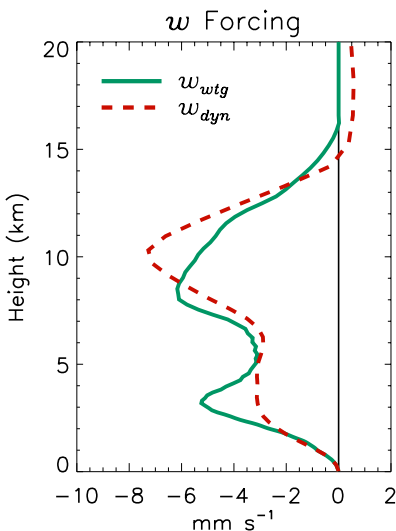


Fig. 3.1. Vertical profiles (km) of vertical motion ( $\text{mm s}^{-1}$ ), including that derived using the spectral WTG scheme  $w_{wtg}$  averaged over two days of simulation time (green solid), and that from the DYNAMO northern-array average over SP–MJO2  $w_{dyn}$  (red dashed). The profile of  $w_{wtg}$  shown is post-merging with  $w_{dyn}$  at low levels.

used along with simulated wind speed and prescribed SST to calculate the fluxes from the bulk formulae. Radiation is modeled using the comprehensive NASA Goddard longwave and shortwave radiation schemes, which include cloud interactions (Chou and Suarez 1994, 1999; Tao et al. 1996). Although this radiation scheme predicts the shortwave radiative fluxes as a function of location, time, and date, the date is held fixed to 13 Nov 2011 to prevent any possible drift in SW. The location for the radiation calculations is set to  $0^\circ, 80^\circ\text{E}$  – the approximate location of the R/V *Revelle* (Fig. 2.1). Surface drag is computed by diagnosing the surface momentum exchange coefficient  $C_d$  as a linear function of wind speed, as in Fig. 2 of Fairall et al. (2003) (with a minimum allowable value of  $C_d = 10^{-3}$ ).

In lieu of prescribing the model state at the lateral boundaries, periodic conditions are imposed. This imposition comes with the assumption that the moist convective processes simulated within the model domain effectively represent that which occurs over a much greater horizontal scale. A free-slip model top is imposed at height  $z = 22$  km. Rayleigh damping is

applied for  $z > 18.5$  km (9 vertical levels). A stretched vertical grid of 125 levels is employed, with spacing of 50 m from 0–2 km (i.e., 40 layers in the lowest 2 km) stretched up to 350 m above 15 km. The horizontal domain is 102.4 km in the zonal dimension ( $x$ ) and 48 km in the meridional dimension ( $y$ ), with spacing of 200 m. While horizontal spacing of 200 m and vertical spacing of  $\sim 50$  m (in the lower troposphere) adequately resolves meso- $\gamma$  circulations, this grid likely sits outside the true inertial subrange of boundary layer thermals as they occur in nature. This is therefore not strictly a large-eddy simulation.

Computations for the total 15.36 million grid points are divided over 32 (24) processors in the  $x$  ( $y$ ) dimension on the National Center for Atmospheric Research (NCAR) Yellowstone (2012) supercomputing system. Time integration is performed with an adaptive time step  $\Delta t$ , which changes to maintain a Courant number near 0.95 (Wicker and Skamarock 2002), typically yielding  $\Delta t \sim 5$  s. Random perturbations of  $\leq 0.1$  K are placed in  $\theta$  throughout the model domain at initialization to break symmetry.

While CM1 is known to provide adequate results in the simulation of moist convection, there have been many stages of bug repairs since its creation (Bryan and Fritsch 2002; Bryan et al. 2003). The version of the model employed herein is the current version – release 17 (<http://www2.mmm.ucar.edu/people/bryan/cm1/>). Model users and the model creator are aware of a very slight mass drift in the current release of the model (and previous releases), which often manifests in a slight decrease in model pressure with time (e.g., a decrease 4 hPa at the surface over  $\sim 30$  days) (G. Bryan 2015, personal communication). In preliminary simulations for the present application, however, this drift is highly amplified, with remarkable pressure *increases*, in fact, on the order of several hPa day<sup>-1</sup>. This bug long went unnoticed (or untended to) since it is negligible for most applications; however, the present application of CM1 is evidently unique,

wherein external moisture and temperature sources are imposed via  $w_{wtg}$ . Fortunately, this bug is now rectified, leading to an order-of-magnitude less mass drift.

## B) MODEL BASE STATE AND EXTERNAL FORCING

The model base state is homogeneously prescribed (prior to the application of random  $\theta$  perturbations) using an idealized sounding based on the mean R/V *Revelle* sounding from SP/MJO2 (Fig. 3.2). The idealized version of the *Revelle* sounding is generated by replicating the features of the mean sounding that are subjectively identified as robust. Robustness is assessed by varying the selected date range for the *Revelle* mean profile, comparing between different DYNAMO suppressed phases, and comparing with other DYNAMO sounding sites (not shown).

The mean *Revelle* sounding is characterized by a statically neutral surface layer with relative humidity RH  $\sim$  70%, and weakly stable PBL with RH increasing upward to  $\sim$ 95% near mixed-layer top (Fig. 3.2) (i.e., similar to suppressed phase mixed layers documented in COARE; Johnson et al. 2001). The robust character of static stability aloft (very similar in character to that at Gan Island; not shown) is a roughly two-mode structure, with a  $\theta$ -lapse rate of  $\sim$ 5 K km<sup>-1</sup> from 2~7 km, yielding to a lapse rate of  $\sim$ 3 K km<sup>-1</sup> thereafter, up to the tropopause around 14 km. RH decreases steadily above mixed-layer top to a minimum of  $\sim$ 20%, with a second peak of  $\sim$ 55% peaking around 17.5 km (similar to that in Fig. 2.2). The tertiary RH peak at 10–11 km in the *Revelle* mean sounding is deemed non-robust, and hence is neglected from the model sounding, by a comparison with other sounding locations and of other times, wherein it does not appear (cf. Fig. 13 of Johnson and Ciesielski 2013). Tests carried out offline demonstrate that this small RH peak has negligible impact to the simulated radiation (not

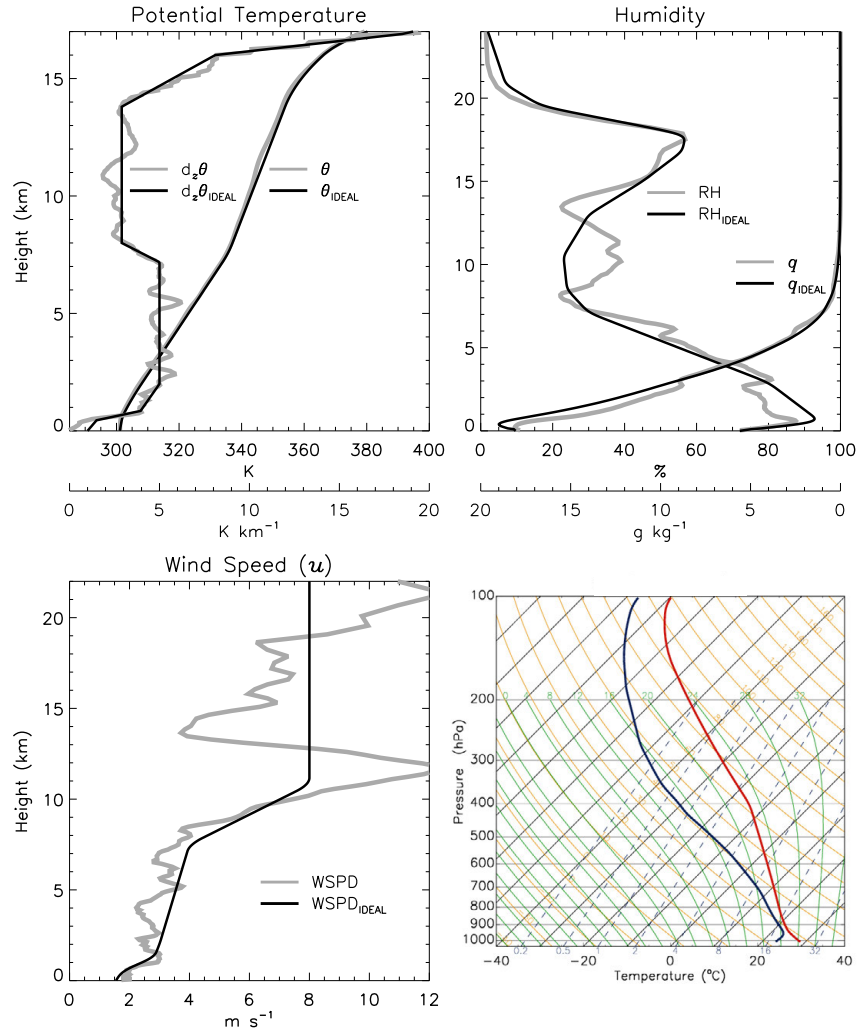


Fig. 3.2. Sounding used to prescribe the model base state. (top-left) Potential temperature  $\theta$  (K; upper abscissa) and the vertical  $\theta$  gradient ( $\text{K km}^{-1}$ ; lower abscissa), as indicated. (top-right) Relative humidity RH (%) ; upper abscissa) and mixing ratio  $q$  ( $\text{g kg}^{-1}$ ; lower abscissa). (bottom-left) Wind speed ( $\text{m s}^{-1}$ ), prescribed in the model as a positive zonal wind  $u$ . (bottom-right) Skew  $T$ - $\log p$  diagram of the idealized sounding. In all panels, gray curves are from the unmodified SP-MJO2-mean R/V *Revelle* sounding, and black curves are the idealized model input versions.

shown). The idealized model-input RH profile compares well with Fig. 2.2. Wind speed, applied in the model as a homogeneous zonal wind, exhibits little variation with height in the lower troposphere above the PBL, where it is slightly weaker due to friction. The model results are sensitive to the initial low-level wind speed, since this wind speed essentially sets the bottom

boundary condition for the model temperature and moisture budgets through the mean strength of surface fluxes. This wind-speed profile, however, results in fluxes that are consistent with observations from the corresponding period in DYNAMO (i.e., SP/MJO2; shown later). The wind speed aloft is highly simplified in the model profile since it exerts zero impact on the simulation results, given that moist convection remains shallow (shown later), and momentum is not exchanged across such a deep layer by convection.

There are several aspects in which external forcing is applied to prevent model drift. In nature, weak ascent occurs in the tropical lower stratosphere to oppose the warming due to radiative absorption by ozone, i.e., closely satisfying (3.1). This weak ascent is evident in  $w_{dyn}$  (Fig. 3.1). Such a balance is not applied in the model stratosphere, however, so  $\theta$  is instead relaxed toward the model base state above 13 km with a relaxation timescale  $\tau = 2$  h (although this relaxation would interfere with the diabatic heating from deep convection, the simulations described herein are devoid of deep convection). Furthermore, since friction would otherwise cause momentum to damp over time, the horizontal velocities are relaxed toward the base state throughout the column with  $\tau = 24$  h (base-state meridional wind  $v_0 = 0$ ). Base-state relaxation is imposed according to  $\partial\psi/\partial t = [\psi'(z, t) - \psi_0(z)]/\tau$ , where  $\psi$  is any prognostic variable.

Since these simulations are dominated by shallow convection, the dominant driving mechanism of  $w_{wtg}$  is net radiative cooling. Preliminary comparisons with observations suggest that the simulated longwave radiative cooling is slightly stronger than in nature. This can be deduced from the slight excess of subsidence in  $w_{wtg}$  in the low–midtroposphere compared to  $w_{dyn}$  (Fig. 3.1) (assuming that  $w_{dyn}$  is in radiative–convective balance). A possible cooling bias in the Goddard radiation scheme is the subject of an ongoing investigation, though the issue remains unresolved. Nevertheless, with a cooling bias in simulated radiation translating to too

strong of drying through  $w_{wtg}$ , the moisture budget is unbalanced in preliminary simulations that exclude any additional external moisture source. In particular, the drying by  $w_{wtg}$  overwhelms cumulus moistening, causing the troposphere to dry dramatically; and as a result of this drying, radiation then drifts further away from that in nature. For the purpose of examining the diurnal cycle over many days and in an environment maintains a state resembling nature, a constant advective moisture source ( $\partial_t q_{psc}$ ) is prescribed in the present simulations that nearly perfectly offsets the difference between convective moistening ( $\partial_t q_{conv}$ ; equal to surface evaporation in the column-integrated sense) and the drying by  $w_{wtg}$  ( $\partial_t q_{wtg}$ ) (Fig. 3.3).  $\partial_t q_{conv}$  is calculated by averaging the moistening over two days in a preliminary simulation in which the drying by  $w_{wtg}$  is non-active, thereby isolating the convective moistening. Since the total source  $\partial_t q_{net} = \partial_t q_{conv} + \partial_t q_{wtg} + \partial_t q_{psc} \approx 0$  in Fig. 3.3, this moisture budget is balanced by  $\partial_t q_{psc}$ . The moisture budget does not remain in a permanent state of balance, however, although it is steady enough to yield a set of at least eight full-day samples of the diurnal cycle for comparison between simulations. Furthermore, the manner and rate in which moisture drifts with time varies among the different simulations executed, which in itself reveals the nonlinear feedback of the diurnal cycle (the topic of section 3.4C).

### C) MODEL EXPERIMENTS

The primary suite of simulations for this study (described below) follows the setup described above. Each simulation is integrated from local midnight out for at least eight days. In order to allow the cloud field to initialize before the complete establishment of radiative cooling and subsidence, the radiative tendencies, prescribed moistening, and  $w_{dyn}$  profile are

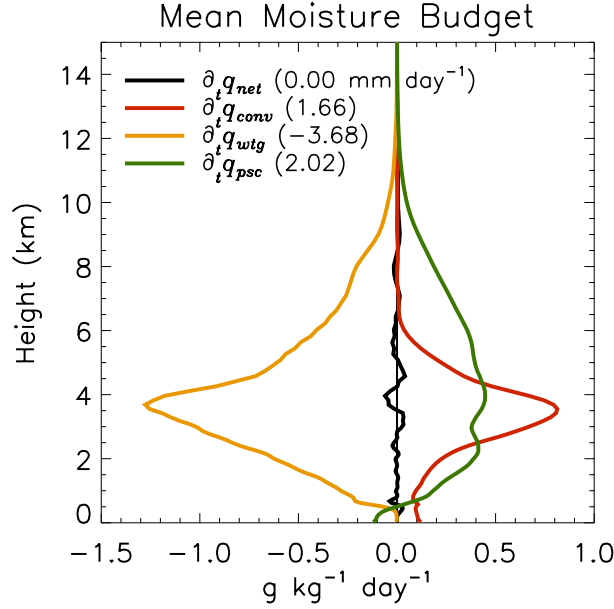


Fig. 3.3. Moisture budget ( $\text{g kg}^{-1} \text{ day}^{-1}$ ) averaged over two days of a preliminary simulation, including the total source ( $\partial_t q_{net}$ ; black), the convective source ( $\partial_t q_{conv}$ ; red), the source due to  $w_{wtg}$  ( $\partial_t q_{wtg}$ ; orange), and the prescribed advective source ( $\partial_t q_{psc}$ ; green).  $\partial_t q_{wtg}$  was calculated but not applied in this preliminary simulation, enabling isolation of  $\partial_t q_{conv}$ , and therefore, calculation of  $\partial_t q_{psc} = -(\partial_t q_{wtg} + \partial_t q_{conv})$ . Values in parentheses are the corresponding column-integrated values ( $\text{mm day}^{-1}$ ).

ramped up from zero to their original or predicted values over the first 12 h of each simulation ( $w_{wtg}$  thereby naturally ramps up in accordance with the radiative tendencies).

Since the diurnal cycle is forced in these simulations by only two processes – the diurnal cycle in SST and that in shortwave radiative heating (SW) – these two processes serve as the primary control variables for the modified physics tests, with the response in surface fluxes and moist convection serving as the dependent variable. Since only the diurnal clock is modified in the SW scheme, however, the radiation also freely responds to the cloud field.

The experiments are shown in Table 1. The control experiment (CTL) is forced with a regular diurnal cycle in SW and SST. A primary objective of this study is to assess the possible feedbacks between the diurnal cycle and longer timescales. If such a feedback exists, it can be

amplified and therefore more easily identified by lengthening the diurnal cycle. The experiment 48HDC does just that – otherwise identical to CTL, the period of the diurnal cycle of SW and SST in this simulation is increased to 48 h. In FIXSW, SW is fixed to its diurnal mean value by fixing the input time to 0621L (local time) (this time was established through trial and error).<sup>4</sup> In FIXSST, SST is fixed to the diurnal mean value of 29.9°C. In nature the diurnal cycles in SW and SST correlate (all else held fixed), so these experiments are highly idealized scenarios. Comparisons between FIXSST and FIXSW, however, will isolate the relative roles of diurnally varying SW and diurnally varying SST in the diurnal cycle of moist convection and the associated diurnal cycle of column humidity. In NODC, both SW and SST are fixed to their diurnal mean values. Therefore, comparisons between CTL, 48HDC, and NODC are particularly powerful for isolating the feedbacks (if present) between the diurnal cycle and longer timescales. Finally, In XCLDRAD, all species of water aside from vapor are set to zero in the input to the radiation scheme, thereby isolating the specific role of clouds in diurnal cycle–radiation feedbacks.

All simulations are integrated to 8 days, with the exception of NODC and XCLDRAD, which are integrated to 16 days for more complete assessment of the slow moisture drift (the topic of section 3.4.C). Output from these simulations is primarily presented in time–height series plots, with variables of interest averaged over the  $x$ - and  $y$ -dimensions. Although some complete eight-day (and sixteen-day) time series are provided, the majority of analyses employ only two or three (four or six) days (in 48HDC), since the simulations exhibit a high degree of persistence. The lack of persistence is highlighted where appropriate.

---

<sup>4</sup> The Goddard scheme in CM1 does not consider lateral cloud shading, so the only effect of fixing the time of day is to fix the insolation of each model column.

Special calculations are carried out to characterize the simulated cloud field. Analogous to the calculation of echo-top frequency for S-PolKa data (chapter 2.2.B), cloud-top frequency is calculated by normalizing the total occurrences of cloud top at a given height by the total number of horizontal grid points, and multiplying that result by 100% (cloud is defined where  $q_c + q_i \geq 0.05 \text{ g kg}^{-1}$ ). This quantity therefore includes both horizontal and vertical frequency information (e.g., cloud-top frequency of 100% would indicate that 100% of the domain includes cloud, 100% of which is at a given level). Cloud area coverage is the percentage of grid points containing any cloud, given the same  $q_c$  threshold.

Table 1. Overview of the model experiments, with experiment name across the top row modifications (“mods”), in the second–fourth rows, and total integration time in the last row.

	CTL	48HDC	FIXSW	FIXSST	NODC	XCLDRAD
SW mods	None	Period = 48 h	Fixed to 0621L	None	Fixed to 0621L	None
SST mods	None	Period = 48 h	None	Fixed to 29.9°C	Fixed to 29.9°C	None
Other mods	None	None	None	None	None	No cloud–rad. feedbacks
Integration time	8 days	8 days	8 days	8 days	16 days	16 days

#### D) THE APPARENT HEAT SOURCE AND MOISTURE SINK

To describe the characteristics of the simulated convection, the apparent heat source is reformulated in height coordinates in terms of  $\theta$  – the model prognostic temperature variable – and with  $w_{wtg}$  – the sole advective heat source:

$$Q_1 \equiv \frac{\partial \bar{\theta}}{\partial t} + w_{wtg} \frac{\partial \bar{\theta}}{\partial z} = Q_R + L_v (\bar{c} - \bar{e}) - \frac{\partial}{\partial z} (\overline{w'\theta'}) = Q_R + Q_c, \quad (3.7)$$

where  $Q_R$  is radiative heating,  $c$  is condensation,  $e$  is evaporation, and  $Q_c$  is the convective heating (calculated from  $Q_1 - Q_R$ ).  $Q_1$  is nearly equivalent to that of Yanai et al. (1973) multiplied by Exner function  $\Pi = (p / p_0)^{R_d/c_p}$ , where  $R_d$  is the gas constant for dry air and  $c_p$  is

the specific heat of dry air at constant pressure. Similarly, the apparent moisture sink is reformulated to include both  $w_{wtg}$  and the prescribed moisture source as

$$Q_2 \equiv -L_v \left( \frac{\partial \bar{q}}{\partial t} - \partial_t q_{psc} + w_{wtg} \frac{\partial \bar{q}}{\partial z} \right) = L_v (\bar{c} - \bar{e}) + L_v \frac{\partial}{\partial z} (\overline{w'q'}). \quad (3.8)$$

The “apparent” source or sink is the residual of the LHS in (3.7) and (3.8). For time tendencies discussed throughout this study, the units  $\text{K day}^{-1}$  correspond to the same measure of heating in 48HDC as they do in all other simulations, i.e.,  $1 \text{ K day}^{-1}$  corresponds to a heating of 1 K per 24 h, for 48HDC as for all other simulations.

### 3.4 Results

#### A) OVERVIEW OF CONTROL SIMULATION

The simulated cloud population in CTL exhibits clear day-to-day persistence, and is characterized by shallow clouds with maximum tops  $\sim 4.5$  km and cloud area coverage ranging from 4–8%, indicating their sparseness (Fig. 3.4). The narrow peak in cloud-top frequency between 0.5 and 1 km corresponds to the abundant cumuli at PBL top. The diurnal cycle manifests in several ways. The high-frequency belt of PBL-top cumuli ascends each afternoon, consistent with daytime PBL warming, deepening, and drying (shown later). The level of highest cloud tops ascends through evening, with a slightly lower midday peak in cloud tops (apparent on most days). The frequency of cloud tops between 2 and 4 km maximizes overnight when cloud tops are highest, implying relatively more vigorous nocturnal convection, long known to be a characteristic of tropical oceanic convection (Gray and Jacobson 1977). Cloud area coverage exhibits prominent midday peaks with slightly lower peaks overnight when clouds are deepest, with distinct minima during the transitions between the nocturnal and daytime

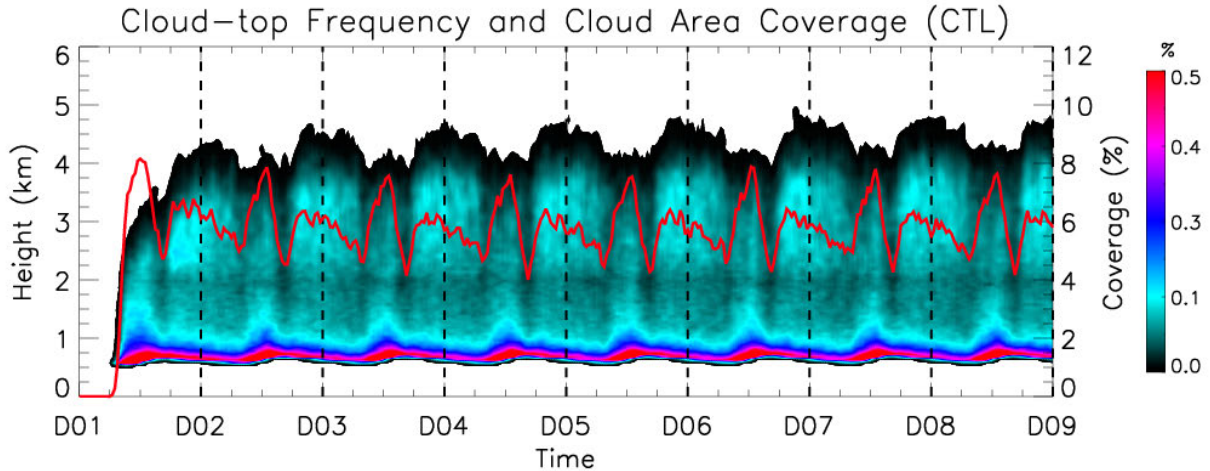


Fig. 3.4. Time–height series of cloud-top frequency (left ordinate; shaded; %) and cloud area coverage (right ordinate; red curve; %) in the control simulation (CTL). Here and henceforth, the abscissa ticks (and vertical dashed lines) are days (local midnight), beginning with the simulation start at midnight on day 1 (D01).

convective regimes. It is yet unclear why the daytime convection in CTL is characterized by substantially greater cloud area coverage than the nocturnal regime.

The corresponding DYNAMO observations from S-PolKa display a more distinct increase in the depth of echo tops and echo area coverage through morning, with tops exceeding 10 km during afternoon and overnight or early morning (Fig. 2.14). It is possible that mesoscale cloud organization, manifest on scales of 15~50 km in nature (Fig. 2.12 and 2.13), is not fully represented in this model, with a domain of  $\sim 100 \times 50$  km, thereby resulting in less vigorous forcing for convection in the model (Weckwerth et al. 1996). Regardless, the consistency between observations and the simulation in the appearance of both daytime and nocturnal peaks in cloud tops and cloud coverage, with relative minima between these regimes, is encouraging.

The corresponding time series of SST and rainfall (Fig. 3.5) displays distinct overnight rainfall maxima coinciding with the deepest clouds (Fig. 3.4), with relatively negligible rainfall during the day when SST peaks. A weak midday peak in rainfall is apparent on most days,

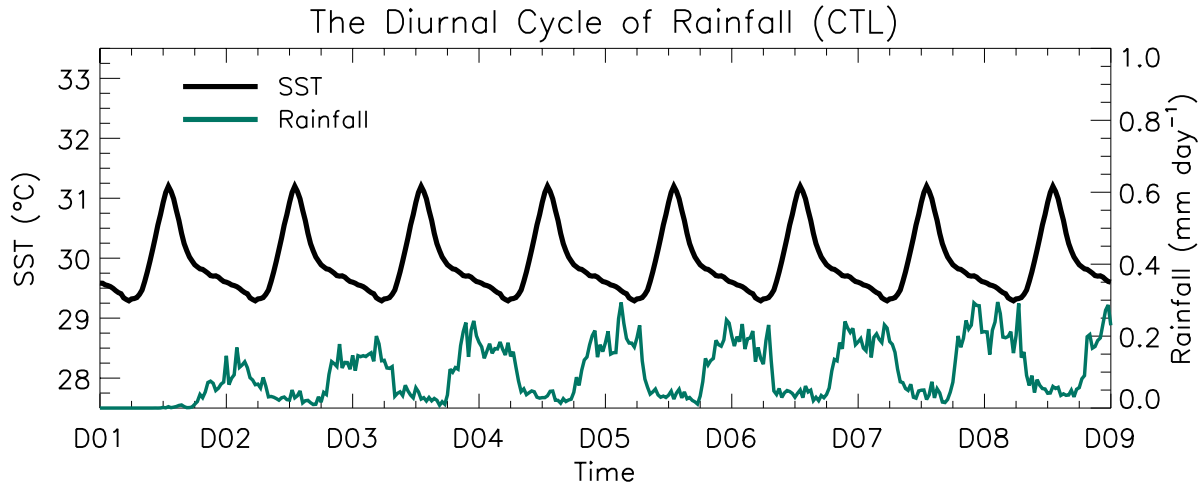


Fig. 3.5. Time series of SST (left ordinate; °C) and domain-averaged rainfall rate (right ordinate;  $\text{mm day}^{-1}$ ) in CTL.

however. This daytime–nighttime contrast is tied to the fundamental difference in character between the simulated daytime and nocturnal regimes of convection – a recurring theme of this study. The archetypal nocturnal rainfall maximum over open tropical oceans (Gray and Jacobson 1977; Sui et al. 1997; Dai 2001; Yang and Slingo 2001) implicates the role of diurnally varying SW, which suppresses convective vigor during the day by stabilizing the column (Randall et al. 1991; Yang and Smith 2006 and references therein).

Rainfall in CTL is substantially less than that in DYNAMO observations (Fig. 2.15); furthermore, observations exhibit greater afternoon–evening rainfall. One possibility is that part of the large-scale forcing, i.e., in vertical motion, in the DYNAMO array is associated with the diurnal cycle of ITCZ convection, as discussed in section 2.4. This issue remains unresolved, however. Rainfall subtly increases from day to day in Fig. 3.5 (more evident in 48HDC; shown later), despite the moisture budget being in near-perfect balance (Fig. 3.3). This increase relates to a subtle drift in the column moisture, which serves as the topic of section 3.4.C.

With little diurnal variation in domain-averaged wind speed, domain-averaged latent and sensible heat fluxes (LH and SH, respectively) strongly correlate with the diurnal cycle in SST (Fig. 3.6). Comparison between Figs. 3.4 and 3.6 indicates the close relationship between surface fluxes and cloud area coverage during the day. More about this relationship can be inferred from a comparison of surface  $\theta'$  between 0000 and 1200L (the prime here denotes the spatial anomaly at a given time, while “surface” refers to the lowest scalar level at 25 m) (Fig. 3.7). The clearest result of this comparison is that the scale of anomalies is larger at 0000L than at 1200L by a factor of at least two (compare anomalies of 5~10 km scale in Figs. 3.7a,c,e with those of 1~5 km in Figs. 3.7b,d,f). So despite a greater frequency of *deep* clouds nocturnally, clouds in general peak in areal coverage during the day in connection with enhanced surface fluxes, PBL circulations of a horizontal scale that more closely matches the depth of the PBL, and hence a greater occurrence of PBL-rooted convection (Figs. 3.4, 3.6, and 3.7). The increase in the scale of anomalies overnight is associated with the spreading of larger and/or stronger cold pools due to stronger convection and greater rainfall (Figs. 3.4 and 3.5).

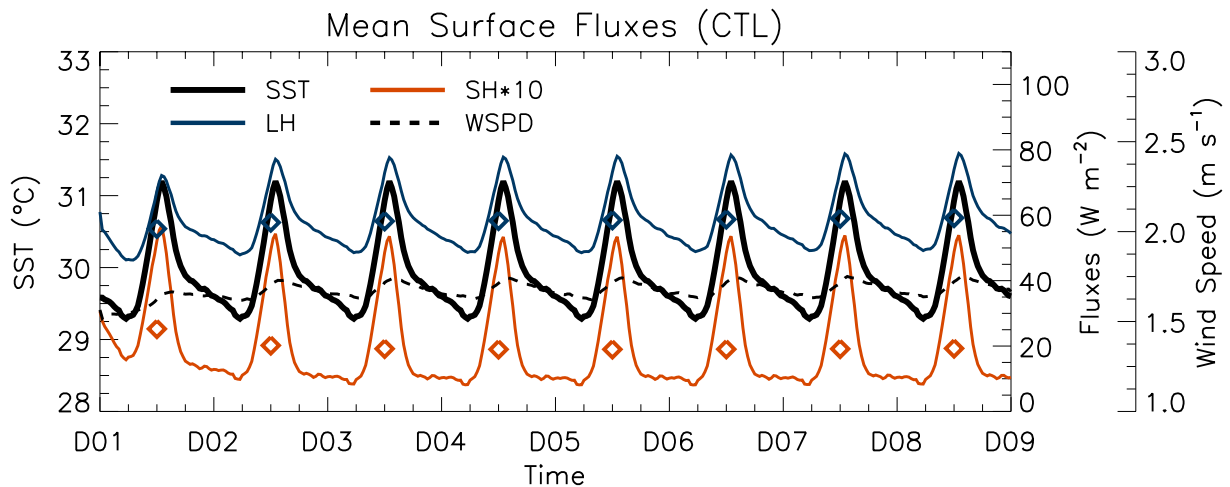


Fig. 3.6. SST (left ordinate; black solid, °C) with domain-averaged latent (blue) and sensible ( $\times 10$ ; red) heat flux (inner-right ordinate;  $\text{W m}^{-2}$ ) and surface (i.e., lowest scalar level at 25 m) wind speed (outer-right ordinate; black dashed;  $\text{m s}^{-1}$ ) in CTL. Blue and red open squares are the daily-mean (midnight–midnight) latent and sensible heat flux values, respectively.

The daytime increase in surface fluxes and PBL-rooted convection is also the cause of the minor daytime increase in wind speed apparent in Fig. 3.6. That wind speed does not vary diurnally as much in the model as in R/V *Revelle* observations during SP/MJO2 (i.e., 2~3 m s<sup>-1</sup>; Figs. 2.10 and 2.11b) may relate to the lack of deeper (i.e.,  $\geq 10$ -km) convective systems that develop in the afternoon during SP/MJO2 (Fig. 2.14). The larger diurnal cycle of wind speed in nature may also be tied to very small-scale PBL thermals that the model does not properly simulate.

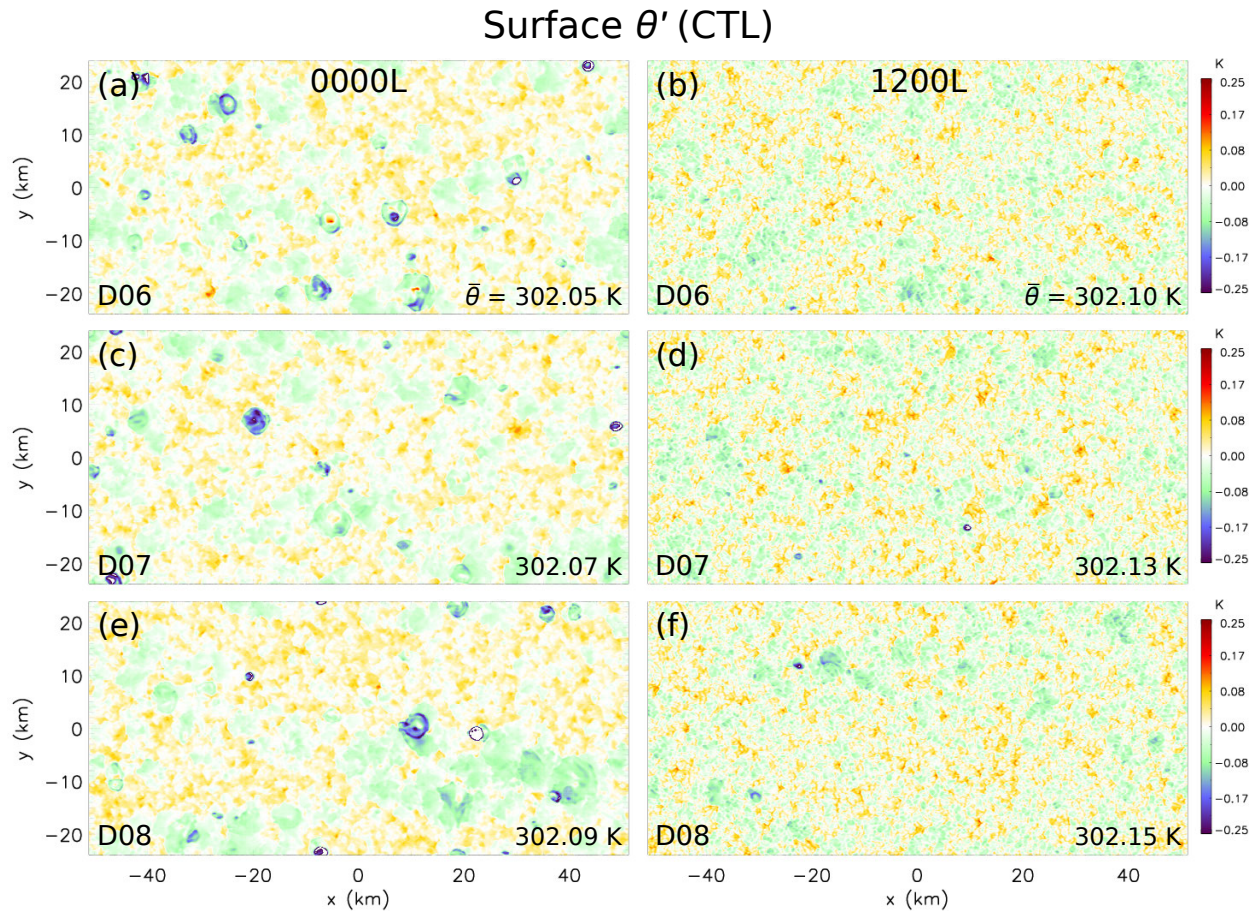


Fig. 3.7.  $\theta'$  (spatial anomaly; K) at the lowest model level (25 m) in CTL at the times (local time, L) and days indicated in each panel. Domain-mean values are indicated in lower-right corner of each panel.

As expected,  $Q_1$  is dominated by radiative cooling, which is largely offset by deep subsidence warming (Figs. 3.8a,b and 3.9a) (only two days are shown since the diurnal cycle is virtually identical from day to day).  $Q_R$  exhibits nocturnal cooling of  $\geq 2 \text{ K day}^{-1}$  through much of the midtroposphere. The warming due to SW is apparent from 0500~1900L, with weak warming around noon. The strong  $Q_1$  cooling that peaks around 3.5 km relates to evaporative cooling of cloud water, as indicated by  $Q_c < 0$  from 3~4.5 km (Fig. 3.9b), and is counteracted by enhanced subsidence warming in the same layer (Fig. 3.8b). Strong midday PBL warming is evident in  $Q_1$  and  $Q_c$  in association with large vertical eddy heat flux convergence in that layer with SST and SH at their peak magnitudes (Figs. 3.6, 3.8a, and 3.9b). Although this PBL heating rapidly decreases as SH wanes, the depth of  $Q_c$  warming rapidly increases from the PBL to ~2 km from 1700–1800L due to increasing condensation warming as nocturnal convection ramps up (Fig. 3.4). The evaporative cooling above this layer simultaneously intensifies.

The diurnal cycle of vertical motion (as inferred from Fig. 3.8b) is quite consistent with that from DYNAMO observations during SP–MJO2 (Fig. 2.16b). In particular, the weakest subsidence (or greatest ascent) appears in the early–mid-afternoon, with the strongest subsidence in the early-morning hours. While the role of diurnal pulsation of the Hadley cell (Deser and Smith 1998; McNoldy et al. 2004) in the observed diurnal cycle of vertical motion over the northern sounding array is yet unclear, it is likely that this vertical motion signal is in near-radiative balance, as supported by the consistency between Figs. 2.16b and 3.8b.

In the current framework, the argument that convection pulses diurnally in response to the radiative heating cycle alone is incomplete, since  $w_{wtg}$  is always operating to offset radiative cooling (or warming) (Figs. 3.8b and 3.9a). A more complete statement is that the convection

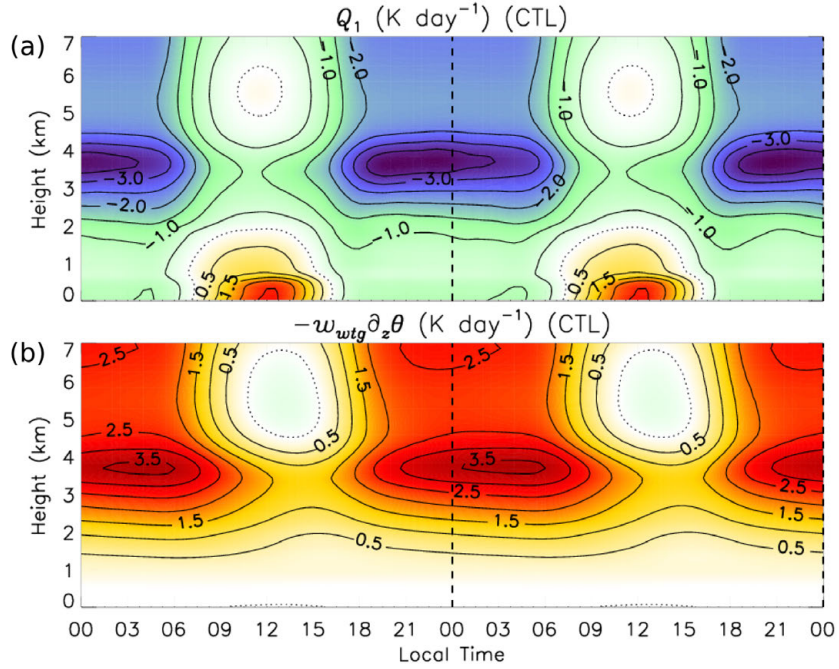


Fig. 3.8. Time–height series spanning D04 and D05 (L indicated along abscissa) of (a) the apparent heat source  $Q_1$  and (b) the advective heat source due to  $w_{wtg}$  (in the Eulerian perspective) (contour interval CI = 0.5 K day<sup>-1</sup>) in CTL. Both terms have been multiplied by  $c_p$ . The dotted contour marks the zero value, here and henceforth.

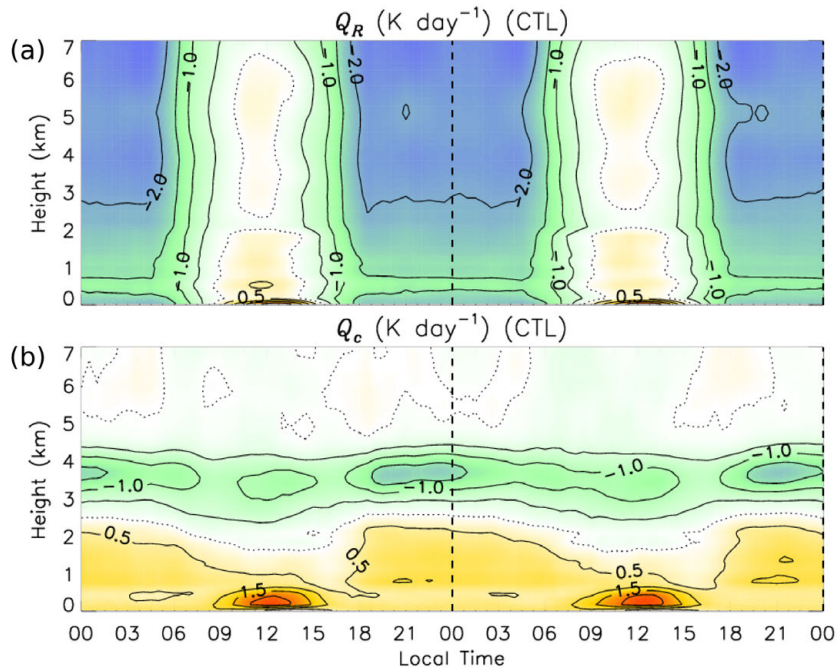


Fig. 3.9. As in Fig. 3.8, except for (a) the radiative heat source  $Q_R$  and (b) the convective heat source  $Q_c = Q_1 - Q_R$ .

pulses diurnally in response to the offset, or residual, between radiative cooling and subsidence warming driven by  $w_{wtg}$ , namely,

$$Q_{resid} \equiv Q_R - w_{wtg} \frac{\partial \bar{\theta}}{\partial z}. \quad (3.9)$$

(It is technically incorrect to treat the diurnal cycle of convection as a “response” in this sense, since its effects on diabatic heating modulate both radiation and  $w_{wtg}$ ; this thought experiment can be insightful, nonetheless.) The clearest signal in  $Q_{resid}$  is the strong warming from 0500~1300L in the layer 2~4.5 km, which acts to suppress daytime convection as indicated by the positive anomaly in  $\theta'$  (i.e.,  $\theta$  with diurnal mean removed) that appears in response to this warming (Figs. 3.10a,b). Recall that  $w_{wtg}$  responds to temperature anomalies with some delay, which is longer for shallower temperature anomalies, via (3.6). Therefore, with enhanced subsidence fully established by nocturnally enhanced evaporative cooling and the associated cold anomaly (Figs. 3.8b and 3.9b), the rapid increase in  $Q_R$  in the morning as SW increases and subsidence persists leads to a large increase in  $Q_{resid}$  that warms the upper cloud layer (Figs. 3.9a and 3.10a). In the afternoon, in contrast,  $Q_{resid}$  rapidly decreases in the 2~4-km layer as SW shuts off, since by this time evaporative cooling has relaxed, the cold anomaly has been replaced by a warm anomaly owing to persistent subsidence, and  $w_{wtg}$  subsidence has therefore finally relaxed (Figs. 3.9a,b and 3.10a,b). This reduction of warming in  $Q_{resid}$  therefore leads to the rapid establishment of nocturnal convection (Fig. 3.4).

In accordance with this diurnal cycle in  $\theta'$  aloft, the diurnal cycle in vertical stability  $\partial\theta'/\partial z$  exhibits negative values in the cloud layer (i.e., 2~3.5 km) at times when  $\theta' < 0$ , with the opposite holding true when  $\theta' > 0$  (Figs. 3.10b,c). The narrow, low-level bands of negative and positive anomalies in  $\partial\theta'/\partial z$  reflect the deeper evening mixed layer and shallower

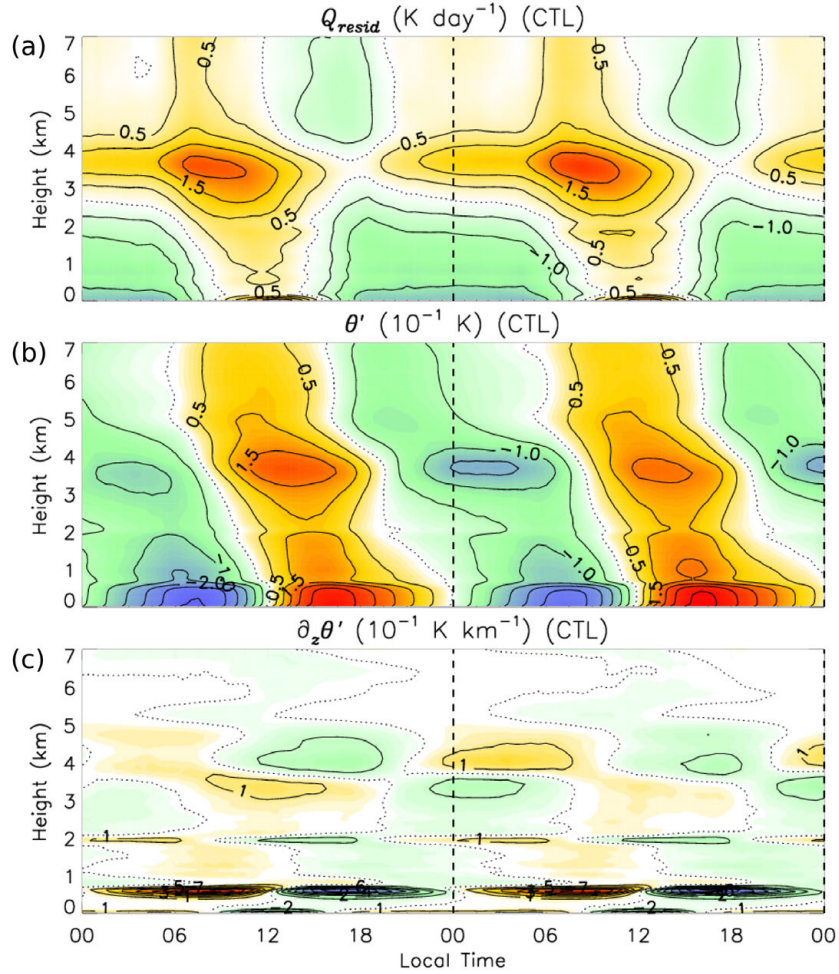


Fig. 3.10. As in Fig. 3.8 except for (a) the “residual” heat source  $Q_{resid}$  ( $CI = 0.5 \text{ K day}^{-1}$ ), (b)  $\theta'$  (i.e.,  $\theta$  with diurnal mean removed) ( $CI = 0.5 \times 10^{-1} \text{ K}$ ), and (c)  $\partial\theta'/\partial z$  ( $CI = 10^{-1} \text{ K km}^{-1}$ ).

nighttime–early-morning mixed layer, respectively. The mean character of the mixed layer appears clearly as a surface-based isentropic layer of  $\sim 600\text{-m}$  depth (Fig. 3.11). The diurnal variation of mixed-layer depth, as indicated in stability, closely correlates with the PBL diurnal temperature anomaly, which reaches its peak (minimum) value in the late afternoon (early morning). This diurnal cycle is consistent with the diurnal cycle in surface fluxes (Fig. 3.6), and agrees with observations from COARE (Johnson et al. 2001). Immediately above the mixed layer, the stability exhibits weakly negative values in the afternoon in connection with daytime PBL warming, which deepens into the greater cloud layer as the cold anomaly develops aloft.

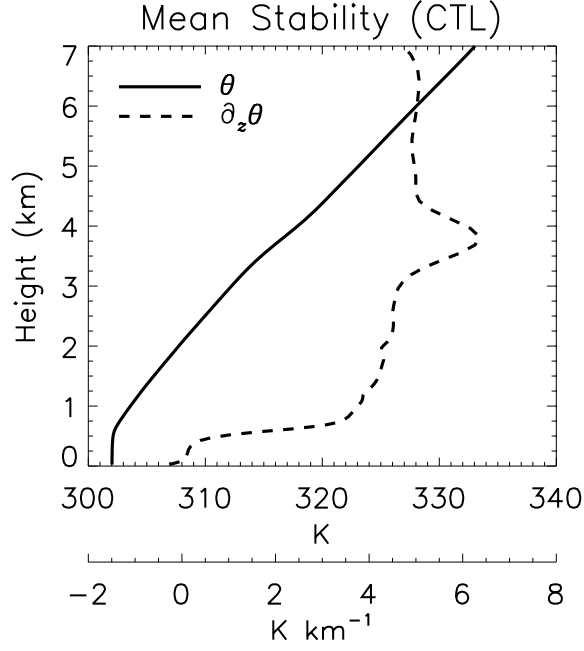


Fig. 3.11. Vertical profiles of  $\theta$  (solid; CI =  $0.5 \times 10^{-1}$  K; upper abscissa) and  $\partial\theta/\partial z$  (dashed; CI =  $10^{-1}$  K km $^{-1}$ ; lower abscissa) averaged over the time periods shown in Fig. 3.10.

Therefore, both the midday PBL warming and the upper-level cooling due to enhanced evaporation and reduced  $Q_{resid}$  appear to effectively destabilize the column. The profiles of mean  $\theta$  and  $\partial\theta/\partial z$  reveal that the mean state is stable (i.e., similar to the base state; Fig. 3.2) (Fig. 3.11); the diurnal variation of stability, however, clearly impacts the nature of the moist convection.

More about the contrasting character between the nocturnal and daytime convective regimes can be elucidated by examination of the vertical eddy fluxes of energy. The vertical eddy fluxes are calculated as follows:

$$\text{Vertical eddy moisture flux} = \rho L_v \overline{w'q'}, \quad (3.10a)$$

$$\text{Vertical eddy heat flux} = \rho c_p \overline{w'\theta'}, \quad (3.10b)$$

$$\text{Vertical eddy buoyancy flux} = \rho c_p \cdot \overline{w'\theta'_v}, \quad (3.10c)$$

where  $\rho$  is the density of moist air,  $\theta_v$  is virtual potential temperature, and the primes denote deviations from the horizontal average at a given time. The dominance of the moisture flux over the total energy flux (i.e., moisture flux plus heat flux) is consistent with previous studies of trade cumulus regimes (Betts 1975) (Figs. 3.12a,b). Beyond the general magnitude difference, however, there is a prominent contrast in the diurnal phasing and elevation of peak moisture and heat fluxes. Eddy moisture flux exhibits a peak of  $\sim 90 \text{ W m}^{-2}$  in association with shallow, PBL-rooted daytime convection, which coincides with the time of peak SST and LH (Fig. 3.6). Eddy heat flux exhibits a negative peak in the PBL at this time due to free-convective eddies that overshoot their equilibrium level at mixed layer top (LeMone and Pennell 1976). Eddy heat flux maximizes ( $\sim 6 \text{ W m}^{-2}$ ) overnight in the 2~3-km layer in association with the more vigorous nocturnal convection, during which time the majority of the rainfall is received (Fig. 3.5). Moisture fluxes are greatly reduced in the nocturnal convection compared to their midday values, though appreciable fluxes reach  $\sim 4 \text{ km}$  overnight.

Buoyancy flux yields a clear distinction between the daytime and nocturnal convective regimes (Fig. 3.12c). During the day, buoyancy fluxes peak at low levels due to large surface fluxes, which drive numerous small-scale, PBL-rooted convective eddies that flux moisture upwards (Figs. 3.4, 3.6, 3.7, and 3.12a). At night, in contrast, buoyancy fluxes peak above the PBL, indicating that the convective eddies do not originate from the PBL. Therefore, the nocturnal convective eddies must owe their existence to the combination of 1) peak  $Q_R$  cooling (and reduced  $Q_{resid}$ ) and 2) peak evaporative cooling in the 2~4-km layer, which supports the cloud layer instability (Figs. 3.9a,b and 3.10a–c). Given that the evaporative cooling is brought about by reduced  $Q_R$  and  $Q_{resid}$ , however, the nocturnal convection more fundamentally owes to the diurnal cycle in radiation, consistent with prior studies (Randall et al. 1991).

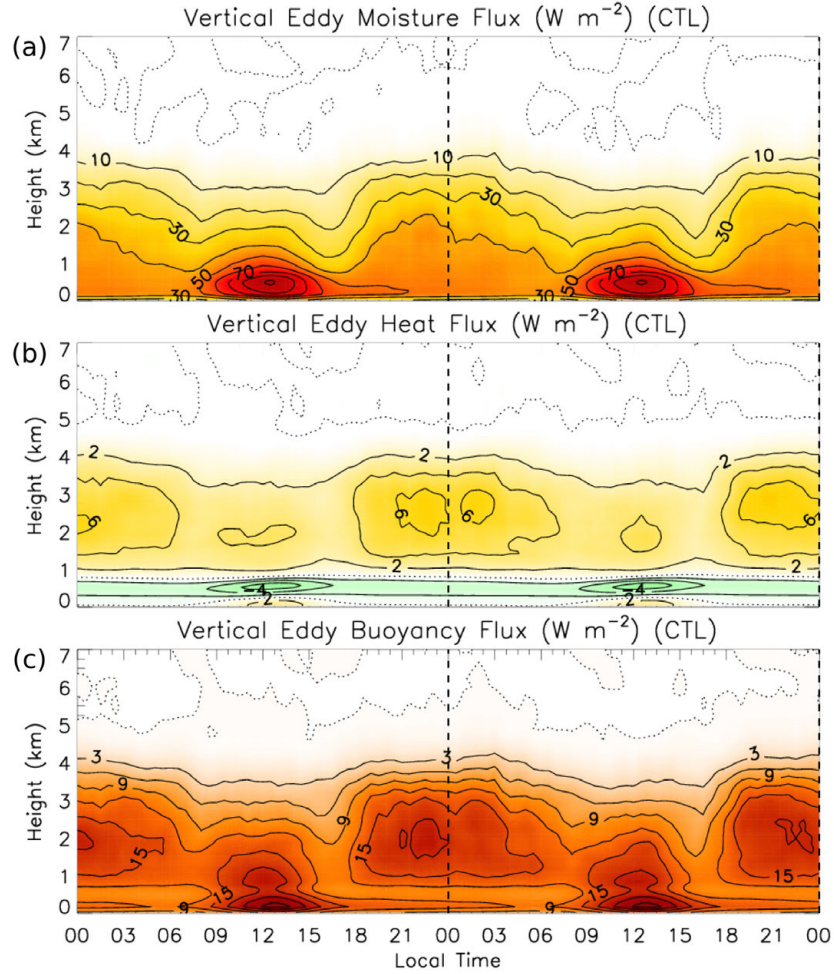


Fig. 3.12. As in Fig. 3.8 except for (a) vertical eddy moisture flux (CI = 10), (b) heat flux (CI = 2), and (c) buoyancy flux (CI = 3) ( $\text{W m}^{-2}$ ).

The diurnal cycle in  $Q_2$  mirrors the distinction between nocturnal and daytime convection (Fig. 3.13a). Nocturnally, there is drying above the boundary layer due to condensation and/or divergence of eddy moisture flux, with evaporative moistening aloft that maximizes in sync with evaporative cooling (Fig. 3.9b). The PBL moistens overnight. During the day, the drying is shifted to the PBL, with moistening aloft. Averaged over a day, the mean  $Q_2$  profile resembles that determined from field campaigns that sampled trade cumulus regimes (Nitta and Esbensen 1974; Johnson and Lin 1997); however, the results here show that those mean profiles consist of profound diurnal variations.

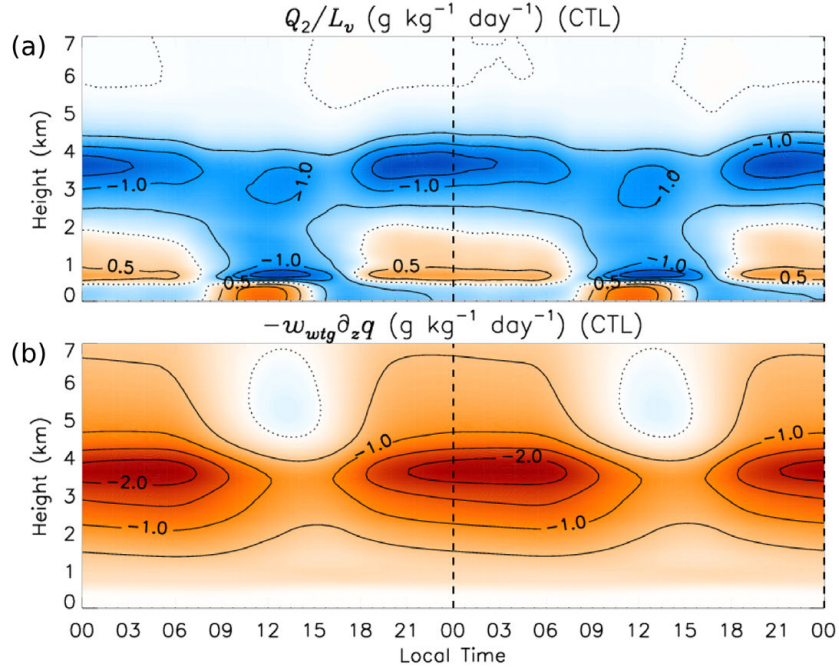


Fig. 3.13. As in Fig. 3.8 except for (a) the apparent moisture sink  $Q_2/L_v$  and (b) the advective moisture source due to  $w_{wtg}$  (in the Eulerian perspective) (contour interval  $CI = 0.5 \text{ g kg}^{-1} \text{ day}^{-1}$ ; multiplying by 2.5 gives the approximate tendency in units of  $\text{K day}^{-1}$ ).

The local time-tendency of  $q$   $\partial_t q$  resembles  $Q_2$  during the day, although nocturnally the cloud moistening from 2~4.5 km is overwhelmed by the subsidence drying due to  $w_{wtg}$ , leading to a net drying in the local tendency (Fig. 3.13b and 2.14a). Moistening in  $\partial_t q$  in fact reaches greater depth than the cloud moistening indicated in  $Q_2$ , revealing the secondary role of  $w_{wtg}$  (i.e., relaxed subsidence or weak rising motion) at moistening the column during the day.

The diurnal variation in  $q'$  (i.e.,  $q$  with diurnal mean removed) closely resembles both the phase and amplitude of that during SP–MJO2 in DYNAMO, with relatively dry conditions in the first half of the day, moist conditions in the second, and a magnitude change of  $0.3\text{--}0.4 \text{ g kg}^{-1}$  (Figs. 2.16b and 3.14b). The anti-correlation between moisture in the PBL and that aloft, though remarkably clear in the simulation, is subtler in the DYNAMO observations (i.e., mostly apparent in the afternoon–evening; Figs. 2.16a,b). This signal in low-level moisture has been

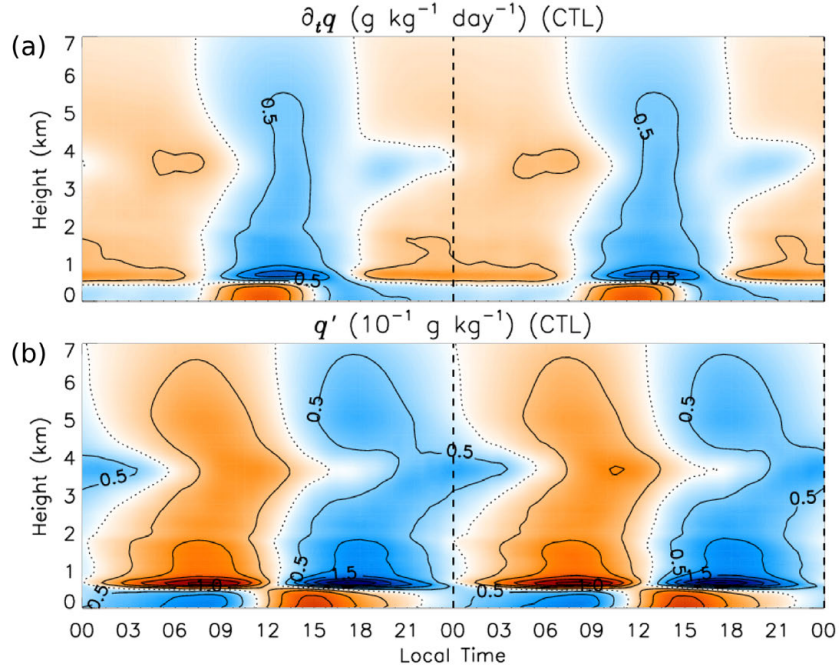


Fig. 3.14. As in Fig. 3.8 except for (a) the local time-tendency of  $q$   $\partial_t q$  ( $\text{g kg}^{-1} \text{day}^{-1}$ ) and (b)  $q'$  (i.e.,  $q$  with diurnal mean removed) ( $10^{-1} \text{g kg}^{-1}$ ) (CI = 0.5).

documented in other field campaigns, however, though it has never been explained (Sui et al. 1997; Yasunaga et al. 2008). These modeling results can shed light on this process. That the PBL dries during the day despite enhanced moistening from the surface (Fig. 3.6) indicates the effectiveness with which PBL-based convective eddies – at peak activity at midday – scour the moisture from the PBL and deposit it aloft (Figs. 3.12a,c). At other times of day, when there are less PBL-rooted convective eddy transports, the PBL is moistened by surface evaporation.

The largest difference between the simulation and observations is in  $Q_2$ , namely, in the enhanced  $Q_2$  moistening associated with nocturnal evaporation aloft (Fig. 3.13a). It is unclear how sensitive this feature is to the microphysics scheme employed. Since this nocturnal moistening is more-than-offset by subsidence drying due to  $w_{wtg}$ , however, the local time variation of humidity in the model is very consistent with that in observations (Figs. 2.16, 3.13b, and 3.14a,b).

Owing to the lack of high-time-resolution surface flux measurements over the DYNAMO northern sounding array, the diurnal cycle of the moisture budget cannot be constrained from observations. This can be accomplished from the model, however. From (3.8), the vertically integrated moisture budget can be written in the Eulerian framework as follows:

$$\left\langle \frac{\partial \bar{q}}{\partial t} \right\rangle \equiv \left\langle \partial_t q_{psc} \right\rangle - \left\langle w_{wtg} \frac{\partial \bar{q}}{\partial z} \right\rangle + E_0 - P_0, \quad (3.11)$$

where  $E_0 = LH/L_v$  is surface evaporation,  $P_0$  is precipitation,  $\langle \cdot \rangle = 1/g \int_{p_{trop}}^{p_{sfc}} (\cdot) dp$ ,  $g$  is gravity, and  $p_{sfc}$  ( $p_{trop}$ ) is surface (tropopause) pressure. The moisture budget is a clear demonstration of the balanced state brought about by inclusion of  $\partial_t q_{psc}$ , with the daily-mean local  $q$ -tendency sitting nearly at zero (Fig. 3.15). The local tendency is characterized by  $\sim 3 \text{ g kg}^{-1} \text{ day}^{-1}$  ( $90 \text{ W m}^{-2}$ ) of moistening at midday when SST, surface fluxes, and PBL-rooted eddy moisture fluxes are at peak amplitude and  $w_{wtg}$  subsidence is at a minimum (with weak ascent at midlevels) (Figs. 3.6, 3.12c, and 3.13a,b). It then reaches a weaker minimum at approximately  $-2 \text{ g kg}^{-1} \text{ day}^{-1}$  ( $50\sim 60 \text{ W m}^{-2}$ ) of drying overnight, though for a more extended period than the daytime moistening. The smallness of the diurnal variation in  $E_0$  is due to the smallness of the diurnal variation of surface wind speed discussed previously (Fig. 3.6). Weak nocturnal drying by rainfall ( $P_0$ ) is apparent, though this term clearly pales in comparison with the others.

The most conspicuous result from Fig. 3.15 is the high degree to which subsidence drying by  $w_{wtg}$  “throttles” the overall moisture tendency, with marked variations from  $2\sim 6 \text{ g kg}^{-1} \text{ day}^{-1}$  ( $40\sim 170 \text{ W m}^{-2}$ ) of drying from day to night. Although  $w_{wtg}$  always acts as a column moisture sink, its variation either more-than-offsets the other moisture sources (nocturnally), or enables them to moisten the column (daytime hours). Since  $w_{wtg}$  acts largely in response to the diurnal

variation of  $Q_R$ , it follows that the diurnal cycle of  $Q_R$  is the fundamental driver of variations in the net column moisture source (Figs. 3.8b and 3.9a).

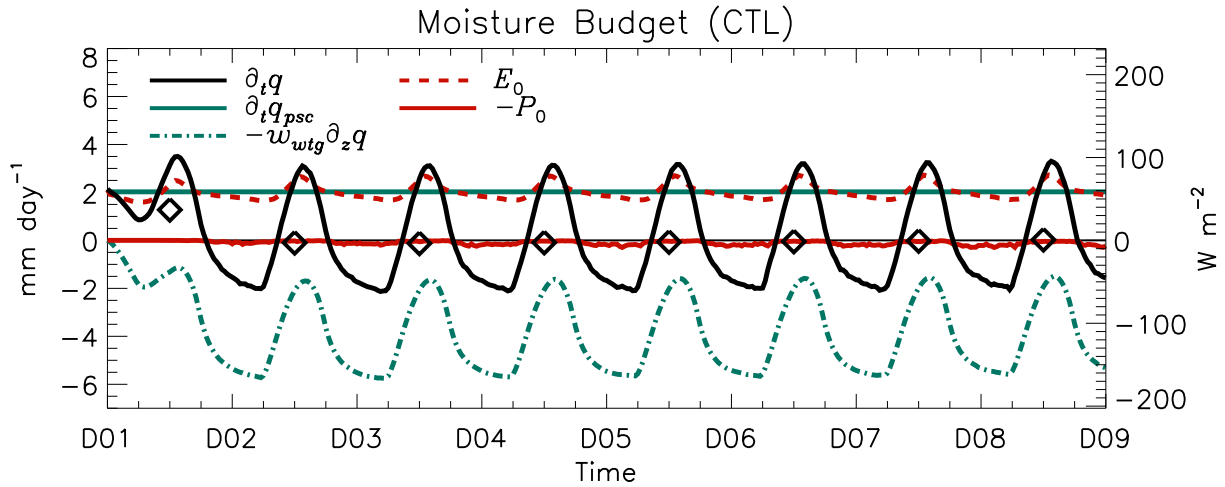


Fig. 3.15. Column-integrated and domain-averaged moisture budget for CTL, with the local time-tendency  $\partial_t q$  (black), the prescribed source  $\partial_t q_{psc}$  (turquoise solid), the advective source due to  $w_{wtg}$  (turquoise dot-dashed),  $E_0$  (red dashed), and  $-P_0$  (red solid) ( $\text{mm day}^{-1}$  along the left ordinate;  $\text{W m}^{-2}$  along the right). Daily-averaged values of  $\partial_t q$  are indicated by the black squares at noon each day (as a reference, the trend in  $\partial_t q$  largely follows that of  $Q_R$ ; Fig. 3.9a).

## B) MODIFIED PHYSICS TESTS

The distinct processes that drive nocturnal and daytime convection are clearly isolated by the sensitivity tests employed. Compared to CTL, FIXSST exhibits enhanced nocturnal convection with no evidence of the daytime convective regime in either cloud-top frequency or cloud area coverage (Figs. 3.16a,b). In FIXSW, in contrast, the daytime peak in cloud area coverage is enhanced relative to CTL, with no nocturnal enhancement of convection (Fig. 3.16c). Although cloud-top frequency indicates that some deep clouds (i.e., those exceeding  $\sim 4$  km in depth) occur throughout the day, cloud-top frequency clearly increases in the middle of the day in accordance with enhanced surface fluxes (Fig. 3.6). 48HDC resembles CTL stretched out in time by a factor of two (Fig. 3.16d). Clouds in 48HDC, however, penetrate to slightly greater

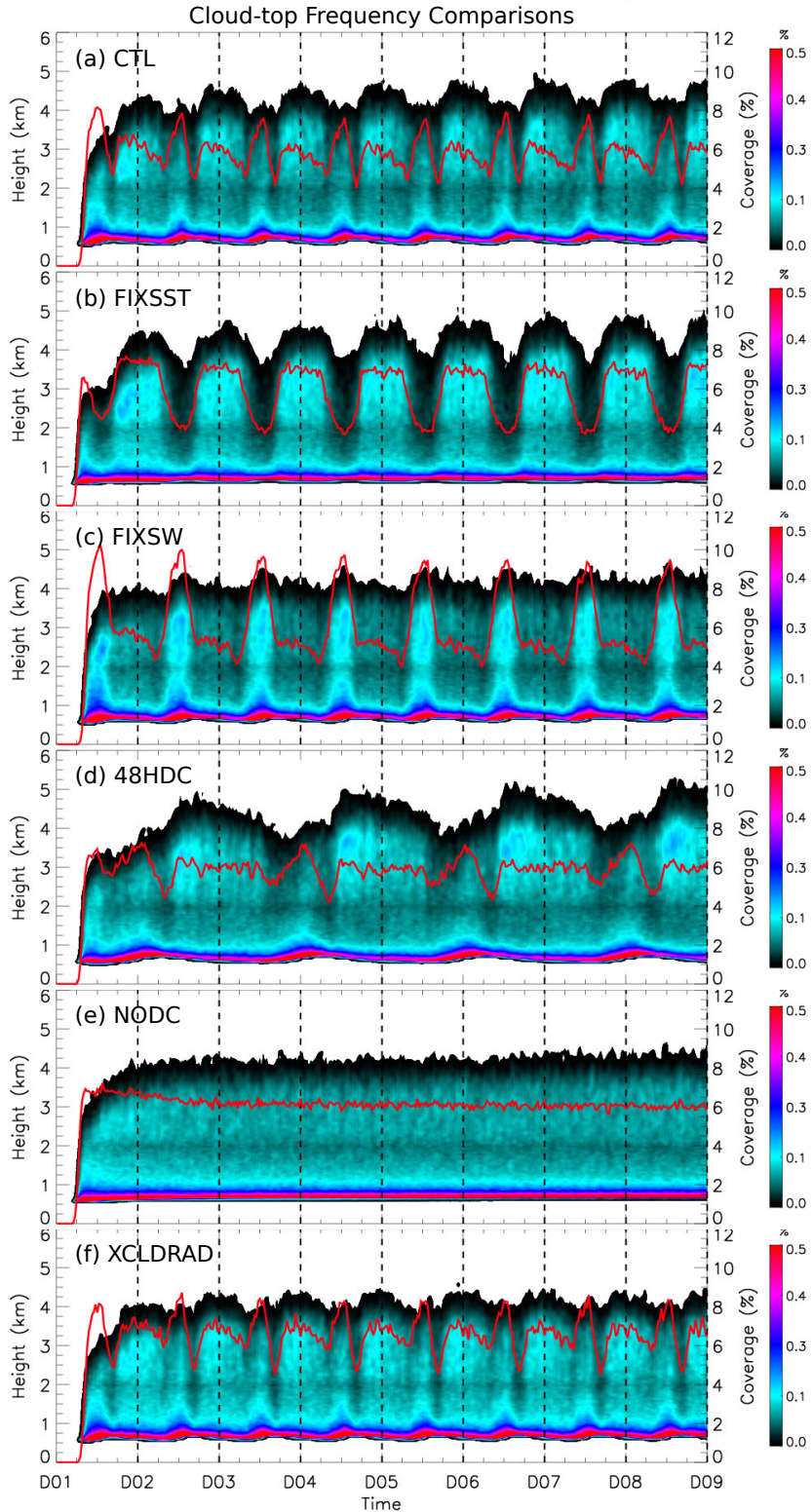


Fig. 3.16. As in Fig. 3.4 except for (a) CTL, (b) FIXSST, (c) FIXSW, (d) 48HDC, (e) NODC, and (f) XCLDRAD. Dashed lines in (d) correspond to diurnal cycle midnight, i.e., with 48-h period.

depth (~5 km) than in CTL during the onset of the nocturnal regime, while they are shallower in the late morning, thereby creating a more emphasized transition in cloud depth from midday–evening. This feature relates to a nonlinear feedback in the diurnal cycle that is amplified by the stretched diurnal cycle (the topic of section 3.4.C). NODC looks simply like a smoothed version of CTL, with no trace of a diurnal cycle, maximum cloud tops of ~4 km, and cloud area coverage of 6~7% throughout the simulation (Fig. 3.16e). The only clear change in XCLDRAD relative to CTL is a slight enhancement of cloud-top frequency at all times (Fig. 3.16f). The cause for this difference will be discussed in section 3.4.C.

The rainfall time series reveals pronounced differences between the simulations (Fig. 3.17). Most obviously, many of the simulated rainfall rates increase with time, and in some this increase occurs more rapidly (i.e., 48HDC) than in others (i.e., NODC). This difference in drift rates will be the topic of the next section. Generally, rainfall amounts are quite miniscule in accordance with large-scale subsidence, although rainfall varies by a factor of ~2.7 across the suite of simulations (excluding XCLDRAD) simply by modifying the diurnal cycle (compare total accumulated values in 48HDC and FIXSW). Rainfall is greatest in 48HDC, which exhibits a more pronounced peak early in the nocturnal convective regime than in other simulations, which coincides with enhanced cloud-top frequency around the same time (Fig. 3.16d). Surprisingly, excluding the diurnal cycle of SST (i.e., FIXSST) leads to a minor increase in rainfall relative to CTL (compare ~1 mm of accumulated rain in FIXSST to ~0.8 mm in CTL), despite dramatic reduction in the diurnal cycle of surface fluxes (Fig. 3.18a). It is not yet clear why this difference between rainfall in CTL and that in FIXSST exists. FIXSW, however, exhibits very little rainfall relative to CTL, despite very similar diurnal cycles in surface fluxes (Figs. 3.6 and 3.18b). The rainfall received in FIXSW maximizes during the day when surface

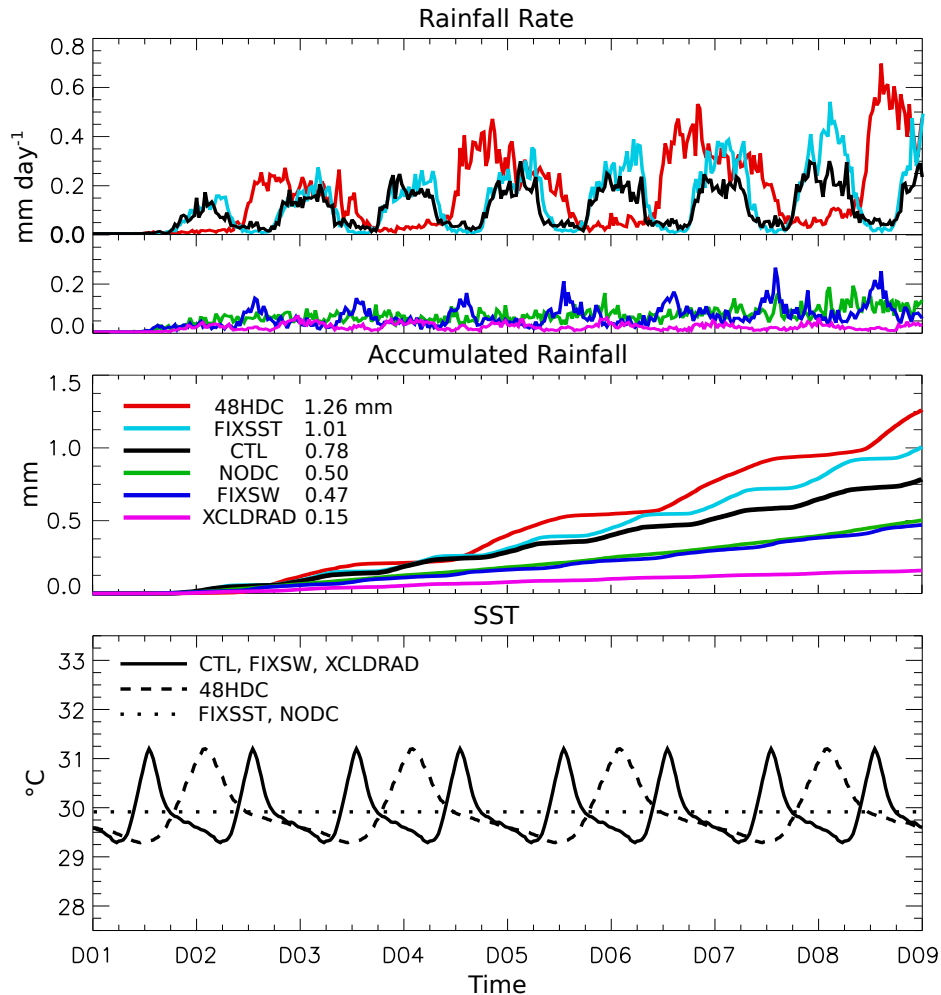


Fig. 3.17. Time series of (top) domain-averaged rainfall rate ( $\text{mm day}^{-1}$ ), (center) accumulated rainfall (mm), and (bottom) SST ( $^{\circ}\text{C}$ ) for all simulations according to the legends. Rainfall rate is separated into two abscissas for clarity purposes. Total simulation end-time accumulated rainfall values are provided for each simulation in the legend of the center panel.

fluxes are greatest, reflecting the propensity for enhanced surface fluxes to invigorate convection (Figs. 3.6 and 3.12c). NODC also exhibits negligible rainfall relative to CTL, and with no detectable diurnal cycle in either rainfall or surface fluxes, as expected (Fig. 3.18d). Perhaps the most surprising result is the degree to which the cloud–radiative feedback accounts for rainfall in CTL: despite a very similar cloud field, and a nearly identical diurnal cycle in surface fluxes, XCLDRAD produces negligible rainfall relative to CTL (Figs. 3.16f and 3.18e). A clear result

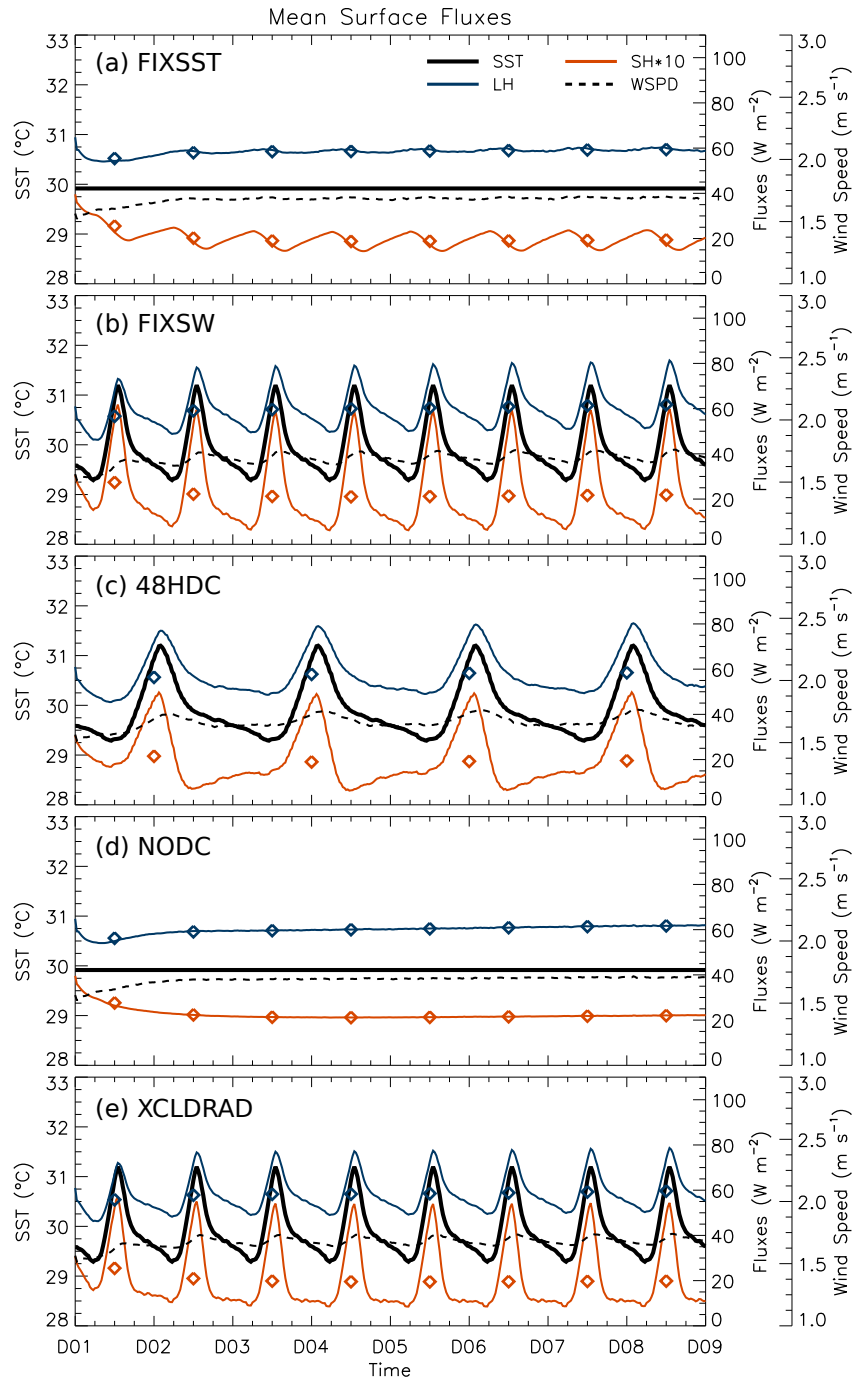


Fig. 3.18. As in Fig. 3.6 except for (a) FIXSST, (b) FIXSW, (c) 48HDC, (d) NODC, and (e) XCLDRAD.

from these comparisons is that, in this model framework, the diurnal cycle of surface fluxes, while important, is not the primary control of rainfall through the whole diurnal cycle.

$Q_1$  in FIXSST, 48HDC, and XCLDRAD is generally quite similar to that in CTL, with cooling between 2 and ~4.5 km that abates around midday as warming increases at low levels due to enhanced eddy flux convergence (Figs. 3.8a, 3.12a,c, and 3.19). (Note that in Fig. 3.19 and similar figures to follow, four days are used to display the same number of diurnal cycles in 48HDC.) Slightly less low-level warming is apparent in FIXSST than in CTL due to the reduced diurnal cycle in surface fluxes (Fig. 3.18a). The major discrepancy in  $Q_1$ , however, appears in the comparison between CTL, NODC, and FIXSW (Figs. 3.20a,b). NODC exhibits persistent cooling of a magnitude that resembles  $Q_1$  in CTL, if smoothed across the diurnal cycle.  $Q_1$  in FIXSW is similar to that in NODC, although the effects of midday PBL-rooted convection are apparent in midday low-level warming and enhanced evaporative cooling aloft (Figs. 3.16c and 3.18b). This low-level warming is weaker than in CTL, however, with SW fixed to its diurnal mean.

Given that  $Q_1$  in FIXSST, 48HDC, and XCLDRAD is similar to that in CTL, the diurnal variation in  $\theta'$  is also quite similar (Figs. 3.21a–c). NODC and FIXSW, however, exhibit very weak signals in  $\theta'$  relative to that in CTL (Figs. 3.22a,b). The very weak signal apparent in NODC between 3 and 4 km is related to a very weak trend in that simulation (discussed later). The signal in FIXSW is related to evaporative cooling driven by midday convection (Fig. 3.16c). The magnitude changes in  $\theta'$  in 48HDC are much larger than those in CTL (compare changes of ~0.3 K around 4 km in CTL to 0.6~0.7 K in 48HDC). This phenomenon can be understood as follows. The change in temperature  $\Delta T$  due to a given heating rate  $Q$  (i.e., that due to surface fluxes) can be calculated from  $\Delta T = Q\Delta t_{diurnal}$ , where  $\Delta t_{diurnal}$  is the duration of time relative to

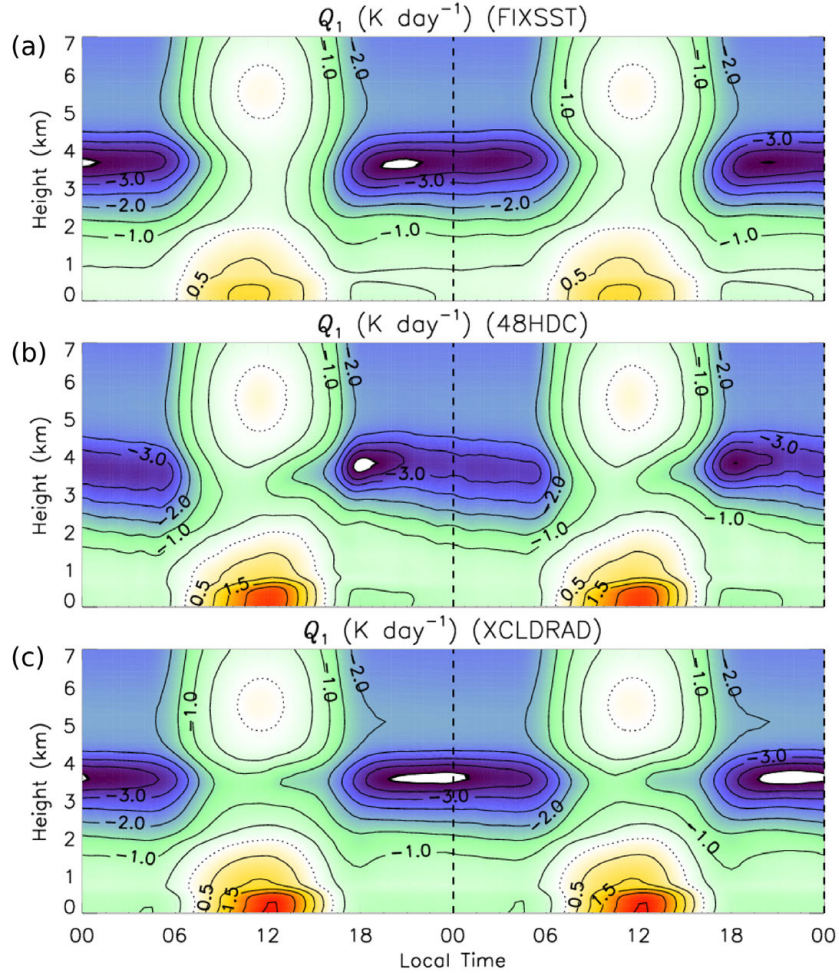


Fig. 3.19. As in Fig. 3.8, with  $Q_1$  ( $\text{K day}^{-1}$ ) for (a) FIXSST, (b) 48HDC, and (c) XCLDRAD.  $Q_1$  for 48HDC is displayed for D03 through D06 for better comparison with the other simulations.

the radiation or SST diurnal cycle – 48 h in 48HDC, and 24 h in CTL. For the case in which  $Q$  in 48HDC exactly equals that in CTL,  $\Delta T$  in 48HDC will be twice that in CTL due to the difference in  $\Delta t_{diurnal}$ . The differences in the  $\theta'$  signal within the cloud layer between 48HDC and CTL, however, also involve nonlinear feedbacks between the diurnal cycle and convection, as will be discussed section 3.4.C.

Similarly,  $q'$  in CTL compares quite closely in character with that in FIXSST, 48HDC, and XCLDRAD, although again the amplitude of that in 48HDC is much larger than in CTL

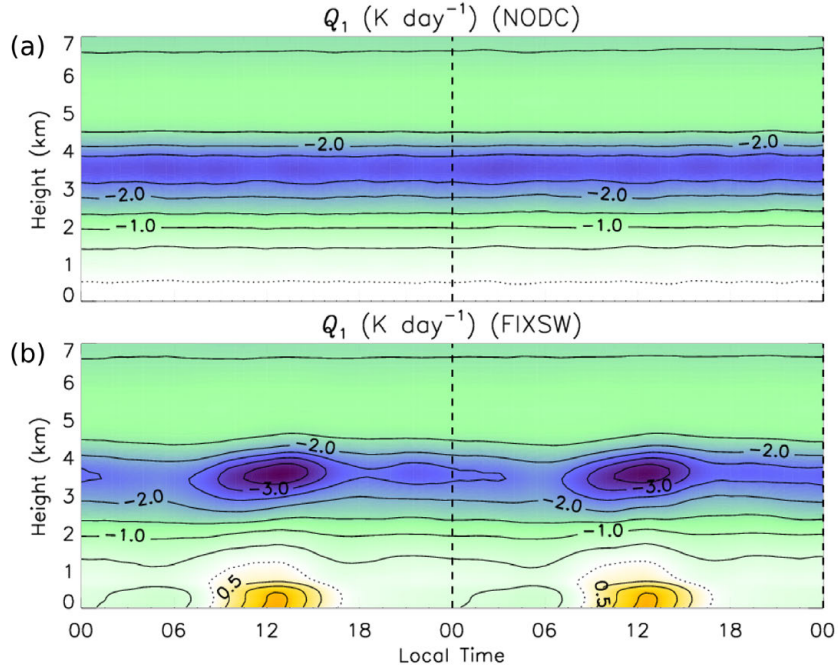


Fig. 3.20. As in Fig. 3.19 except for (a) NODC and (b) FIXSW.

(Figs. 3.23a–c).  $q'$  in FIXSST does not exhibit the PBL drying characteristic of CTL (48HDC and XCLDRAD do exhibit this feature), corroborating the role of midday increased SST and surface fluxes in driving eddies that scour PBL moisture and transport it aloft (Figs. 3.12a,c and 3.18a). That this PBL drying also appears in FIXSW supports this notion (Fig. 3.24b).  $q'$  in NODC exhibits no discernable signal, while that in FIXSW reflects the convective moistening by midday convection (Figs. 3.24a,b). While  $q'$  in CTL exhibits anomalies that extend throughout the lower troposphere, the  $q'$  anomalies in FIXSW are very localized to cloud top (Fig. 3.16c). This indicates that the diurnal variation of  $w_{wtg}$  associated with the diurnal cycle of SW is important to the column moisture budget.

Comparison of  $\langle \partial_t q \rangle$  between the simulations supports the notion that diurnal SW variation exerts major control over column moistening, given that CTL, 48HDC, FIXSST, and XCLDRAD exhibit large swings from daytime moistening to nocturnal drying, while FIXSW

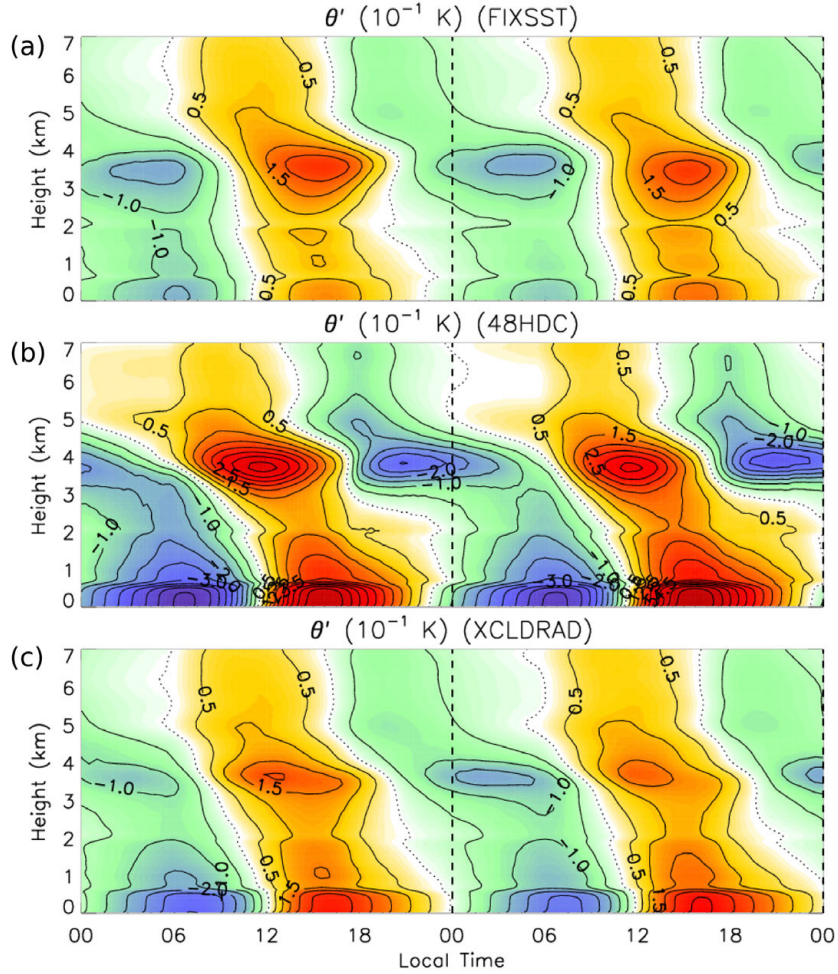


Fig. 3.21. As in Fig. 3.19 except for  $\theta'$  ( $CI = 0.5 \times 10^{-1}$  K).

and NODC do not (Fig. 3.25). The column tendencies are consistent with the respective diurnal cycles in  $q'$  (Figs. 3.23 and 3.24). That the amplitude of moistening and drying in 48HDC closely matches that in CTL is nontrivial, however, given that the respective signals in  $q'$  differ in magnitude substantially. As with  $\theta'$ , this discrepancy can be understood by considering the differing timescales over which  $\langle \partial_t q \rangle$  acts in CTL and 48HDC: with much greater positive area beneath the curve over the course of a given 48-h day in 48HDC than a given 24-h day in CTL, the associated net change in moisture is much larger in 48HDC than in CTL. That there is much

greater rainfall in 48HDC than in CTL likely owes to this greater cumulative moistening, which is evident in the amplitude of  $q'$  (Figs. 3.17 and 3.23b).

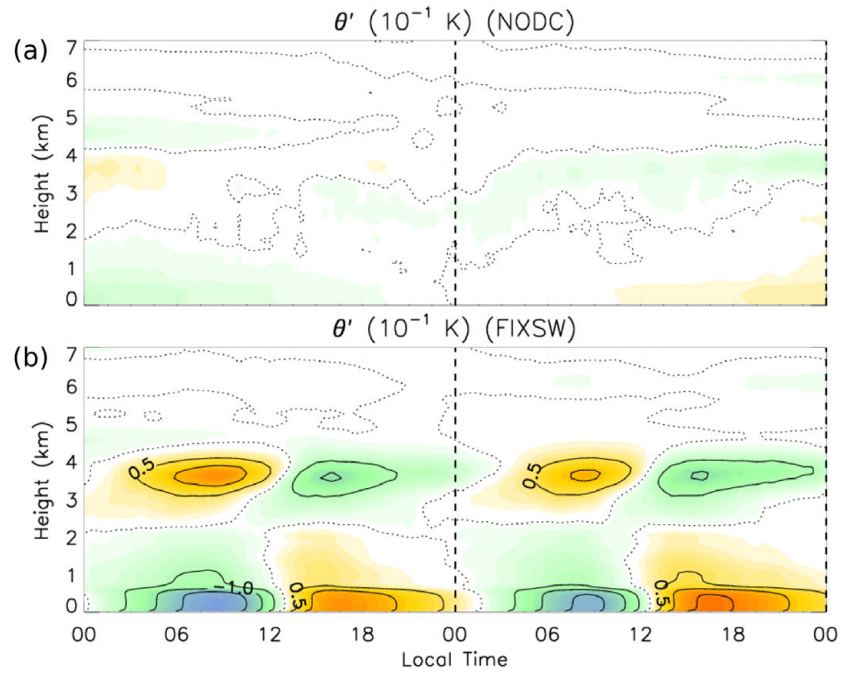


Fig. 3.22. As in Fig. 3.21 except for (a) NODC and (b) FIXSW.

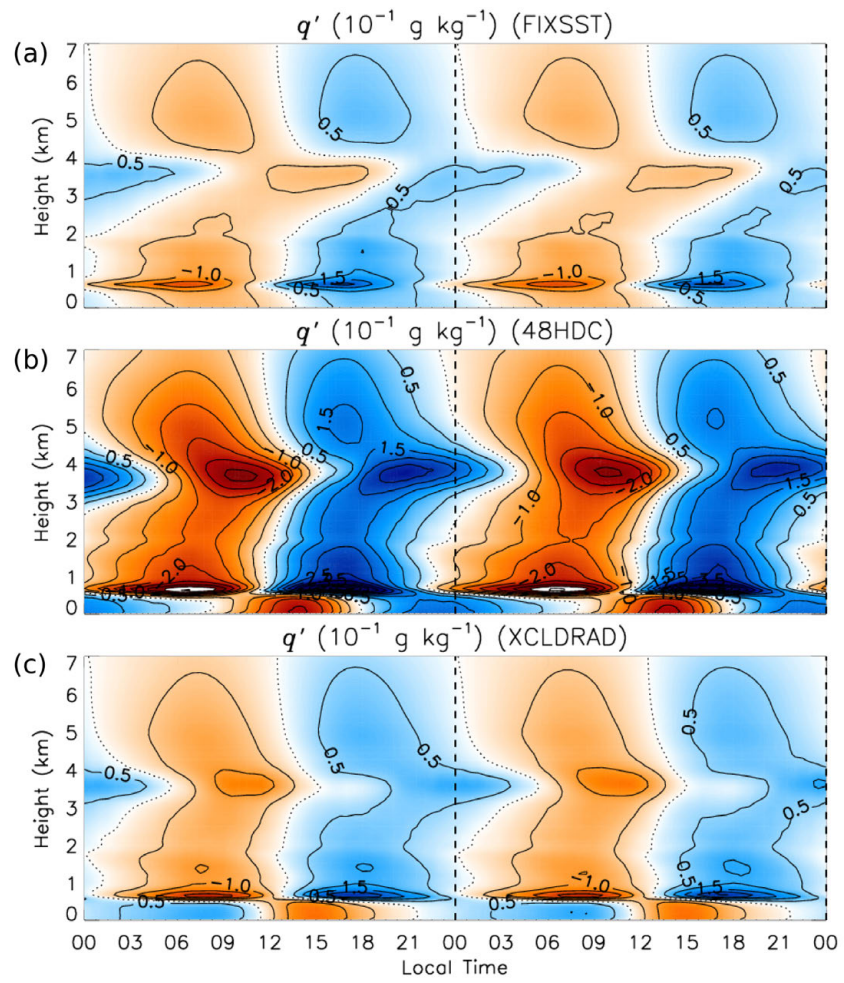


Fig. 3.23. As in Fig. 3.19 except for  $q'$  ( $\text{CI} = 10^{-1} \text{ g kg}^{-1}$ ).

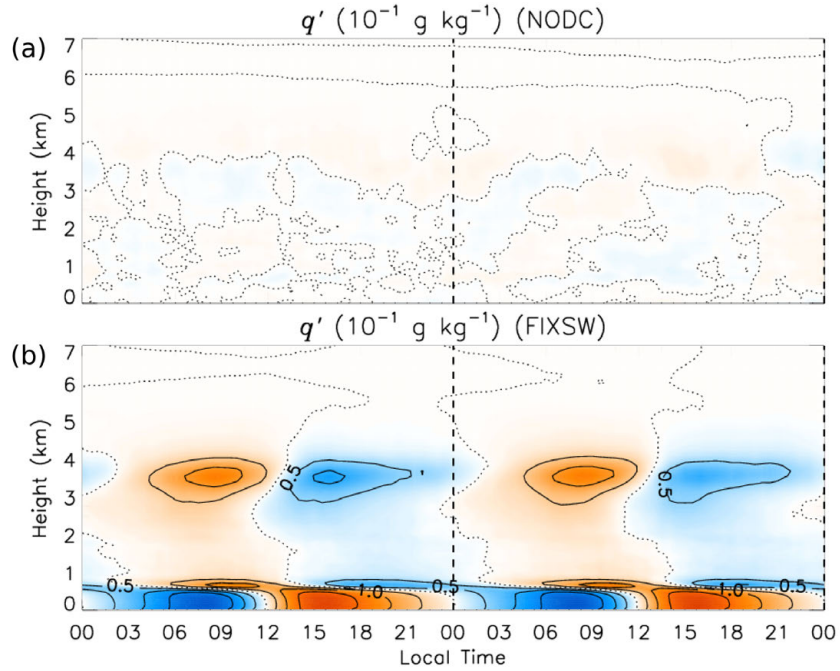


Fig. 3.24. As in Fig. 3.23 except for (a) NODC and (b) FIXSW.

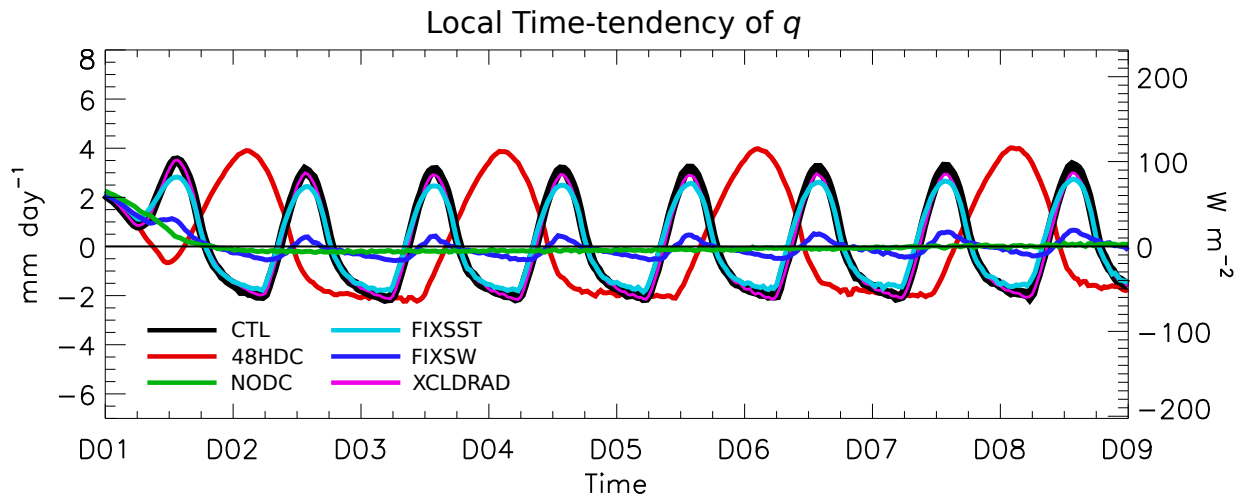


Fig. 3.25. Time series of the domain-averaged and  $\langle \partial_t q \rangle$  (mm day $^{-1}$  along the left ordinate; W m $^{-2}$  along the right) for all simulations according to the legend.

### C) THE DIURNAL CYCLE AND COLUMN MOISTENING

The time series of rainfall rate provides evidence of model drift, with rainfall in many of the simulations increasing with time, despite the moisture budget being in near-perfect balance (Figs. 3.17 and 3.25). A time series showing precipitable water PW (i.e.,  $\langle q \rangle$ ) for all of the simulations (along with a new simulation, 48HDC\_NOON, described below) and rainfall out to 16 days for select simulations confirms that the moisture budget is out of balance, with precipitable water changing from day to day (Fig. 3.26). As PW increases over 16 days in 48HDC\_NOON and NODC, rainfall dramatically increases, reflecting a transition to deep convection in the domain (not shown). Rainfall in XCLDRAD also increases with time, though the deep-convective transition is evidently not reached by day 17. Differences in the day-to-day moistening rates indicate that the measure of moisture imbalance varies among the simulations. All of the curves exhibit an increasing trend with time, although those with a diurnal cycle in SW increase more rapidly than those without.

48HDC\_NOON has not been previously discussed. This simulation is identical to 48HDC, except with the diurnal cycle of SST and radiation initialized at local noon rather than midnight, which has the effect of reducing the net moistening on the first day relative to the other simulations (Fig. 3.26). Executed following discovery of the trends shown in Fig. 3.26, this simulation is designed specifically to rule out the possibility that the differences in first-day moistening explain the differences in PW trends. Given that the PW trend in 48HDC\_NOON increases more rapidly than that in the other simulations (though similar to that in 48HDC), the aforementioned possibility is nullified, thus confirming that there is a feedback related to the diurnal cycle, which is amplified in 48HDC and 48HDC\_NOON.

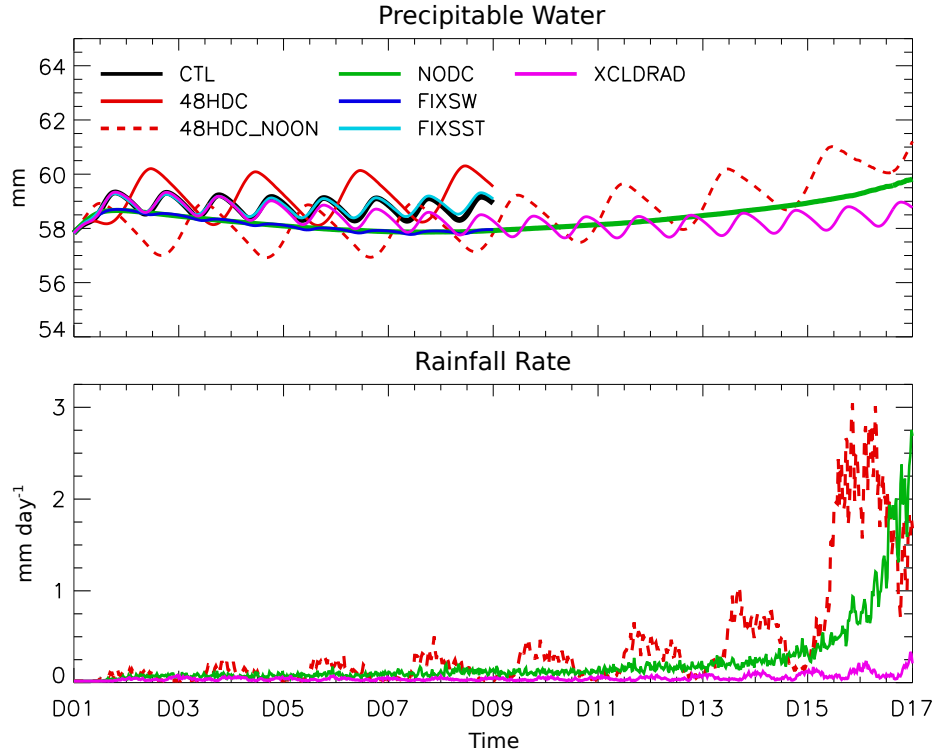


Fig. 3.26. Time series of (top) domain-averaged precipitable water PW (mm) for all simulations, and (bottom) rainfall rate (mm day<sup>-1</sup>) for 48HDC\_NOON, NODC, and XCLDRAD.

The difference between 48HDC and the other simulations that leads to the differing moistening trends is revealed by a comparison of  $Q_c$  from the respective simulations (Fig. 3.27). The evaporative cooling in the upper cloud layer in 48HDC is subtly weaker than that in all of the other simulations (Figs. 3.27a–d). This difference is most apparent overnight–early morning. Furthermore, condensation heating in 48HDC is slightly greater from 1~2.5 km than in the other simulations. This difference is more clearly visualized in eight-day mean vertical profiles of  $Q_c$  (Fig. 3.28). In particular,  $Q_c$  in 48HDC is up to  $\sim 0.5$  K day<sup>-1</sup> greater than that in NODC around 3.5 km, which accounts for a corresponding positive difference in  $w_{wtg}$  of  $\sim 0.5$  mm s<sup>-1</sup>. Therefore, there is weaker subsidence, and hence weaker drying in the cloud layer due to the stretched diurnal cycle in 48HDC relative to NODC. The difference of  $0.5$  mm s<sup>-1</sup> equates to 7.7% of the diurnal peak magnitude of subsidence in this layer in CTL. The weaker mean

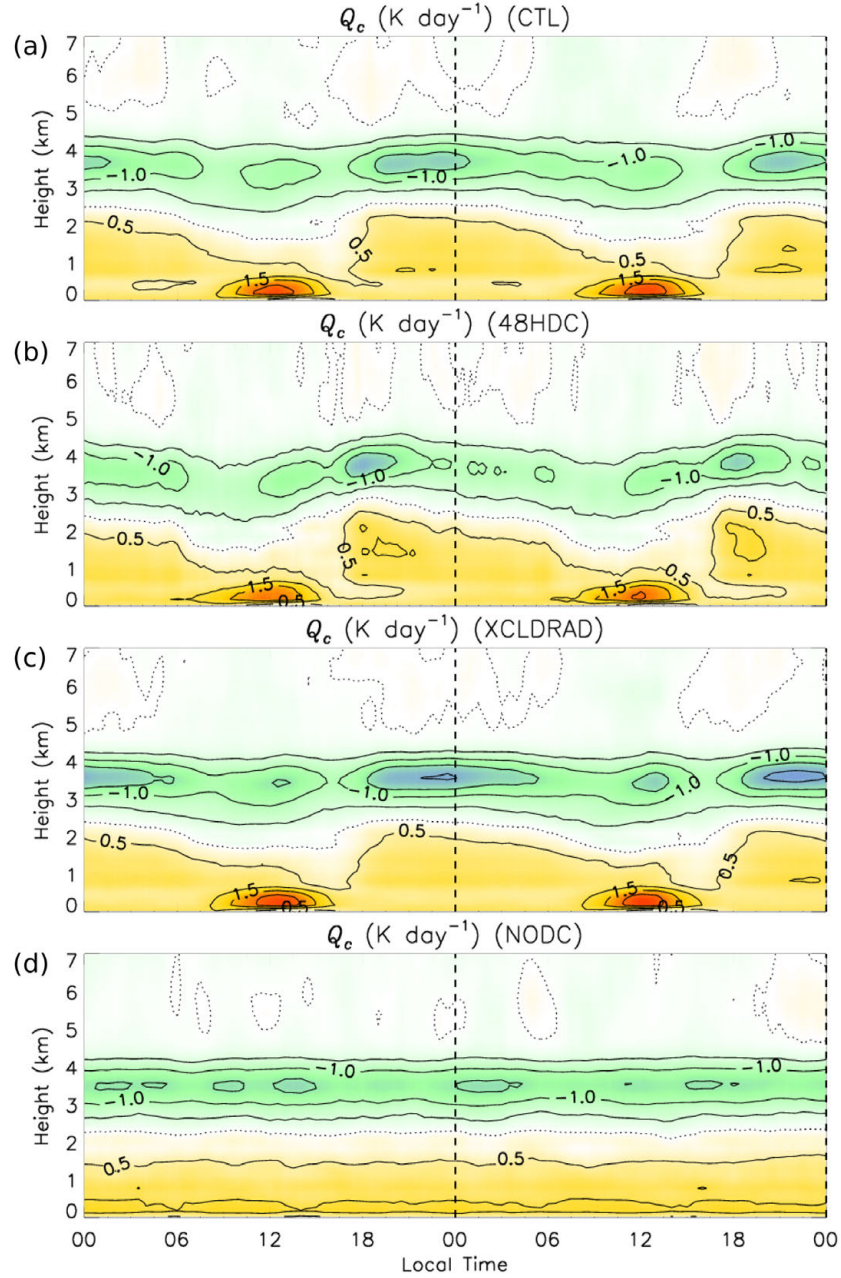


Fig. 3.27. As in Fig. 3.19 except for  $Q_c$  for (a) CTL, (b) 48HDC, (c) XCLDRAD, and (d) NODC ( $CI = 0.5 \text{ K day}^{-1}$ ).

subsidence in 48HDC (and in 48HDC\_NOON; not shown) explains the increased rate of moistening relative to the other simulations (Fig. 3.26). Since this difference is rectified by the diurnal cycle, however, mean profiles cannot explain the key physics at play.

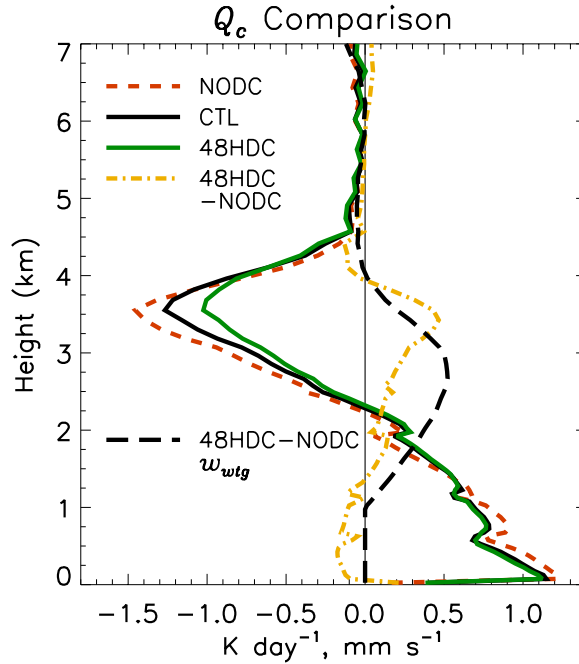


Fig. 3.28. Domain- and time-mean vertical profiles of  $Q_c$  ( $\text{K day}^{-1}$ ) in NODC (red dashed), CTL (black solid), and 48HDC (green solid), the difference between that in 48HDC and that in NODC (yellow dash-dotted), and the difference between  $w_{wtg}$  ( $\text{mm s}^{-1}$ ) in 48HDC and that in NODC (black dashed). Data were averaged from D01 through D09.

With the diurnal cycles of rainfall and PW in CTL and 48HDC lined up local time, it becomes clear that rainfall initiates earlier in the evening and is more intense in 48HDC than in CTL (Fig. 3.29a). This apparent phase shift in rainfall relates to the phase shift in the diurnal cycle of temperature, as indicated by the difference between  $\theta'$  in 48HDC from that in CTL (Fig. 3.29b) (see also Fig. 3.21). The positive values in the PBL owe the greater duration over which enhanced daytime surface fluxes warm the PBL in 48HDC, as described earlier. By similar reasoning, the warm anomaly in the upper cloud layer that peaks at  $\sim 3.5$  km is associated with greater *relative* warming by SW in 48HDC than in CTL. At this level, however,  $w_{wtg}$  operates to offset temperature anomalies.

Recall that  $w_{wtg}$  operates to offset domain-averaged  $\theta$  anomalies (i.e., deviations from  $\theta_0$ ) with an adjustment timescale  $\tau_j$  (3.6) that varies as a function of vertical mode only (assuming  $N$

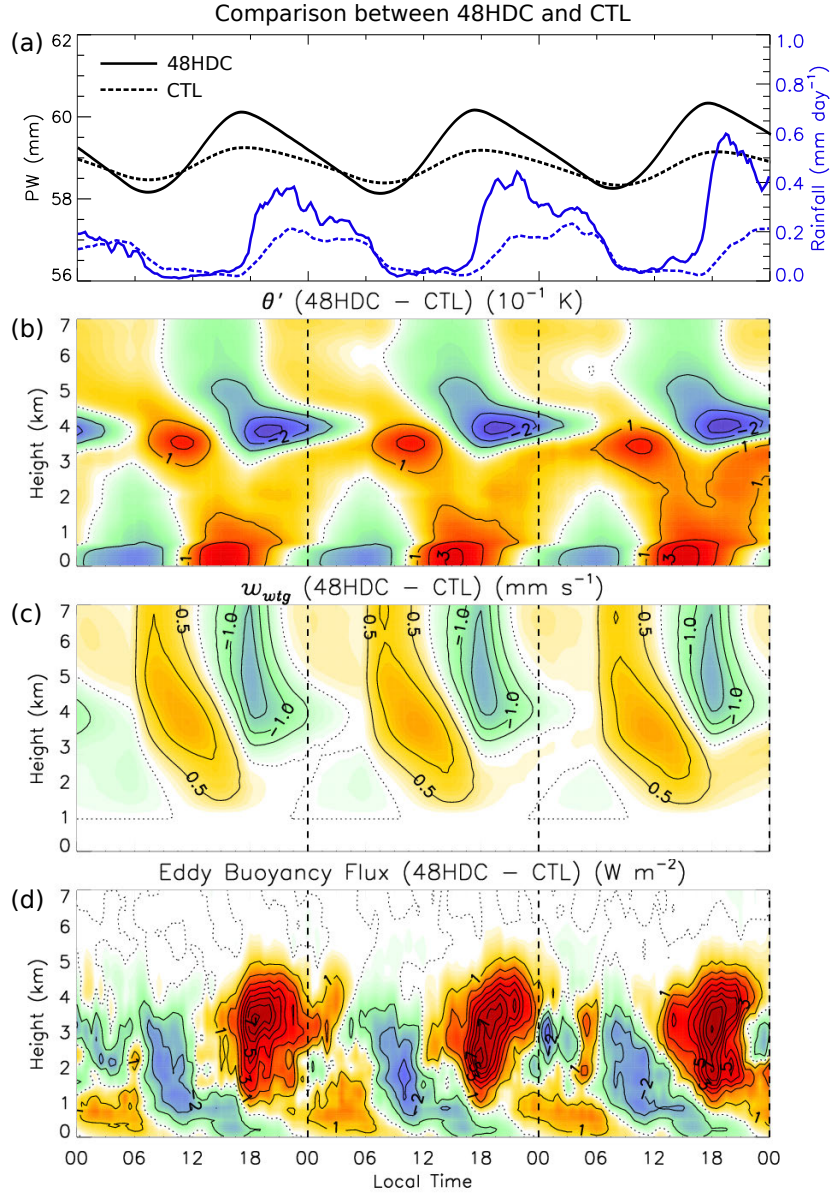


Fig. 3.29. Time series of (a) PW (black; mm; left ordinate) and rainfall rate (blue; mm day<sup>-1</sup>; right ordinate) in 48HDC (solid) and CTL (dashed), (b) the difference between  $\theta'$  in 48HDC and that in CTL (CI =  $10^{-1}$  K), (c) the difference between  $w_{wtg}$  in 48HDC and that in CTL (CI =  $0.5 \text{ mm s}^{-1}$ ), and (d) the difference between vertical eddy buoyancy flux in 48HDC and that in CTL (CI =  $1 \text{ W m}^{-2}$ ). The period D03–D05 (inclusive) is used for the time series of CTL, and the period D03–D08 is used for that of 48HDC.

does not change). Therefore, since  $\tau_j$  is the same in 48HDC as in CTL, this adjustment timescale is more rapid relative to the diurnal cycle in 48HDC than it is in CTL. This timescale difference explains the greater daytime ascent in  $w_{wtg}$  in 48HDC, which is in response to the greater relative

warming due to  $Q_R$  (Fig. 3.29c). This relative warm  $\theta'$  in 48HDC explains why clouds are slightly shallower in the late morning compared to CTL (Fig. 3.16d). In connection with greater relative rising motion in 48HDC, the column is moistened more than in CTL, as indicated by the diurnal cycle in PW (Fig. 3.29a). As  $Q_R$  decreases in the afternoon with the shutdown of SW, temperature in 48HDC responds more quickly relative to the diurnal cycle compared to CTL, explaining the negative relative anomaly in  $\theta'$  at 4 km, which is tied to the greater relative subsidence that appears around the same time (see also Fig. 3.21). While this cold relative  $\theta'$  anomaly is due to the more rapid radiative cooling in 48HDC relative to CTL, convection is also important.

The difference between vertical eddy buoyancy flux in 48HDC from that in CTL indicates much greater convection relative to CTL beginning at  $\sim 1800L$ , consistent with greater rainfall at this time (Fig. 3.29d). This convective burst in 48HDC relates in part to the more rapid relative cooling response to the shutdown of SW; however, it likely also relates to the more moist conditions established by greater relative daytime ascent in  $w_{wtg}$ , as indicated by PW (Fig. 3.29a). But why, then, is the overall evaporative cooling of the upper cloud layer weaker, if convection is in fact stronger (Fig. 3.27b)? Evening–nocturnal convection is indeed stronger in 48HDC, as corroborated both by greater  $Q_c$  heating and greater vertical eddy buoyancy flux in the evening in 48HDC.

The key result of the larger diurnal cycle of  $w_{wtg}$  in 48HDC is that the lower troposphere is moistened more during the day than in CTL, both by greater (relative) ascent and more vigorous evening convection (Figs. 3.29a,c,d). Since  $q'$  and  $\theta'$  are anti-correlated in the upper cloud layer (Figs. 3.21b and 3.23b), the associated diurnal cycle in RH is greater than that in either  $q'$  or  $\theta'$  due to the effect both anomalies. Then, since the diurnal amplitude of both  $q'$  and

$\theta'$  is much greater in 48HDC than in CTL, the associated signal in  $RH'$  in 48HDC is much larger than that in CTL (Figs. 3.30a,b). The key result is that the amount of evaporation that will occur in the evening and overnight when RH is at its highest is less in 48HDC than in CTL. This difference in the magnitude of  $RH'$  is what causes the difference in  $Q_c$ , and hence the more rapid moistening in 48HDC (and 48HDC\_NOON) than in CTL (Fig. 3.26).

By extrapolation, it can be reasoned that the above-described nonlinear diurnal rectification process accounts for the other differences in the PW trends (Fig. 3.26). That in XCLDRAD, however, is less intuitive, as this simulation is characterized by a very similar diurnal cycle to that in CTL, yet it is characterized by a weaker moistening trend than that of NODC (Figs. 3.8a, 3.19c, and 3.30a,c). Comparing  $Q_c$  in CTL with that in XCLDRAD reveals notably stronger cooling of the upper cloud layer, suggesting that there is relatively greater  $w_{wtg}$  subsidence and hence drying than in CTL.

Recall that the only difference between CTL and XCLDRAD is that clouds are non-interactive with radiation in the latter. To demonstrate the effect that this has on individual clouds (in CTL), consider the difference between LW at cloudy points (i.e., grid columns where  $q_c + q_i \geq 0.5 \text{ g kg}^{-1}$ ) and the domain-averaged LW, and the respective difference for SW (Fig. 3.31). This difference highlights three important aspects of cloud–radiative feedbacks: 1) the clouds cause a relative warming of the air beneath them in the longwave bands; 2) they strongly cool from their tops in the longwave bands; and 3) they have virtually the opposite effect (though much more weakly so) in shortwave bands. The net result is that the cloudy columns are destabilized, and hence convect more vigorously, when they are radiatively active. The removal of this cloud–radiative feedback in XCLDRAD shuts down rainfall, which indicates that less

water is removed from the column (Fig. 3.17). This relative excess of water in the relatively less vigorous clouds instead evaporates, leading to enhanced  $Q_c$  cooling.

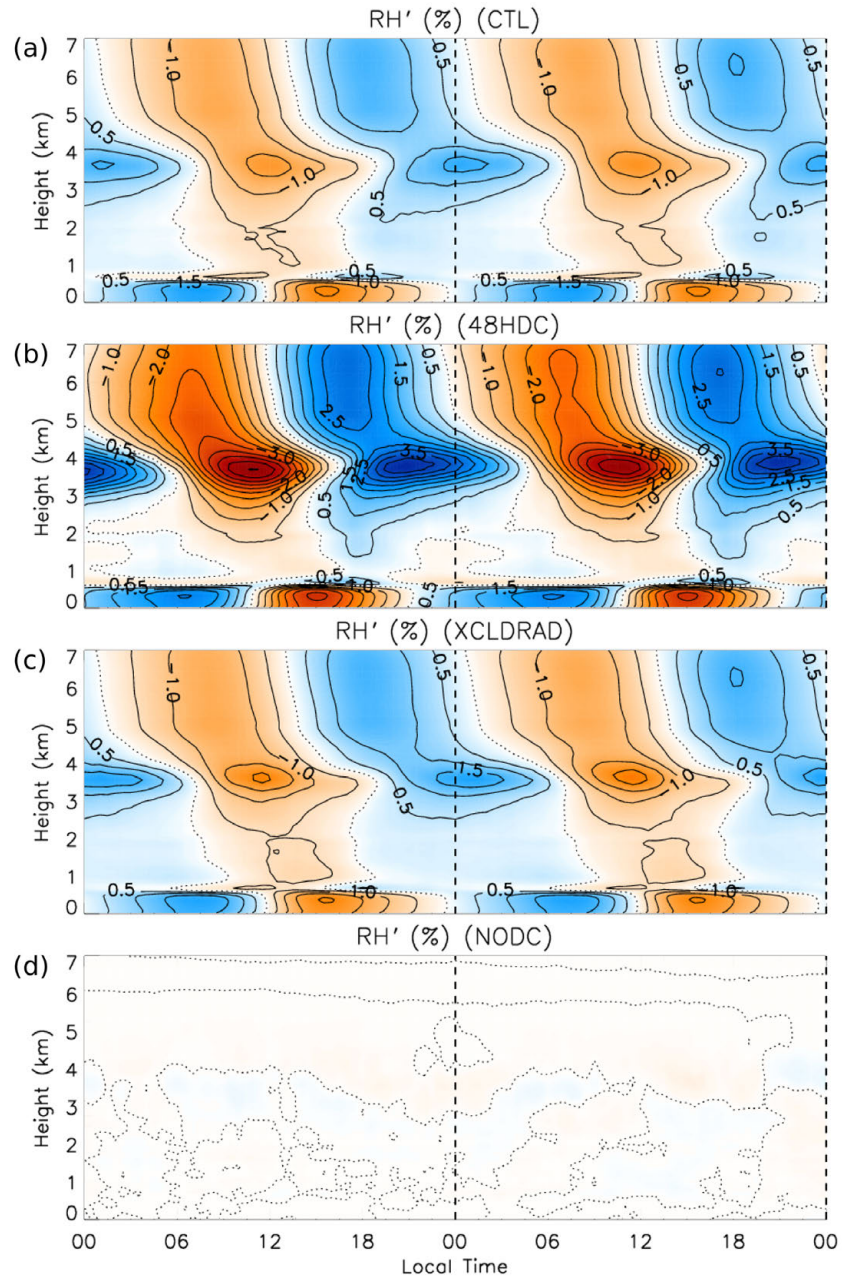


Fig. 3.30. As in Fig. 3.19 except for  $RH'$  (i.e.,  $RH$  with diurnal mean removed) for (a) CTL, (b) 48HDC, (c) XCLDRAD, and (d) NODC ( $CI = 0.5\%$ ).

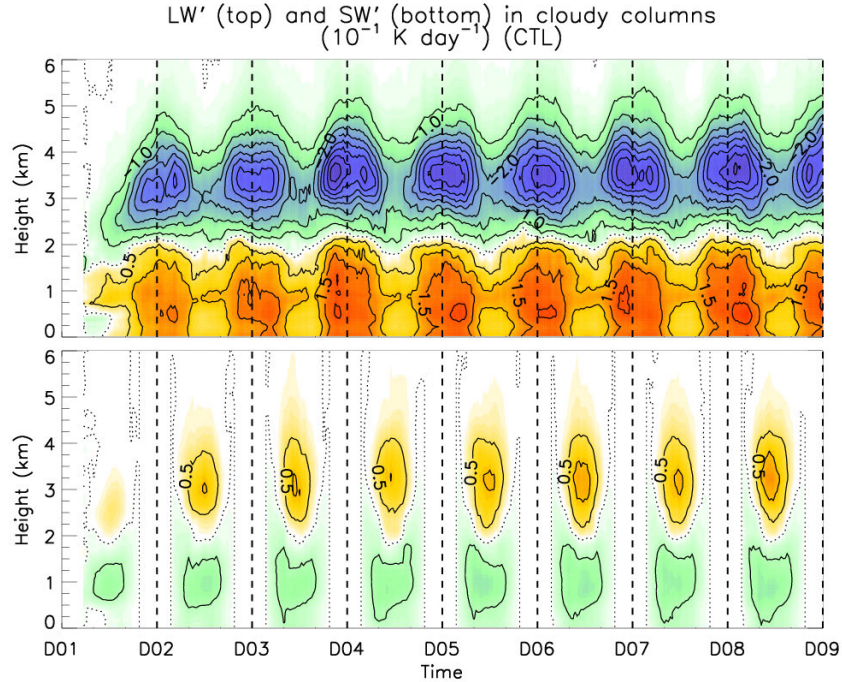


Fig. 3.31. Time–height series of the mean difference between (top) LW and (bottom) SW in cloudy regions (i.e., grid columns where  $q_c + q_i \geq 0.5 \text{ g kg}^{-1}$ ) and the respective all-inclusive domain-averaged values in CTL ( $CI = 10^{-1} \text{ K day}^{-1}$ ).

#### D) SENSITIVITY TESTS

Two additional sensitivity tests have been carried out independent of the modified physics tests described in the previous section. These two tests represent the first step toward grasping the sensitivity of trade-cumulus convection with imposed spectral WTG forcing to grid resolution and microphysics. Both simulations are identical to CTL, though only integrated out to four days, and with the following modifications: in LORES, spacing in the horizontal dimensions is 400 m (i.e., twice the value of that in CTL); and in SINGMOM, the NASA–Goddard single-moment microphysics scheme, based on Lin et al. (1983), is employed in place of the Morrison double-moment scheme.

LORES exhibits a clear, immediate drift with rainfall increasing rapidly each day to  $>1 \text{ mm day}^{-1}$  by the simulation end and clouds quickly deepening to  $\sim 6\text{-km}$  depth (Figs. 3.32a,b).

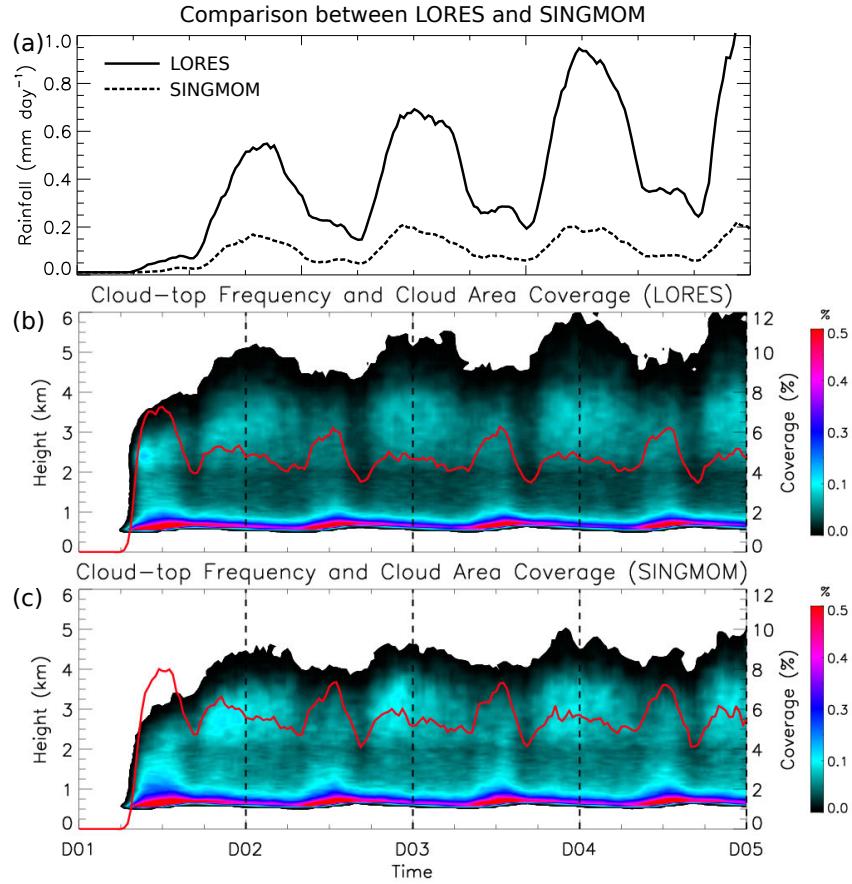


Fig. 3.32. Time series of (a) rainfall rate ( $\text{mm day}^{-1}$ ), with LORES (solid) and SINGMOM (dashed), and time–height series of cloud-top frequency and cloud area coverage for (b) LORES and (c) SINGMOM.

SINGMOM, in contrast, closely matches CTL in rainfall rate, its diurnal cycle, and cloud depth, with no detectable drift (Figs. 3.4, 3.5, and 3.28c). Comparison of  $Q_c$  between CTL and LORES provides clear evidence as to the cause of the drift: in LORES, there is very weak evaporative cooling of the upper cloud layer relative to CTL, and in fact warming in this layer by late in the simulation (Figs. 3.27a and 3.32a). Weaker cooling implies weaker subsidence in  $w_{wtg}$ , which in turn implies a weaker subsidence-driven moisture sink. Since the same prescribed moisture source is applied as that which keeps the moisture budget balanced in CTL, the budget in LORES is unbalanced, the column moistens, and hence convection rapidly deepens. It is likely

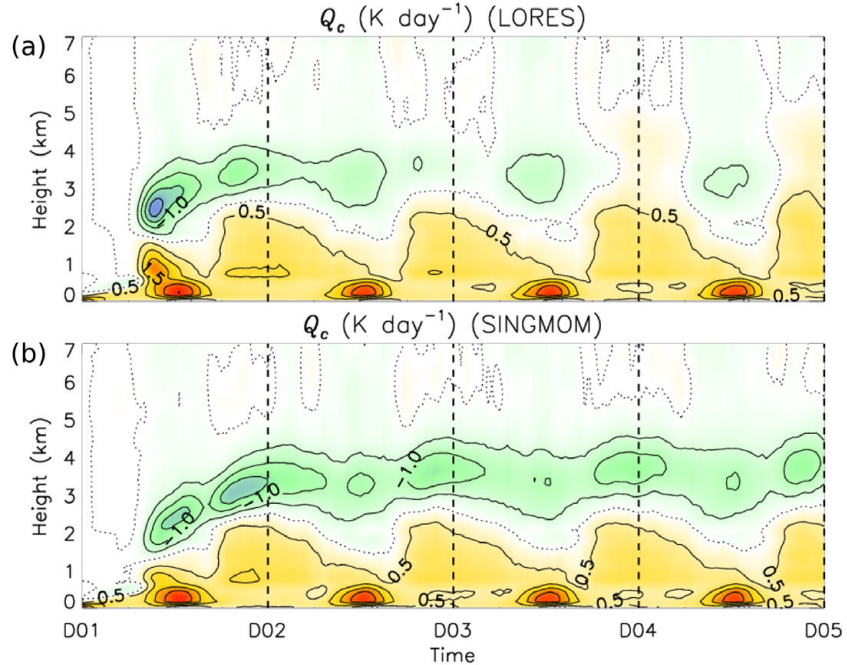


Fig. 3.33. Time–height series of  $Q_c$  ( $CI = 0.5 \text{ K day}^{-1}$ ) for (a) LORES and (b) SINGMOM.

that, relative to LORES, the finer grid spacing in CTL enables better representation of the cloud-scale circulations responsible for dry-air entrainment and cloud water detrainment, ultimately leading to greater evaporation in CTL than in LORES. Without more similar sensitivity tests, however, it is unclear how small the grid spacing must be before this cloud evaporation sensitivity is reduced.

Although the cloud-layer evaporative cooling in  $Q_c$  is also slightly less in SINGMOM than in CTL, there is no apparent drift as there is in LORES (Figs. 3.32b and 3.33b). That SINGMOM spans only four days, however, limits the ability to fully compare possible drift in this simulation with that in CTL. It is encouraging, nevertheless, that SINGMOM and the first four days in CTL are quite consistent in rainfall and cloud characteristics.

### 3.5 Summary and conclusions

The present study describes a suite of modeling tests that have been carried out in order to 1) better understand the relative roles of SST and radiative heating in the diurnal cycle of moist convection under large-scale suppressed conditions, and 2) test the hypothesis that the diurnal cycle causes greater net column moistening from day to day than would occur without the diurnal cycle, which derives from the observational findings presented in chapter 2. To carry out these tests, a cloud model (CM1; Bryan and Fritsch 2002) has been employed with moist convection explicitly represented, a diurnal cycle of SST prescribed, and cloud-interactive radiation simulated with a diurnal cycle in shortwave heating (SW). The effects of large-scale subsidence ( $w_{wtg}$ ) are parameterized in the model via the spectral WTG technique, wherein domain-mean temperature deviations are opposed by adiabatic motion applied with a vertical-mode-dependent relaxation timescale (Herman and Raymond 2014; section 3.2). A constant prescribed moisture source is applied such that the simulations remain in a quasi-steady state for over a week's simulation time.

The control simulation (CTL) represents the primary characteristics of the observed diurnal cycle adequately – with nocturnally enhanced subsidence, distinct daytime and nocturnal convective regimes with associated peaks in cloud depth, and daytime (nocturnal) mixed layer deepening (shoaling) (Johnson et al. 2001). The afternoon peak in rainfall is much weaker than that in observations; the daytime response of convection to enhanced surface fluxes, however, is very similar to that in observations.

The midday peak in PBL-rooted, mostly non-raining convection in CTL is caused by enhanced surface fluxes, which in turn depend on the diurnal cycle of SST. The observed diurnal cycle of surface wind speed (of  $\sim 2 \text{ m s}^{-1}$ ) is not well represented by CTL, such that the

diurnal amplitude of surface flux variations may also be underrepresented. Though it is yet unclear, this weakness may owe to too coarse of a model grid for properly resolving PBL thermals.

Consistent with previous studies, the diurnal cycle in shortwave heating supports more vigorous nocturnal convection (Randall et al. 1991). The diurnal cycle of SW acts to suppress daytime convection via a large, positive residual between radiative cooling and subsidence warming (i.e.,  $Q_{resid} = w_{wtg} \partial_z \bar{\theta}$ ) during the day.  $Q_{resid}$  is large in the morning owing to the combination of persistent  $w_{wtg}$  subsidence warming – established by enhanced nocturnal evaporative cooling – and rapidly increasing SW, which leads to the development of a warm anomaly in the upper cloud layer, thereby stabilizing that layer. During the evening,  $Q_{resid}$  decreases as a result of relaxed  $w_{wtg}$  subsidence (or weak ascent), which in turn is in response to the aforementioned warm anomaly. As SW then shuts off around 1800L,  $Q_{resid}$  reaches a minimum, thereby favoring the intensification of convection into the night as evaporative cooling in the upper cloud layer then destabilizes the cloud layer.

A key finding from CTL is that the diurnal cycle in  $w_{wtg}$  exerts a dominant control over the column moisture budget by “throttling” the moisture sink due to subsidence. Since radiative heating largely controls the variation in  $w_{wtg}$ , it is clear that SW plays a critical role in the diurnal modulation of column moisture. Exclusion of the diurnal cycle in SW virtually removes nocturnal rainfall. Complementary to this finding is the surprising finding that, in the context of column diurnal humidity variations, the diurnal cycle of SST and the associated diurnal cycle of surface fluxes is of little importance relative to that in SW. This finding suggests that Hypothesis 1 of chapter 2 is nullified; however, since the diurnal cycle of surface wind speed is

not well represented in the model, a conclusion that the diurnal cycle of SST is unimportant to diurnal column moisture variations should be drawn with some caution.

The difference between CTL and 48HDC – identical to CTL but with a diurnal cycle of 48 h – is manifest in amplitude differences in the diurnal cycle. Specifically, 48HDC exhibits  $\geq$ twice the magnitude signals in  $\theta'$  and  $q'$  in the PBL and upper part of the cloud layer. These differences cannot be explained by differences in the magnitude of the forcing – i.e., that due to surface fluxes or radiative heating rates – since these tendencies do not substantially differ between the two simulations. The only explanation, therefore, is the timescale over which the tendencies operate relative to the timescale of the diurnal cycle. With a tendency of similar magnitude acting over differing durations of time (i.e., compare 24 h in CTL to 48 h in 48HDC), the heating/cooling and moistening/drying driven by that tendency will occur more rapidly *relative to the diurnal cycle*, and to larger extent, in 48HDC than in CTL. Therefore, nocturnal convection triggers slightly earlier and with more vigor in 48HDC relative to CTL.

Given that diurnal  $\theta$  and  $q$  variations closely anti-correlate in the upper cloud layer since adiabatic motions and evaporative cooling and moistening are their driving processes, the associated relative humidity anomaly  $RH'$  is larger than either that in  $\theta$  or  $q$ . Therefore, in the case of 48HDC, the diurnal cycle of  $RH'$  is much larger than that in CTL. The result of this discrepancy is that less nocturnal evaporative cooling and moistening can take place in the upper cloud layer in 48HDC relative to CTL, since this evaporation occurs nocturnally when  $RH'$  peaks. This leads to less daily-mean evaporative cooling of the upper cloud layer in 48HDC than in CTL, and hence, via  $w_{wtg}$ , less subsidence drying. This nonlinear feedback, which evidently depends on the diurnal variation of SW, explains the greater apparent day-to-day moistening trend in 48HDC relative to CTL. This feedback is emphasized even more by comparison of the

moisture trend in 48HDC with that in NODC, as well as that in the other simulations wherein the diurnal cycle of SW is excluded.

Given that the diurnal cycle is characterized by a feedback that rectifies moistening onto longer timescales, Hypothesis 1 of chapter 2 – though incorrect in the attribution to the diurnal cycle of SST and surface fluxes – is correct to the extent that the diurnal cycle must be considered a daily-mean column moisture source, without which the tropical climate would be in a slightly different state. Furthermore, given this feedback, it cannot be ruled out that the diurnal cycle is a critical part of the moistening that takes place during MJO initiation as moist convective clouds first deepen and organize on the large scale.

## CHAPTER 4

### OVERARCHING CONCLUSIONS

In this dissertation, both observations and modeling techniques have been exploited to explore the possible role of the diurnal cycle in large-scale climate. In chapter 2, observations from DYNAMO were employed to 1) diagnose the general character of the two observed MJO events, and 2) to characterize the diurnal cycle of moist convection, and its relationship with column humidity. The observations demonstrate that MJO onset takes place as follows: moistening of the low–midtroposphere is accomplished by cumuliform clouds, which deepen as the drying by large-scale subsidence and horizontal advection simultaneously wane. This relaxing of subsidence is tied to decreasing column radiative cooling, which links to the evolution of the cloud population.

Description of the diurnal cycle reveals the high degree to which clouds and column humidity are linked at this timescale. This diurnal cycle is driven by the diurnal cycles in SST, air-sea fluxes, and radiative fluxes, which are especially large in the suppressed phase (or pre-onset stage) of the MJO. The diurnally modulated cloud field exhibits pronounced mesoscale organization in the form of open cells and horizontal convective rolls. These observational findings motivated two new hypotheses, which posit that the diurnal cycle and mesoscale cloud organization may promote more vigorous day-to-day tropospheric moistening than would otherwise occur.

The modeling study described in chapter 3 is designed specifically to 1) test the hypothesis that the diurnal cycle drives day-to-day moistening of the column, and 2) better understand the relative roles of SST and radiation in the diurnal cycle of convection. In the

model, moist convection is explicitly represented, with the diurnal cycle of SST prescribed, and cloud-interactive radiation simulated with a diurnal cycle in shortwave heating. The large-scale dynamics are parameterized via the spectral weak temperature gradient (WTG) technique of Herman and Raymond, wherein external (i.e., “large-scale”) vertical motion is diagnosed based on the internal diabatic heating in the model, which is then used to advect model temperature and humidity. This vertical motion opposes the domain-averaged diabatic warming/cooling via adiabatic warming and cooling, and strikes a feedback between the model diabatic heat sources and humidity.

With a control simulation that successfully replicates quite well the regime of shallow convection that occurs in nature, it is found through sensitivity tests that the diurnal cycle in shortwave radiative heating (SW) is the dominant driver of both diurnal column moisture variations and nocturnal rainfall in this regime, the latter of which agrees with previous findings by Randall et al. The diurnal cycle in SST and surface fluxes, in turn, is the main driver of the daytime convective regime, which is distinct from the nocturnal regime by its rooting in the boundary layer.

Although the representation of distinct daytime and nocturnal convective regimes in the model is consistent with observations, rainfall in the simulations is notably weaker. The possibility that the simulated radiative cooling is stronger than in nature, thereby causing a stronger column moisture sink, is currently being explored. It is possible that diurnal pumping of the Hadley circulation tied to diurnal fluctuations of ITCZ convection exerts impacts on the DYNAMO observations described herein, as speculated in chapter 2. These effects would not, however, be captured in the model.

A key finding from the modeling study is that the diurnal cycle of SST and surface fluxes – hypothesized to potentially be important to climate in chapter 2 – is of little–no importance in the context of the column moisture budget, which is instead primarily modulated by the diurnal cycle of SW. An issue with generalizing this finding, however, is that the model does not well-represent the full magnitude of the diurnal cycle in surface wind speed as it occurs in nature, thereby potentially underrepresenting the magnitude of diurnal variations of surface fluxes.

A simulation in which the diurnal cycle is stretched to 48 h reveals an important nonlinear feedback at work in the diurnal cycle, which owes to the high-amplitude diurnal cycle in column relative humidity RH. This diurnal cycle in RH limits the amount of evaporation, and hence evaporative cooling, that can take place nocturnally in the upper part of the cloud layer. By throttling down the diabatic cooling, this diurnal cycle in RH throttles down the daily-mean moisture sink driven by large-scale subsidence, such that the environment drifts more rapidly toward a moist state relative to CTL and the other simulations, especially those in which the diurnal cycle of SW is excluded.

Studies show that the diurnal cycle of SST in the tropics is critical to rectifying the slower (i.e., daily-mean) SST increases observed during the suppressed phase of the MJO (Webster et al. 1996; Duvel et al. 2004; Bernie et al. 2005, 2008; Vialard et al. 2009; Matthews et al. 2014). With the findings presented herein, we now have evidence that a similar process exists in the atmosphere, whereby the diurnal pumping of shallow convection and associated diurnal moistening rectifies onto longer timescales, leading the environment to drift toward a moister state. This supports a hypothesis presented in chapter 2, that the diurnal cycle exerts a day-to-day moistening that would not otherwise occur. It is therefore clear that proper representation

of the diurnal cycle of moist convection is crucial for accurate representation of large-scale tropical climate.

Future work is needed to test another hypothesis that was presented in chapter 2 – that the observed mesoscale organization of clouds leads to greater day-to-day moistening than would otherwise occur. This may require a larger modeling domain, as the scale of the observed organization reaches as large as ~50 km, i.e., similar to the total length of the meridional dimension in the modeling study described herein.

More testing of the key hypothesis of this study – that the diurnal cycle rectifies moistening onto longer timescales – should be carried out. While this hypothesis is supported by the modeling results herein, the simulations described only span a single regime – i.e., a suppressed similar to one observed in the Indian Ocean during DYNAMO. This hypothesis can undergo more rigorous testing with the aid of a global model, wherein an otherwise identical test to one carried out here is executed – namely, the diurnal cycle can be excluded by prescribing mean insolation, and in another test the diurnal cycle can be stretched to longer periods.

## REFERENCES

- Arakawa, A., and W. H. Schubert, 1974: Interaction of a cumulus cloud ensemble with the large-scale environment, part I. *J. Atmos. Sci.*, **31**, 674–701, doi:10.1175/1520-0469(1974)031<0674:IOACCE>2.0.CO;2.
- Austin, J. M., 1948: A note on cumulus growth in a nonsaturated environment. *J. Meteor.*, **5**, 103–107, doi:10.1175/1520-0469(1948)005<0103:ANOCGI>2.0.CO;2.
- Barnes, H. C., and R. a. Houze, 2013: The precipitating cloud population of the Madden-Julian Oscillation over the Indian and west Pacific Oceans. *J. Geophys. Res.*, **118**, 6996–7023, doi:10.1002/jgrd.50375.
- Bellenger, H., Y. N. Takayabu, T. Ushiyama, and K. Yoneyama, 2010: Role of diurnal warm layers in the diurnal cycle of convection over the tropical Indian Ocean during MISO. *Mon. Wea. Rev.*, **138**, 2426–2433, doi:10.1175/2010MWR3249.1.
- Benedict, J. J., and D. A. Randall, 2007: Observed characteristics of the MJO relative to maximum rainfall. *J. Atmos. Sci.*, **64**, 2332–2354, doi:10.1175/JAS3968.1.
- Bernie, D. J., S. J. Woolnough, J. M. Slingo, and E. Guilyardi, 2005: Modeling diurnal and intraseasonal variability of the ocean mixed layer. *J. Clim.*, **18**, 1190–1202.
- Bernie, D. J., E. Guilyardi, G. Madec, J. M. Slingo, S. J. Woolnough, and J. Cole, 2008: Impact of resolving the diurnal cycle in an ocean–atmosphere GCM. Part 2: A diurnally coupled CGCM. *Clim. Dyn.*, **31**, 909–925, doi:10.1007/s00382-008-0429-z.
- Betts, A. K., 1975: Parametric Interpretation of Trade-Wind Cumulus Budget Studies. *J. Atmos. Sci.*, **32**, 1934–1945, doi:10.1175/1520-0469(1975)032<1934:PIOTWC>2.0.CO;2.
- Bladé, I., and D. L. Hartmann, 1993: Tropical intraseasonal oscillations in a simple nonlinear model. *J. Atmos. Sci.*, **50**, 2922–2939, doi:10.1175/1520-0469(1993)050<2922:TIOIAS>2.0.CO;2.
- Bryan, G., and J. Fritsch, 2002: A benchmark simulation for moist nonhydrostatic numerical models. *Mon. Wea. Rev.*, 2917–2928.
- Bryan, G. H., J. C. Wyngaard, and J. M. Fritsch, 2003: Resolution Requirements for the Simulation of Deep Moist Convection. *Mon. Wea. Rev.*, **131**, 2394–2416, doi:10.1175/1520-0493(2003)131<2394:RRFTSO>2.0.CO;2.
- Charney, J. G., 1963: A note on large-scale motions in the tropics. *J. Atmos. Sci.*, **20**, 607–609, doi:10.1175/1520-0469(1963)020<0607:ANOLSM>2.0.CO;2.

- Chen, S. S., and R. A. Houze, 1997: Diurnal variation and life-cycle of deep convective systems over the tropical pacific warm pool. *Quart. J. Roy. Meteor. Soc.*, **123**, 357–388, doi:10.1002/qj.49712353806.
- Chen, S. S., R. A. Houze, and B. E. Mapes, 1996: Multiscale variability of deep convection in relation to large-scale circulation in TOGA COARE. *J. Atmos. Sci.*, **53**, 1380–1409, doi:10.1175/1520-0469(1996)053<1380:MVODCI>2.0.CO;2.
- Chikira, M., 2014: Eastward-Propagating Intraseasonal Oscillation Represented by Chikira–Sugiyama Cumulus Parameterization. Part II: Understanding Moisture Variation under Weak Temperature Gradient Balance. *J. Atmos. Sci.*, **71**, 615–639, doi:10.1175/JAS-D-13-038.1.
- Chou, M.-D., and M. J. Suarez, 1994: An efficient thermal infrared radiation parameterization for use in general circulation models. *NASA Tech. Memo. 104606*, vol. **3**, 102 pp.
- Chou, M.-D., and M. J. Suarez, 1999: A solar radiation parameterization for atmospheric studies. *NASA Tech. Memo., NASA/TM-1999-104606*, **15**.
- Ciesielski, P. E., R. H. Johnson, P. T. Haertel, and J. Wang, 2003: Corrected TOGA COARE sounding humidity data: Impact on diagnosed properties of convection and climate over the warm pool. *J. Climate*, **16**, 2370–2384.
- Ciesielski, P. E. and Coauthors, 2014a: Quality-controlled upper-air sounding dataset for DYNAMO/CINDY/AMIE: Development and corrections. *J. Atmos. Oceanic Technol.*, **31**, 741–764, doi:10.1175/JTECH-D-13-00165.1.
- Ciesielski, P. E., R. H. Johnson, and R. K. Taft, 2014b: Mitigation of Sri Lanka Island Effects in Colombo Sounding Data and Its Impact on DYNAMO Analyses. doi:10.2151/jmsj.2014-407.
- Computational and Information Systems Laboratory. 2012. Yellowstone: IBM iDataPlex System (University Community Computing). Boulder, CO: National Center for Atmospheric Research. <http://n2t.net/ark:/85065/d7wd3xhc>.
- Dai, A., 2001: Global precipitation and thunderstorm frequencies. Part II: Diurnal variations. *J. Climate*, **14**, 1112–1128, doi:10.1175/1520-0442(2001)014<1112:GPATFP>2.0.CO;2.
- Davison, J. L., R. M. Rauber, and L. Di Girolamo, 2013: A revised conceptual model of the tropical marine boundary layer. Part II: Detecting relative humidity layers using Bragg scattering from S-Band radar. *J. Atmos. Sci.*, **70**, 3025–3046, doi:10.1175/JAS-D-12-0322.1.
- Deardorff, J. W., 1980: Stratocumulus-capped mixed layers derived from a three-dimensional model. *Boundary-Layer Meteorol.*, **18**, 495–527, doi:10.1007/BF00119502.

- DeMott, C. A., and S. A. Rutledge, 1998: The Vertical Structure of TOGA COARE Th vertical structure of TOGA COARE convection. Part II: Modulating influences and implications for diabatic heating. *J. Atmos. Sci.*, **55**, 2748–2762, doi:10.1175/1520-0469(1998)055<2748:TVSOTC>2.0.CO;2.
- Derbyshire, S. H., I. Beau, P. Bechtold, J.-Y. Grandpeix, J.-M. Piriou, J.-L. Redelsperger, and P. M. M. Soares, 2004: Sensitivity of moist convection to environmental humidity. *Quart. J. Roy. Meteor. Soc.*, **130**, 3055–3079, doi:10.1256/qj.03.130.
- Deser, C., and C. A. Smith, 1998: Diurnal and Semidiurnal Variations of the Surface Wind Field over the Tropical Pacific Ocean. *J. Climate*, **11**, 1730–1748, doi:10.1175/1520-0442(1998)011<1730:DASVOT>2.0.CO;2.
- Duvel, J. P., R. Roca, and J. Vialard, 2004: Ocean mixed layer temperature variations induced by intraseasonal convective perturbations over the Indian Ocean. *J. Atmos. Sci.*, **61**, 1004–1023, doi:10.1175/1520-0469(2004)061<1004:OMLTVI>2.0.CO;2.
- Fairall, C. W., E. F. Bradley, J. E. Hare, A. A. Grachev, and J. B. Edson, 2003: Bulk Parameterization of Air–Sea Fluxes: Updates and Verification for the COARE Algorithm. *J. Climate*, **16**, 571–591, doi:10.1175/1520-0442(2003)016<0571:BPOASF>2.0.CO;2.
- Feng, Z., S. A. McFarlane, C. Schumacher, S. Ellis, J. Comstock, and N. Bharadwaj, 2014: Constructing a merged cloud–precipitation radar dataset for tropical convective clouds during the DYNAMO/AMIE experiment at Addu Atoll. *J. Atmos. Oceanic Technol.*, **31**, 1021–1042, doi:10.1175/JTECH-D-13-00132.1.
- Flament, P., J. Firing, M. Sawyer, and C. Trefois, 1994: Amplitude and horizontal structure of a large diurnal sea surface warming event during the Coastal Ocean Dynamics Experiment. *J. Phys. Oceanogr.*, **24**, 124–139.
- Del Genio, A. D., Y. Chen, D. Kim, and M.-S. Yao, 2012: The MJO transition from shallow to deep convection in CloudSat/CALIPSO data and GISS GCM simulations. *J. Climate*, **25**, 3755–3770, doi:10.1175/JCLI-D-11-00384.1.
- Gill, A. E., 1980: Some simple solutions for heat-induced tropical circulation. *Quart. J. Roy. Meteor. Soc.*, **106**, 447–462, doi:10.1002/qj.49710644905.
- Gottschalck, J., P. E. Roundy, C. J. Schreck III, A. Vintzileos, and C. Zhang, 2013: Large-scale atmospheric and oceanic conditions during the 2011–12 DYNAMO field campaign. *Mon. Wea. Rev.*, **141**, 4173–4196, doi:10.1175/MWR-D-13-00022.1.
- Gray, W. M., and R. W. Jacobson, 1977: Diurnal variation of deep cumulus convection. *Mon. Wea. Rev.*, **105**, 1171–1188.

- Haertel, P. T., G. N. Kiladis, A. Denno, and T. M. Rickenbach, 2008: Vertical-mode decompositions of 2-day waves and the Madden–Julian Oscillation. *J. Atmos. Sci.*, **65**, 813–833, doi:10.1175/2007JAS2314.1.
- Halpern, D., and R. K. Reed, 1976: Heat budget of the upper ocean under light winds. *J. Phys. Oceanogr.*, **6**, 972–975, doi:10.1175/1520-0485(1976)006<0972:HBOTUO>2.0.CO;2.
- Hendon, H. H., and B. Liebmann, 1990: The intraseasonal (30–50 day) oscillation of the Australian summer monsoon. *J. Atmos. Sci.*, **47**, 2909–2924, doi:10.1175/1520-0469(1990)047<2909:TIDOOT>2.0.CO;2.
- Hendon, H. H., and M. L. Salby, 1994: The life cycle of the Madden–Julian Oscillation. *J. Atmos. Sci.*, **51**, 2225–2237, doi:10.1175/1520-0469(1994)051<2225:TLCOTM>2.0.CO;2.
- Hendon, H. H., B. Liebmann, M. Newman, J. D. Glick, and J. E. Schemm, 2000: Medium-range forecast errors associated with active episodes of the Madden-Julian Oscillation. *Mon. Wea. Rev.*, **128**, 69–86.
- Herman, M. J., and D. J. Raymond, 2014: WTG cloud modeling with spectral decomposition of heating. *J. Adv. Model. Earth Sys.*, **6**, 1121–1140, doi:10.1002/2014MS000359.
- Hohenegger, C., and B. Stevens, 2013: Preconditioning deep convection with cumulus congestus. *J. Atmos. Sci.*, **70**, 448–464, doi:10.1175/JAS-D-12-089.1.
- Huffman, G. J. and Coauthors, 2007: The TRMM Multisatellite Precipitation Analysis (TMPA): Quasi-Global, Multiyear, Combined-Sensor Precipitation Estimates at Fine Scales. *J. Hydrometeor.*, **8**, 38–55, doi:10.1175/JHM560.1.
- Jiang, X. and Coauthors, 2011: Vertical Diabatic Heating Structure of the MJO: Intercomparison between Recent Reanalyses and TRMM Estimates. *Mon. Wea. Rev.*, **139**, 3208–3223, doi:10.1175/2011MWR3636.1.
- Johnson, R. H., 2011: Diurnal cycle of monsoon convection. 257–276.
- Johnson, R. H., and X. Lin, 1997: Episodic Trade Wind Regimes over the Western Pacific Warm Pool. *J. Atmos. Sci.*, **54**, 2020–2034, doi:10.1175/1520-0469(1997)054<2020:ETWROT>2.0.CO;2.
- Johnson, R. H., and P. E. Ciesielski, 2002: Characteristics of the 1998 summer monsoon onset over the northern South China Sea. *J. Meteor. Soc. Japan*, **80**, 561–578, doi:10.2151/jmsj.80.561.
- Johnson, R. H., and P. E. Ciesielski, 2013: Structure and properties of Madden–Julian Oscillations deduced from DYNAMO sounding arrays. *J. Atmos. Sci.*, **70**, 3157–3179, doi:10.1175/JAS-D-13-065.1.

- Johnson, R. H., T. M. Rickenbach, S. A. Rutledge, P. E. Ciesielski, and W. H. Schubert, 1999: Trimodal characteristics of tropical convection. *J. Climate*, **12**, 2397–2418.
- Johnson, R. H., P. E. Ciesielski, and J. A. Cotturone, 2001: Multiscale Variability of the Atmospheric Mixed Layer over the Western Pacific Warm Pool. *J. Atmos. Sci.*, **58**, 2729–2750, doi:10.1175/1520-0469(2001)058<2729:MVOTAM>2.0.CO;2.
- Johnson, R. H., P. E. Ciesielski, T. S. L’Ecuyer, and A. J. Newman, 2010: Diurnal cycle of convection during the 2004 North American Monsoon Experiment. *J. Climate*, **23**, 1060–1078, doi:10.1175/2009JCLI3275.1.
- Johnson, R. H., P. E. Ciesielski, J. H. Ruppert, and M. Katsumata, 2015: Sounding-Based Thermodynamic Budgets for DYNAMO. *J. Atmos. Sci.*, **72**, 598–622, doi:10.1175/JAS-D-14-0202.1.
- Katsumata, M., P. E. Ciesielski, and R. H. Johnson, 2011: Evaluation of budget analyses during MISMO. *J. Appl. Meteor. Climatol.*, **50**, 241–254, doi:10.1175/2010JAMC2515.1.
- Kawai, Y., and A. Wada, 2007: Diurnal sea surface temperature variation and Its Impact on the atmosphere and ocean: A review. *J. Oceanogr.*, **63**, 721–744.
- Keeler, R. J., J. Lutz, and J. Vivekanandan, 2000: S-Pol: NCAR’s polarimetric Doppler research radar. *IGARSS 2000. IEEE 2000 Int. Geosci. Remote Sens. Symp. Tak. Pulse Planet Role Remote Sens. Manag. Environ. Proc. (Cat. No.00CH37120)*, **4**, 1570–1573, doi:10.1109/IGARSS.2000.857275.
- Kemball-Cook, S. R., and B. C. Weare, 2001: The Onset of Convection in the Madden–Julian Oscillation. *J. Climate*, **14**, 780–793, doi:10.1175/1520-0442(2001)014<0780:TOOCIT>2.0.CO;2.
- Kerns, B. W., and S. S. Chen, 2014: Equatorial Dry Air Intrusion and Related Synoptic Variability in MJO Initiation during DYNAMO. *Mon. Wea. Rev.*, **142**, 1326–1343, doi:10.1175/MWR-D-13-00159.1.
- Kikuchi, K., and Y. N. Takayabu, 2004: The development of organized convection associated with the MJO during TOGA COARE IOP: Trimodal characteristics. *Geophys. Res. Lett.*, **31**, L10101, doi:10.1029/2004GL019601.
- Kiladis, G. N., K. H. Straub, G. C. Reid, and K. S. Gage, 2001: Aspects of interannual and intraseasonal variability of the tropopause and lower stratosphere. *Quart. J. Roy. Meteor. Soc.*, **127**, 1961–1983, doi:10.1002/qj.49712757606.
- Kiladis, G. N., K. H. Straub, and P. T. Haertel, 2005: Zonal and vertical structure of the Madden-Julian oscillation. *J. Atmos. Sci.*, **62**, 2790–2809.

- Klemp, J. B., and R. B. Wilhelmson, 1978: The Simulation of Three-Dimensional Convective Storm Dynamics. *J. Atmos. Sci.*, **35**, 1070–1096, doi:10.1175/1520-0469(1978)035<1070:TSOTDC>2.0.CO;2.
- Klemp, J. B., W. C. Skamarock, and J. Dudhia, 2007: Conservative Split-Explicit Time Integration Methods for the Compressible Nonhydrostatic Equations. *Mon. Wea. Rev.*, **135**, 2897–2913, doi:10.1175/MWR3440.1.
- Kummerow, C. and Coauthors, 2000: The Status of the Tropical Rainfall Measuring Mission (TRMM) after Two Years in Orbit. *J. Appl. Meteorol.*, **39**, 1965–1982, doi:10.1175/1520-0450(2001)040<1965:TSOTTR>2.0.CO;2.
- LeMone, M. a., and W. T. Pennell, 1976: The Relationship of Trade Wind Cumulus Distribution to Subcloud Layer Fluxes and Structure. *Mon. Wea. Rev.*, **104**, 524–539, doi:10.1175/1520-0493(1976)104<0524:TROTWC>2.0.CO;2.
- Lin, J.-L. and Coauthors, 2006: Tropical Intraseasonal Variability in 14 IPCC AR4 Climate Models. Part I: Convective Signals. *J. Climate*, **19**, 2665–2690, doi:10.1175/JCLI3735.1.
- Lin, X., and R. H. Johnson, 1996a: Kinematic and thermodynamic characteristics of the flow over the western Pacific warm pool during TOGA COARE. *J. Atmos. Sci.*, **53**, 695–715, doi:10.1175/1520-0469(1996)053<0695:KATCOT>2.0.CO;2.
- Lin, X., and R. H. Johnson, 1996b: Heating, moistening, and rainfall over the western Pacific warm pool during TOGA COARE. *J. Atmos. Sci.*, **53**, 3367–3383, doi:10.1175/1520-0469(1996)053<3367:HMAROT>2.0.CO;2.
- Lin, Y.-L., R. D. Farley, and H. D. Orville, 1983: Bulk Parameterization of the Snow Field in a Cloud Model. *J. Clim. Appl. Meteorol.*, **22**, 1065–1092, doi:10.1175/1520-0450(1983)022<1065:BPOTSF>2.0.CO;2.
- Liu, C., E. J. Zipser, and S. W. Nesbitt, 2007: Global distribution of tropical deep convection: Different perspectives from TRMM infrared and radar data. *J. Climate*, **20**, 489–503.
- Madden, R., and P. Julian, 1972: Description of global-scale circulation cells in the tropics with a 40-50 day period. *J. Atmos. Sci.*, **29**, 1109–1123.
- Madden, R. A., and P. R. Julian, 1971: Detection of a 40-50 day oscillation in the zonal wind in the tropical Pacific. *J. Atmos. Sci.*, **28**, 702–708.
- Majda, A. J., and S. N. Stechmann, 2009: The skeleton of tropical intraseasonal oscillations. *Proc. Natl. Acad. Sci. USA*, **106**, 8417–8422, doi:10.1073/pnas.0903367106.
- Maloney, E. D., and D. L. Hartmann, 1998: Frictional moisture convergence in a composite life cycle of the Madden-Julian oscillation. *J. Climate*, **11**, 2387–2403.

- Mapes, B., S. Tulich, J. Lin, and P. Zuidema, 2006: The mesoscale convection life cycle: Building block or prototype for large-scale tropical waves? *Dyn. Atmos. Ocean.*, **42**, 3–29, doi:10.1016/j.dynatmoce.2006.03.003.
- Mapes, B. E., 1993: Gregarious Tropical Convection. *J. Atmos. Sci.*, **50**, 2026–2037, doi:10.1175/1520-0469(1993)050<2026:GTC>2.0.CO;2.
- Mapes, B. E., 2001: Water's two height scales: The moist adiabat and the radiative troposphere. *Quart. J. Roy. Meteor. Soc.*, **127**, 2353–2366, doi:10.1002/qj.49712757708.
- Matthews, A. J., 2008: Primary and successive events in the Madden – Julian Oscillation. *Quart. J. Roy. Meteor. Soc.*, **134**, 439–453, doi:10.1002/qj.
- Matthews, A. J., D. B. Baranowski, K. J. Heywood, P. J. Flatau, and S. Schmidtko, 2014: The Surface Diurnal Warm Layer in the Indian Ocean during CINDY/DYNAMO. *J. Climate*, **27**, 9101–9122, doi:10.1175/JCLI-D-14-00222.1.
- McNab, A. L., and A. K. Betts, 1978: A mesoscale budget study of cumulus convection. *Mon. Wea. Rev.*, **106**, 1317–1331, doi:10.1175/1520-0493(1978)106<1317:AMBSOC>2.0.CO;2.
- McNoldy, B. D., P. E. Ciesielski, W. H. Schubert, and R. H. Johnson, 2004: Surface winds, divergence, and vorticity in stratocumulus regions using QuikSCAT and reanalysis winds. *Geophys. Res. Lett.*, **31**, 1–5, doi:10.1029/2004GL019768.
- Moncrieff, M. W., D. E. Waliser, M. J. Miller, M. a. Shapiro, G. R. Asrar, and J. Caughey, 2012: Multiscale convective organization and the YOTC virtual global field campaign. *Bull. Amer. Meteor. Soc.*, **93**, 1171–1187, doi:10.1175/BAMS-D-11-00233.1.
- Morrison, H., J. A. Curry, and V. I. Khvorostyanov, 2005: A New Double-Moment Microphysics Parameterization for Application in Cloud and Climate Models. Part I: Description. *J. Atmos. Sci.*, **62**, 1665–1677, doi:10.1175/JAS3446.1.
- Morrison, H., G. Thompson, and V. Tatarskii, 2009: Impact of Cloud Microphysics on the Development of Trailing Stratiform Precipitation in a Simulated Squall Line: Comparison of One- and Two-Moment Schemes. *Mon. Wea. Rev.*, **137**, 991–1007, doi:10.1175/2008MWR2556.1.
- Moum, J. N. and Coauthors, 2013: Air-sea interactions from westerly wind bursts during the November 2011 MJO in the Indian Ocean. *Bull. Am. Meteorol. Soc.* **2013** ; e-View, 1–49, doi:http://dx.doi.org/10.1175/BAMS-D-12-00225.1.
- Nicholls, M. E., R. A. Pielke, and W. R. Cotton, 1991: Thermally Forced Gravity Waves in an Atmosphere at Rest. *J. Atmos. Sci.*, **48**, 1869–1884, doi:10.1175/1520-0469(1991)048<1869:TFGWIA>2.0.CO;2.

- Nitta, T., and S. Esbensen, 1974: Heat and moisture budget analyses using BOMEX data. *Mon. Wea. Rev.*, **102**, 17–28, doi:10.1175/1520-0493(1974)102<0017:HAMBAU>2.0.CO;2.
- Nuss, W. A., and D. W. Titley, 1994: Use of multiquadric interpolation for meteorological objective analysis. *Mon. Wea. Rev.*, **122**, 1611–1631.
- O'Brien, J. J., 1970: Alternative Solutions to the Classical Vertical Velocity Problem. *J. Appl. Meteorol.*, **9**, 197–203, doi:10.1175/1520-0450(1970)009<0197:ASTTCV>2.0.CO;2.
- Powell, S. W., and R. A. Houze, 2013: The cloud population and onset of the Madden-Julian Oscillation over the Indian Ocean during DYNAMO-AMIE. *J. Geophys. Res.*, **118**, 11,979–11,995, doi:10.1002/2013JD020421.
- Praveen Kumar, B., J. Vialard, M. Lengaigne, V. S. N. Murty, and M. J. McPhaden, 2011: TropFlux: air-sea fluxes for the global tropical oceans—description and evaluation. *Clim. Dyn.*, **38**, 1521–1543, doi:10.1007/s00382-011-1115-0.
- Randall, D. A., Harshvardhan, and D. A. Dazlich, 1991: Diurnal Variability of the Hydrologic Cycle in a General Circulation Model. *J. Atmos. Sci.*, **48**, 40–62, doi:10.1175/1520-0469(1991)048<0040:DVOTHC>2.0.CO;2.
- Raymond, D. J., 2001: A new model of the Madden–Julian oscillation. *J. Atmos. Sci.*, **58**, 2807–2819, doi:10.1175/1520-0469(2001)058<2807:ANMOTM>2.0.CO;2.
- Raymond, D. J., and X. Zeng, 2005: Modelling tropical atmospheric convection in the context of the weak temperature gradient approximation. *Quart. J. Roy. Meteor. Soc.*, **131**, 1301–1320, doi:10.1256/qj.03.97.
- Redelsperger, J. L., D. B. Parsons, and F. Guichard, 2002: Recovery processes and factors limiting cloud-top height following the arrival of a dry intrusion observed during TOGA COARE. *J. Atmos. Sci.*, **59**, 2438–2457.
- Riley, E. M., B. E. Mapes, and S. N. Tulich, 2011: Clouds associated with the Madden–Julian oscillation: A new perspective from CloudSat. *J. Atmos. Sci.*, **68**, 3032–3051, doi:10.1175/JAS-D-11-030.1.
- Rowe, A. K., and R. a. Houze, 2014: Microphysical characteristics of MJO convection over the Indian Ocean during DYNAMO. *J. Geophys. Res.*, **119**, 2543–2554, doi:10.1002/2013JD020799.
- Rui, H., and B. Wang, 1990: Development characteristics and dynamic structure of tropical intraseasonal convection anomalies. *J. Atmos. Sci.*, **47**, 357–379, doi:10.1175/1520-0469(1990)047<0357:DCADSO>2.0.CO;2.

- Ruppert, J. H., and R. H. Johnson, 2015: Diurnally Modulated Cumulus Moistening in the Pre-Onset Stage of the Madden–Julian Oscillation during DYNAMO. *J. Atmos. Sci.*, **72**, 141224143226006, doi:10.1175/JAS-D-14-0218.1.
- Ruppert, J. H., R. H. Johnson, and A. K. Rowe, 2013: Diurnal circulations and rainfall in Taiwan during SoWMEX/TiMREX (2008). *Mon. Wea. Rev.*, **141**, 3851–3872, doi:10.1175/MWR-D-12-00301.1.
- Sobel, a. H., and C. S. Bretherton, 2000: Modeling tropical precipitation in a single column. *J. Climate*, **13**, 4378–4392, doi:10.1175/1520-0442(2000)013<4378:MTPIAS>2.0.CO;2.
- Sobel, A., S. Wang, and D. Kim, 2014: Moist Static Energy Budget of the MJO during DYNAMO. *J. Atmos. Sci.*, **71**, 4276–4291, doi:10.1175/JAS-D-14-0052.1.
- Sobel, A. H., J. Nilsson, and L. M. Polvani, 2001: The Weak Temperature Gradient Approximation and Balanced Tropical Moisture Waves\*. *J. Atmos. Sci.*, **58**, 3650–3665, doi:10.1175/1520-0469(2001)058<3650:TWTGAA>2.0.CO;2.
- Stephens, G. L., P. J. Webster, R. H. Johnson, R. Engelen, and T. L’Ecuyer, 2004: Observational evidence for the mutual regulation of the tropical hydrological cycle and tropical sea surface temperatures. *J. Climate*, **17**, 2213–2224.
- Stramma, L., P. Cornillon, R. A. Weller, J. F. Price, and M. G. Briscoe, 1986: Large diurnal sea surface temperature variability: Satellite and in situ measurements. *J. Phys. Oceanogr.*, **16**, 827–837, doi:10.1175/1520-0485(1986)016<0827:LDSSTV>2.0.CO;2.
- Sui, C.-H., K.-M. Lau, Y. N. Takayabu, and D. A. Short, 1997: Diurnal variations in tropical oceanic cumulus convection during TOGA COARE. *J. Atmos. Sci.*, **54**, 639–655.
- Sui, C.-H., X. Li, and K.-M. Lau, 1998: Radiative-convective processes in simulated diurnal variations of tropical oceanic convection. *J. Atmos. Sci.*, **55**, 2345–2357.
- Takemi, T., O. Hirayama, and C. Liu, 2004: Factors responsible for the vertical development of tropical oceanic cumulus convection. *Geophys. Res. Lett.*, **31**, 4, doi:10.1029/2004GL020225.
- Tao, W.-K., S. Lang, J. Simpson, C.-H. Sui, B. Ferrier, and M.-D. Chou, 1996: Mechanisms of Cloud-Radiation Interaction in the Tropics and Midlatitudes. *J. Atmos. Sci.*, **53**, 2624–2651, doi:10.1175/1520-0469(1996)053<2624:MOCRII>2.0.CO;2.
- Vialard, J. and Coauthors, 2009: CIRENE: Air—sea interactions in the Seychelles—Chagos thermocline ridge region. *Bull. Amer. Meteor. Soc.*, **90**, 45–61, doi:10.1175/2008BAMS2499.2.

- Virts, K. S., and J. M. Wallace, 2010: Annual, interannual, and intraseasonal variability of tropical tropopause transition layer cirrus. *J. Atmos. Sci.*, **67**, 3097–3112, doi:10.1175/2010JAS3413.1.
- Virts, K. S., J. M. Wallace, Q. Fu, and T. P. Ackerman, 2010: Tropical tropopause transition layer cirrus as represented by CALIPSO lidar observations. *J. Atmos. Sci.*, **67**, 3113–3129, doi:10.1175/2010JAS3412.1.
- Waite, M. L., and B. Khouider, 2010: The deepening of tropical convection by congestus preconditioning. *J. Atmos. Sci.*, **67**, 2601–2615, doi:10.1175/2010JAS3357.1.
- Waliser, D. E., K. M. Lau, W. Stern, and C. Jones, 2003: Potential predictability of the Madden-Julian oscillation. *Bull. Amer. Meteor. Soc.*, **84**, 33–50, doi:10.1175/BAMS-84-1-33.
- Waliser, D. E. and Coauthors, 2012: The “Year” of Tropical Convection (May 2008–April 2010): Climate variability and weather highlights. *Bull. Amer. Meteor. Soc.*, **93**, 1189–1218, doi:10.1175/2011BAMS3095.1.
- Webster, P. J., C. A. Clayson, and J. A. Curry, 1996: Clouds, Radiation, and the Diurnal Cycle of Sea Surface Temperature in the Tropical Western Pacific. *J. Climate*, **9**, 1712–1730, doi:10.1175/1520-0442(1996)009<1712:CRATDC>2.0.CO;2.
- Weckwerth, T. M., J. W. Wilson, and R. M. Wakimoto, 1996: Thermodynamic variability within the convective boundary layer due to horizontal convective rolls. *Mon. Wea. Rev.*, **124**, 769–784, doi:10.1175/1520-0493(1996)124<0769:TVWTCTB>2.0.CO;2.
- Weckwerth, T. M., T. W. Horst, and J. W. Wilson, 1999: An Observational Study of the Evolution of Horizontal Convective Rolls. *Mon. Wea. Rev.*, **127**, 2160–2179, doi:10.1175/1520-0493(1999)127<2160:AOSOTE>2.0.CO;2.
- Wei, D., A. M. Blyth, and D. J. Raymond, 1998: Buoyancy of convective clouds in TOGA COARE. *J. Atmos. Sci.*, **55**, 3381–3391, doi:10.1175/1520-0469(1998)055<3381:BOCCIT>2.0.CO;2.
- Weller, R. A., and S. P. Anderson, 1996: Surface meteorology and air-sea fluxes in the western equatorial Pacific warm pool during the TOGA Coupled Ocean-Atmosphere Response Experiment. *J. Climate*, **9**, 1959–1990, doi:10.1175/1520-0442(1996)009<1959:SMAASF>2.0.CO;2.
- Wheeler, M. C., and H. H. Hendon, 2004: An all-season real-time multivariate MJO index: Development of an index for monitoring and prediction. *Mon. Wea. Rev.*, **132**, 1917–1932, doi:10.1175/1520-0493(2004)132<1917:AARMMI>2.0.CO;2.
- Wicker, L. J., and W. C. Skamarock, 2002: Time-Splitting Methods for Elastic Models Using Forward Time Schemes. *Mon. Wea. Rev.*, **130**, 2088–2097, doi:10.1175/1520-0493(2002)130<2088:TSMFEM>2.0.CO;2.

- Wu, Z., 2003: A shallow CISK, deep equilibrium mechanism for the interaction between large-scale convection and large-scale circulations in the tropics. *J. Atmos. Sci.*,
- Xu, K.-M., and D. A. Randall, 1995: Impact of Interactive Radiative Transfer on the Macroscopic Behavior of Cumulus Ensembles. Part II: Mechanisms for Cloud-Radiation Interactions. *J. Atmos. Sci.*, **52**, 800–817, doi:10.1175/1520-0469(1995)052<0800:IOIRTO>2.0.CO;2.
- Xu, W., and S. A. Rutledge, 2014: Convective characteristics of the Madden–Julian Oscillation over the central Indian Ocean observed by shipborne radar during DYNAMO. *J. Atmos. Sci.*, **71**, 2859–2877, doi:10.1175/JAS-D-13-0372.1.
- Yanai, M., and R. H. Johnson, 1993: Impacts of cumulus convection on thermodynamic fields. *Meteor. Monogr.*, **24**, 39–62.
- Yanai, M., S. Esbensen, and J.-H. Chu, 1973: Determination of bulk properties of tropical cloud clusters from large-scale heat and moisture budgets. *J. Atmos. Sci.*, **30**, 611–627, doi:10.1175/1520-0469(1973)030<0611:DOBPOT>2.0.CO;2.
- Yang, G.-Y., and J. Slingo, 2001: The Diurnal Cycle in the Tropics. *Mon. Wea. Rev.*, **129**, 784–801, doi:10.1175/1520-0493(2001)129<0784:TDCITT>2.0.CO;2.
- Yang, S., and E. A. Smith, 2006: Mechanisms for Diurnal Variability of Global Tropical Rainfall Observed from TRMM. *J. Climate*, **19**, 5190–5226, doi:10.1175/JCLI3883.1.
- Yasunaga, K., M. Fujita, T. Ushiyama, K. Yoneyama, Y. N. Takayabu, and M. Yoshizaki, 2008: Diurnal variations in precipitable water observed by shipborne GPS over the tropical Indian Ocean. *SOLA*, **4**, 97–100.
- Yoneyama, K. and Coauthors, 2008: Mismo field experiment in the equatorial Indian Ocean. *Bull. Amer. Meteor. Soc.*, **89**, 1889–1903, doi:10.1175/2008BAMS2519.1.
- Yoneyama, K., C. Zhang, and C. N. Long, 2013: Tracking pulses of the Madden–Julian oscillation. *Bull. Amer. Meteor. Soc.*, **94**, 1871–1891, doi:10.1175/BAMS-D-12-00157.1.
- Zhang, C., 2005: Madden-Julian Oscillation. *Rev. Geophys.*, **43**, RG2003, doi:10.1029/2004RG000158.
- Zhang, C., 2013: Madden-Julian Oscillation: Bridging Weather and Climate. *Bull. Amer. Meteor. Soc.*, **94**, 1849–1870, doi:10.1175/BAMS-D-12-00026.1.
- Zhang, C., M. McGauley, and N. Bond, 2004: Shallow Meridional Circulation in the Tropical Eastern Pacific\*. *J. Climate*, 133–139.

- Zhang, C., J. Gottschalck, E. D. Maloney, M. W. Moncrieff, F. Vitart, D. E. Waliser, B. Wang, and M. C. Wheeler, 2013: Cracking the MJO nut. *Geophys. Res. Lett.*, **40**, 1223–1230, doi:10.1002/grl.50244.
- Zipser, E. J., 1977: Mesoscale and convective-scale downdrafts as distinct components of squall-line structure. *Mon. Wea. Rev.*, **105**, 1568–1589.
- Zuluaga, M. D., and R. A. Houze, 2013: Evolution of the population of precipitating convective systems over the equatorial Indian Ocean in active phases of the Madden–Julian oscillation. *J. Atmos. Sci.*, **70**, 2713–2725, doi:10.1175/JAS-D-12-0311.1.